The European Master in Advanced Structural Analysis and Design using Composite Materials is a join initiative of:

Universidade do Minho

Universitat de Girona

Università degli Studi di Napoli Federico II

INSA Institut National des Sciences Appliquées Toulouse

Université de Toulouse

Assessment of the effectiveness of different techniques for the strengthening of corroded reinforced concrete piles

John Francis Emolu

FRP++ Advanced structural analysis and design using composite materials

UMinho | 2026

Universidade do Minho
Escola de Engenharia

John Francis Emolu

Assessment of the effectiveness of different techniques for the strengthening of corroded reinforced concrete piles

FRP++
Advanced structural analysis and design using composite materials

Funded by the European Union

September 2026

Universidade do Minho
Escola de Engenharia

John Francis Emolu

Assessment of the effectiveness of different techniques for the strengthening of corroded reinforced concrete piles

FRP++
Advanced structural analysis and design using composite materials

Master Dissertation
European Master Advanced Structural Analysis and Design using Composite Materials

Work developed under the supervision of
Professor Joaquim António Oliveira Barros
Professor Rudolf Seracino

Funded by
the European Union

September 2026

DIREITOS DE AUTOR E CONDIÇÕES DE UTILIZAÇÃO DO TRABALHO POR TERCEIROS

Este é um trabalho académico que pode ser utilizado por terceiros desde que respeitadas as regras e boas práticas internacionalmente aceites, no que concerne aos direitos de autor e direitos conexos.

Assim, o presente trabalho pode ser utilizado nos termos previstos na licença abaixo indicada.

Caso o utilizador necessite de permissão para poder fazer um uso do trabalho em condições não previstas no licenciamento indicado, deverá contactar o autor, através do RepositóriUM da Universidade do Minho.

Licença concedida aos utilizadores deste trabalho



Atribuição CC BY

https://creativecommons.org/licenses/by/4.0/

ACKNOWLEDGEMENTS

This dissertation was carried out at the Department of Civil Engineering of the University of Minho (Portugal), in collaboration with North Carolina State University (US), under the supervision of Professor Joaquim Oliveira Barros and Professor Rudolf Seracino.

First, I would like to express my sincere gratitude to Professor Joaquim Barros for his profound mentorship, encouragement and patience throughout the development of this thesis work. He guided me through the development of most of the technical aspects of implemented in this work, particularly the analytical frameworks for flexural analysis with DOCROS and shear, drawing on his deep technical expertise in structural concepts and composite materials to steer the direction of this work with rigour, clarity, and confidence at every stage. Professor Barros always challenged me to think like an engineer in navigating complex problems along the way, and his timely feedback to my questions were very insightful.

I am very grateful for the opportunity of collaborating with Professor Rudolf Seracino in this project. I thank him for availing all the necessary resources and details including the as-built drawings, project goals and objectives, which provided the foundation and the real case study around which this dissertation was developed. Despite the long distance and time difference, he always made it possible to discuss and review the research outcomes, and provided timely feedback to all my questions and doubts.

I thank the leadership of the FRP Secretariat for giving me the opportunity to participate in this program. In a special way, I would like to thank Dr. Luís Correia for following up on my onboarding process to the program, even when I was behind the official registration schedule and all hope seemed lost. I thank Professor José Sena Cruz and Carla Gomes for their immense contribution to the success of this program.

Most importantly, I would like to gratefully acknowledge the financial support provided by the European Union for participation in the Erasmus Mundus FRP++ European Master Course in Advanced Structural Analysis and Design using Composite Materials (Project no. 101048961). This work was also supported by FCT/MCTES under the R&D Unit Institute for Sustainability and Innovation in Structural Engineering (ISISE), under the references UID/4029/2025 (DOI: 10.54499/UID/04029/2025), UID/PRR/04029/2025 (DOI:

10.54499/UID/PRR/04029/2025) and UID/PRR2/04029/2025 (DOI: 10.54499/UID/PRR2/04029/2025), and under the Associate Laboratory Advanced Production and Intelligent Systems ARISE under reference LA/P/0112/2020 (DOI: 10.54499/LA/P/0112/2020).

Finally, I am deeply grateful to my friends, especially to Basel Fouda for providing valuable insights, constructive discussions, and moral support. I also extend my appreciation to my family for their encouragement, and unwavering belief in me. Thank you for always praying for me. Thank you everyone, I love you all.

STATEMENT OF INTEGRITY

I hereby declare having conducted this academic work with integrity. I confirm that I have not used plagiarism or any form of undue use of information or falsification of results along the process leading to its elaboration.

I further declare that I have fully acknowledged the Code of Ethics and Conduct of the University of Minho.

DECLARATION ON THE USE OF ARTIFICIAL INTELLIGENCE (AI) TOOLS

I hereby declare having acted this academic work with integrity and confirm that I have not resorted to any form of undue use of AI tools, nor to the falsification or omission of information, sources, data, results or processes in any of the stages leading to its elaboration.

I further declare that any use of AI tools was done in a transparent and responsible manner, being duly noted in the work, and that I critically verified the accuracy of the content produced with their support, assuming full responsibility for what I submit.

I further declare that I have fully acknowledged the Code of Ethics and Conduct of the University of Minho, as well as the applicable standards of academic integrity and data protection.

Avaliação da eficiência de diferentes técnicas no reforço de estacas de betão armado com corrosão

RESUMO

Esta dissertação desenvolve e aplica modelos analíticos para prever a capacidade resistente à flexão e ao esforço transverso de estacas de betão armado (BA) deterioradas e reforçadas através de diferentes técnicas com polímeros reforçados com fibras (FRP). A avaliação à flexão é realizada através de uma análise seccional por camadas, na qual os estados original, deteriorado e reforçado são sistematicamente modelados, considerando-se dois níveis de corrosão predefinidos, correspondentes a reduções de 25% e 50% da área da secção transversal das armaduras de aço existentes nos estados deteriorado e reforçado, respetivamente.

São adotadas configurações de reforço que incluem a reconstrução do recobrimento com betão simples (PC), betão reforçado com fibras de aço (SFRC), compósitos cimentícios com endurecimento por deformação em tração (SHCC), armaduras longitudinais constituídas por varões de polímero reforçado com fibras de vidro (GFRP) e confinamento externo através de encamisamento com polímero reforçado com fibras de carbono (CFRP).

A inexistência de uma solução analítica para prever a capacidade resistente ao esforço transverso de secções circulares reforçadas motivou o desenvolvimento de um modelo analítico de avaliação da resistência ao corte deste tipo de secções e incluindo mais do que um tipo de armaduras/materiais de reforço. Este modelo sobrepõe as contribuições do núcleo de betão armado existente e deteriorado e da nova camada de reforço, avaliadas com base no modelo de treliça, tratando explicitamente a interação com o esforço axial através da posição do eixo neutro e do campo de tensões de compressão.

Os resultados mostram que a corrosão reduz a capacidade resistente ao momento fletor em flexão pura em 31% e 49%, para níveis de corrosão de 25% e 50%, respetivamente. Demonstram igualmente que a simples reconstrução do recobrimento permite recuperar uma parte significativa da capacidade perdida, enquanto o confinamento com FRP proporciona a

maior recuperação de capacidade na região do diagrama de interação controlada pela compressão.

O modelo de corte proposto mostra que a resistência ao esforço transverso do domínio de reforço é determinada quase exclusivamente pelo tipo de nova armadura de reparação e é, em grande medida, insensível ao estado de corrosão do núcleo existente. Por sua vez, a resistência do núcleo existente diminui sistematicamente com a perda de secção das armaduras longitudinais e transversais, sendo substancialmente aumentada pela compressão axial.

Palavras-chave: Corrosão; estacas de betão armado; confinamento com FRP; núcleo de betão existente; domínio de reforço.

Assessment of the effectiveness of different techniques for the strengthening of corroded reinforced concrete piles

ABSTRACT

This dissertation develops and applies analytical frameworks for predicting the flexural and shear capacity of deteriorated reinforced concrete (RC) piles strengthened with different fibre-reinforced polymer (FRP) strengthening techniques. Flexural assessment is performed through layered sectional analysis, in which the as-built, deteriorated and strengthened states are systematically modelled with two prescribed corrosion levels corresponding to 25% and 50% reductions in the cross-sectional area of the existing steel reinforcement in the deteriorated and strengthened states respectively. Strengthening configurations comprising cover reconstruction with plain concrete (PC), steel-fibre-reinforced concrete (SFRC), strain hardening cementitious composites (SHCC), glass-fibre-reinforced polymer (GFRP) longitudinal bar reinforcement, and external confinement using carbon-FRP jackets are adopted. The absence of a closed-form solution for predicting the shear capacity of circular strengthened cross-sections inspired the development of an analytical shear model, superposing the contribution of the existing deteriorated RC core and the new strengthening cover, evaluated based on the truss model, with explicit treatment of the axial load interaction through the neutral-axis position and the compressive stress field. The results show that corrosion reduces pure-bending moment capacity by 31% and 49% at 25% and 50 % corrosion respectively, and that cover restoration alone recovers a significant amount of the lost capacity, while FRP confinement provides the largest capacity recovery in the compression-controlled region of the interaction diagram. The proposed shear model shows that the shear resistance of the strengthening-domain is governed almost entirely by the type of the new repair reinforcement and is largely insensitive to the corroded state of the existing core, while the existing-core resistance degrades systematically with both longitudinal and transverse steel section loss and is amplified substantially by axial compression.

KEYWORDS: Corrosion; Reinforced concrete piles; FRP-confinement; existing concrete core; Strengthening domain

TABLE OF CONTENTS

Acknowledgements iii
Resumo vi
Abstract viii
Table of Contents ix
List of Figures xiii
List of Tables xv
List of Abbreviations and Symbols xvi
1. Introduction 1
1.1. Background and Motivation 1
1.2. The Earl C. Davis Memorial Bridge and Harkers Island Bridge 2
1.3. Thesis Objectives 4
1.4. Structure of Dissertation 5
2. State-of-the-Art Materials and Techniques for the Repair of Corroded RC Structures 9
2.1. Fundamentals of Steel Corrosion in Concrete 9
2.1.1. Chloride-Induced Corrosion 9
2.1.2. Carbon-Induced Corrosion 11
2.2. Inspection and Diagnosis of Corrosion in RC Piles 11
2.2.1. Visual Inspection and Preliminary Assessment 12
2.2.2. Non-Destructive Testing (NDT) Methods 12
2.3. Techniques to Quantify Corrosion in RC Structures 14
2.3.1. Chloride Profiling 15
2.3.2. Gravimetric Mass Loss Measurement 15
2.3.3. Assessment of Corrosion-Induced Cracking and Cover Spalling 16
2.3.4. Photogrammetry, 3D Scanning, and Section Reconstruction 17
2.3.5. Structural Health Monitoring and Embedded Sensor Systems 17
2.4. Material and Techniques for Retrofitting Corrosion Damaged RC Piles 18
2.4.1. Conventional Repair Approaches 18

2.4.2. Fibre-Reinforced Polymer (FRP) Systems 19
2.4.3. FRP Repair Systems for Piles in Wet and Underwater Conditions 22
3. Analytical Framework for Flexural and Axial Capacity Assessment of the Deteriorated and Strengthened RC Piles 27
3.1. Introduction 27
3.2. Layered Sectional Analysis 28
3.2.1. Fundamental Assumptions and Section Discretization 28
3.2.2. Section Discretization 28
3.2.3. Equilibrium Conditions 29
3.3. Constitutive Models for Structural Materials 30
3.3.1. Plain Concrete 30
3.3.2. Steel Fibre Reinforced Concrete (SFRC) 33
3.3.3. Strain-Hardening Cementitious Composites (SHCC) 35
3.3.4. Steel Reinforcement 36
3.3.5. Fibre Reinforced Polymers (FRP) 39
3.4. Constitutive Model for FRP Confined Reinforced Concrete 39
3.4.1. Design-Oriented Model (DOM) for FRP Confined Reinforced Concrete 40
4. Analytical Framework For Determining the Shear Capacity of Strengthened RC Piles with Circular Cross-sections 49
4.1. Introduction 49
4.2. Fundamental Governing Equations 49
4.2.1. Formulations from the Truss Model 50
4.2.2. Influence of Axial Loading 51
4.3. Shear Prediction in Circular Sections 54
4.3.1. Determination of the Neutral Axis and Effective Depth 54
4.3.2. Equivalent Rectangular Cross-section and Transverse Reinforcement Efficiency 57
4.4. Proposed Analytical Model for Determining Shear in strengthened circular cross-sections 58

4.4.1. Geometry of Strengthened Circular Cross-section 58
4.4.2. Equations for Predicting the Shear Capacity of the Strengthened Circular Cross-sections 60
4.5. Axial load influence on shear resistance terms 63
4.6. Design Application of the Model 65
4.7. Results for the Shear Strengthening Prediction 66
4.8. Summary 68
5. Results and Discussion of the predicted Flexural, Axial and Shear Capacity of the Deteriorated and Strengthened Piles 69
5.1. Introduction 69
5.2. Flexural and Axial Capacity Assessment 69
5.2.1. Geometry of the Pile Assessment Configurations 69
5.2.2. As-Built vs. Deteriorated Pile Capacity Assessment 71
5.2.3. Strengthening with Plain-Concrete (PC35 and PC60) for cover repair 73
5.2.4. Strengthening with SFRC for cover repair 75
5.2.5. Effect of GFRP Longitudinal Bar Reinforcement in the C60 Concrete Cover 77
5.2.6. Effect of FRP Confinement on the Strengthened Deteriorated Pile 79
5.2.7. Strengthening with SHCC 81
5.3. Shear Capacity Assessment 83
5.3.1. Influence of Corrosion damage 84
5.3.2. Influence of Axial load on the predicted shear capacity 85
5.3.3. Influence of Cover Material and Transverse Reinforcement Type 86
5.3.4. Implications for shear strengthening strategy 88
5.4. Summary 88
6. Conclusions and Further Developments 93
6.1. Main Conclusions 93
6.1.1. Analytical Framework Developed 93
6.1.2. Flexural and Axial Capacity Predictions 94
6.1.3. Shear capacity Predictions 95
6.1.4. Repair Selection Strategy 96

6.2. Further Developments 97
6.2.1. Experimental Validation 97
6.2.2. Finite Element Validation 98
6.2.3. Further Analytical Refinement 99
6.2.4. Cost Assessment and Life Cycle Analysis 100
References 101
Annex I - Derivation of the Compression Segment Area and Centroid for a Circular Section 105
I.1 Area of Compression zone segment 105
I.2 Distance of the Centroid of the Segment from the Neutral Axis 106
Annex II - Derivation of the Axial Force Distribution Between the Existing and Strengthening Domains 108

LIST OF FIGURES

Figure 1.1: The Earl C. Davis Memorial Bridge with new access bridge at time of construction 3
Figure 2.1: Schematic representation of chloride-induced corrosion 10
Figure 2.2: Exposure zones in marine structures 10
Figure 2.3: Carbon-induced corrosion 11
Figure 2.4: Spatial cracking patterns of corrosion damaged concrete at different corrosion level 16
Figure 2.5: Tensile Properties of FRP material types compared to steel 20
Figure 2.6: Stress-strain relationship for confined and unconfined concrete 21
Figure 2.7: FRP strengthening techniques in marine environments 22
Figure 2.8: Strengthening of marine piles with prefabricated GFRP and CFRP jackets 24
Figure 3.1: Section discretization in DOCROS 29
Figure 3.2: a) Schematic representation of concrete in compression b) Simplified design stress-strain relationship of concrete in tension 30
Figure 3.3: Constitutive model adopted for plain concrete in compression and tension 32
Figure 3.4: Constitutive law for SFRC in tension 34
Figure 3.5: Characteristic stress-strain and cracking behavior of SHCC 35
Figure 3.6: Constitutive model for steel 37
Figure 3.7: Stress-strain relationship of FCRC 41
Figure 3.8: Predicted stress-strain behavior for FCRC pile with homogenous strengthening 46
Figure 3.9: Predicted stress-strain behavior for FCRC pile with heterogenous strengthening. 46
Figure 3.10: Schematic representation of the constitutive model adopted for confined concrete 47
Figure 4.1: Shear Truss Analogy 50
Figure 4.2: Geometrical illustration of the compression zone 55
Figure 4.3: Flexural Analysis to determine neutral axis and effective depth 55
Figure 4.4: Definition of web width 58

Figure 4.5: a) Geometry of the strengthened cross-section b) Definition of the equivalent rectangular section 59
Figure 4.6: Truss model representation of a strengthened pile 60
Figure 4.7: Flexural analysis to determine the neutral axis depth of circular strengthened sections 61
Figure 4.8: Geometry of the circular strengthened pile section 65
Figure 5.1: Geometrical details of the assessment configurations 70
Figure 5.2: N-M interaction comparison of the as-built pile (ABOP) with the deteriorated unstrengthened sections at 25% (DTP25) and 50% (DTP50) corrosion level 72
Figure 5.3: N-M interaction diagram for repair configurations STPC35 and STPC60, with plain concrete cover repair at 25% corrosion level 73
Figure 5.4: N-M interaction diagram for repair configurations STPC35 and STPC60, with plain concrete cover repair at 50% corrosion level 74
Figure 5.5: N-M interaction diagram for SFRC cover repair with performance classes (3a-8e), compared against the plain C60 cover (PC60), at 25% corrosion level 75
Figure 5.6: N-M interaction diagram for SFRC cover repair with performance classes (3a-8e), compared against the plain C60 cover (PC60), at 50% corrosion level. 76
Figure 5.7: N-M interaction comparison of the plain C60 cover repair with and without longitudinal GFRP bar reinforcement, at 25% and 50% corrosion level. 78
Figure 5.8: N-M interaction diagram of unconfined (UPC35, UPC60) and FRP-confined (CPC35, CPC60) repaired sections at 25% corrosion level 79
Figure 5.9: N-M interaction comparison of unconfined (UPC35, UPC60) and FRP-confined (CPC35, CPC60) repaired sections at 50% corrosion level 80
Figure 5.10: N-M interaction comparison of the SHCC-strengthened section (SHCC35) with the plain-concrete repairs STPC35 and STPC60, at 25% corrosion level 81
Figure 5.11: N-M interaction comparison of the SHCC-strengthened section (SHCC35) with the plain-concrete repairs STPC35 and STPC60, at 50% corrosion level 82
Figure I. 1: Geometrical representation of the compression zone 105
Figure I. 2: Geometrical relationship between the centroid of segment and the neutral axis 107
Figure II. 1: Axial load distribution in the strengthened pile section 108

LIST OF TABLES

Table 3.1: Constitutive model parameters for plain concrete grades C35 and C60..... 32

Table 3.2: Residual tensile and strain properties of SFRC for different performance classes 35

Table 3.3: Constitutive model properties for SHCC..... 36

Table 3.4: Constitutive model properties for the longitudinal reinforcing steel..... 38

Table 3.5: Summary of FRP Material Properties..... 39

Table 3.6: Constitutive model properties for FCRC 48

Table 4.1: Properties for the plain concrete and SFRC strengthening 65

Table 4.2: Properties of the steel reinforcement 65

Table 4.3: Properties of the GFRP reinforcement 66

Table 4.4: Summary of the predicted shear strengthening results..... 66

Table 5.1: Summary of the predicted shear strengthening results..... 70

LIST OF ABBREVIATIONS AND SYMBOLS

Abbreviations

ACI	American Concrete Institute
AE	Acoustic Emission
ASTM	American Society for Testing and Materials
BFRP	Basalt Fiber-Reinforced Polymer
BS	British Standard
CEN	European Committee for Standardization
CFRP	Carbon Fiber-Reinforced Polymer
CMOD	Crack Mouth Opening Displacement
CO_2	Carbon Dioxide
CP	Cathodic Protection
Cl^-	Chloride ions
DIC	Digital Image Correlation
DOCROS	Design of Cross-Sections
DOM	Design-Oriented Model
EC2	Eurocode 2 (EN 1992-1-1)
EIS	Electrochemical Impedance Spectroscopy
EN	European Standard (Norm)
FBG	Fibre Bragg Grating
FCC	FRP-Confined Concrete
FCRC	FRP-Confined Reinforced Concrete
FRC	Fibre-Reinforced Concrete
FRP	Fibre-Reinforced Polymer

Fe	Iron
Fe^{2+}	Ferrous Iron
GFRP	Glass Fibre-Reinforced Polymer
GPR	Ground-Penetrating Radar
HCP	Half-Cell Potential (mapping)
LPR	Linear Polarization Resistance
NDT	Non-Destructive Testing
O_2	Oxygen
prEN	Draft (pre-standard) European Standard
RC	Reinforced Concrete
SFRC	Steel Fiber-Reinforced Concrete
SHCC	Strain-Hardening Cementitious Composite
SSFRC	Strain-Softening Fiber-Reinforced Concrete
UPV	Ultrasonic Pulse Velocity
UV	Ultraviolet

Symbols

A_c	Cross-sectional area of concrete
A_f	Cross-sectional area of FRP reinforcement
A_s	Cross-sectional area of steel reinforcement
A_{sw}	Cross-sectional area of transverse (shear) reinforcement
D	Diameter of the circular/octagonal pile cross-section
E_a	Elastic modulus of the adhesive
E_{cm}	Mean secant modulus of elasticity of concrete
E_f	Elastic modulus of FRP
E_s	Elastic modulus of steel

E_{sh}	Strain-hardening modulus of steel
L	Length
M	Bending moment
M_{Ed}	Design value of the applied bending moment
M_{Rd}	Design value of the flexural moment resistance
N	Axial (normal) force
N_{Ed}	Design value of the applied axial force
N_{Rd}	Design value of the axial resistance
V_{Rd}	Design value of the total shear resistance
$V_{Rd,c}$	Design value of the concrete contribution to shear resistance
$V_{Rd,e}$	Design value of the shear resistance of the existing core domain
$V_{Rd,s}$	Design value of the shear resistance of the strengthening domain
b_w	Width effective web width of the equivalent rectangular section
$b_{w,eq}$	Equivalent effective width of the transformed circular section
d	Effective depth
$d_{l,eq}$	Equivalent effective depth of the longitudinal reinforcement
f_{c0}	Unconfined compressive strength of the concrete core
f'_{cc}	Confined compressive strength of concrete
$f_{c,eq}$	Equivalent compressive strength of a heterogeneous confined section
f_{cd}	Design value of the concrete compressive strength
f_{ck}	Characteristic compressive strength of concrete
f_{cm}	Mean compressive strength of concrete
f_{ctm}	Mean tensile strength of concrete
f_{Fts}	Serviceability residual tensile strength of SFRC
f_{Ftu}	Ultimate residual tensile strength of SFRC

f_{fu}	Ultimate tensile strength of FRP
$f_{R,1k}$	Characteristic residual flexural tensile strengths of SFRC at CMOD1
$f_{R,3k}$	Characteristic residual flexural tensile strengths of SFRC at CMOD3
f_{yd}	Design yield strength of steel
f_{yk}	Characteristic yield strength of steel
n	Number of FRP layers
r	Radius of the circular cross-section
s	Pitch (spacing) of the transverse spiral reinforcement
t_f	Thickness of the FRP layer
z	Internal lever arm
γ_s	Partial safety factor for steel
ε_c	Concrete compressive strain
ε_{ccu}	Ultimate compressive strain of FRP-confined concrete
ε_{cu}	Ultimate compressive strain of unconfined concrete
ε_f	Ultimate strain of the FRP laminate
ε_{fu}	Ultimate tensile strain of FRP
ε_{sy}	Yield strain of steel
ε_{ud}	Design ultimate strain of prestressing steel

THIS PAGE WAS INTENTIONALLY LEFT BLANK

1. INTRODUCTION

1.1. Background and Motivation

Compared to other building materials, concrete is more widely used in the construction industry, with approximately 3 tonnes used per year for every person in the world [1]. This is due to the ready availability of its constitutive materials including aggregates, cement, water and sand. Concrete is naturally strong in compression, with its tensile strength accounting for about 8-14% of its compressive strength [2]. As a result, concrete is usually reinforced with steel, which is naturally strong in tension, to create a composite material that leverages the individual strength properties of both the concrete and steel. In some applications, the reinforcing steel embedded in concrete is prestressed before or after casting the concrete, creating a superior material with enhanced resistance to cracking, bending, shear and torsional properties. In coastal and offshore areas with weak soils, concrete piles, in prestressed or passive state, are commonly adopted as deep foundation supports offering stability for load transfer. They anchor essential marine and waterfront structures like docks, bridges, seawalls, and piers to sea beds.

The structural performance, long-term durability, and safety of reinforced concrete (RC) structures during their service life is governed not only by the mechanical design provisions implemented at the time of their construction, but also the progressive changes in the material properties over time. These RC structures are exposed to various environmental and loading conditions, including changing temperatures, humidity, and chemical components that progressively contribute to the deterioration of both the mechanical and material properties of RC. Corrosion of steel reinforcements is a common cause for the deterioration of RC infrastructure globally, especially in coastal marine environments. Tidal cycling, elevated chloride and carbon concentrations, and high humidity tend to create ideal conditions for the initiation and propagation of corrosion.

The economic impacts of corrosion damage to civil infrastructure are substantial and have been well documented. In the United States alone, the direct cost of corrosion to highway bridges has been estimated at several billion dollars annually, relative to the global cost

estimated at US $2.5 trillion [3], with indirect costs arising from traffic disruption, accelerated replacement cycles, and emergency interventions. Corrosion-related damage imposes a disproportionate amount of financial burden on the maintenance and preservation of existing infrastructure in tropical, coastal, and industrial environments where the aggressive species such as chlorides, carbons, and sulphates thrive.

The repair of corrosion-damaged RC has been an active area of applied research and field engineering, driven by the recognition that replacement as a historically dominant approach, is often prohibitively expensive, disruptive to essential transportation links, and environmentally costly compared to in-situ repair and strengthening. The use of Fiber Reinforced Polymer (FRP) composites for the repair, strengthening and retrofitting of RC structures has become widely studied and applied in civil engineering applications. FRP systems offer a compelling combination of benefits including structural confinement which increases the compressive capacity and ductility of existing concrete, and barrier protection which reduces the ingress of oxygen, moisture, and chlorides to the corroding steel surface.

The assessment of FRP repair and strengthening techniques for RC structures requires not only field applications, but also rigorous analytical prediction of the structural capacity of the RC member considering the as-built, deteriorated, and repaired conditions. Such analytical work, conducted along with destructive experimental testing, provides theoretical framework against which test results are subsequently evaluated and calibrated, enabling the identification of the most critical parameters governing the structural response. The methodology used in this work is layered sectional analysis, implemented within the DOCROS (Design of Cross-Sections) software platform developed at the University of Minho [4]. This approach offers a rigorous, physically grounded framework for nonlinear cross-sectional analysis under combined axial and flexural loading, and is particularly well suited to the complex material configurations of the RC cross-section.

1.2. The Earl C. Davis Memorial Bridge and Harkers Island Bridge

Built in 1968 to replace an old wooden bridge, the Earl C. Davis Memorial Bridge and Harkers Island Bridge provided major vehicular access between the mainland of Carteret County and Harkers Island (see **Figure 1.1**), particularly acting as a hurricane evacuation route for the

residents of Harkers Island. The bridge comprised two key sections, a swing-span movable bridge (Earl C. Davis Memorial Bridge, Carteret Country Bridge No. 73) and the Carteret County Bridge No. 96 [5]. According to the North Carolina Department of Transportation (NCDOT), the area of the state is classified as highly corrosive due to the aggressive marine environment conditions. Therefore, after decades of salt-spray exposure and tidal moisture, the swing span bridge was severely corroded, while Bridge No. 96 was functionally obsolete as the steel prestressing strands in the existing concrete piles were extremely corroded. The bridge was therefore designated as structurally deficient and set apart for replacement by NCDOT.



Figure 1.1: The Earl C. Davis Memorial Bridge with new access bridge at time of construction [6]

The bridge replacement project involved the construction of a new, wider replacement bridge on an adjacent alignment, after which the original Earl C. Davis Memorial Bridge was fully demolished. As part of the replacement project of the Harkers Island Bridge, 9 of the original prestressed concrete pile samples were extracted from the bridge substructure and preserved for study purposes. Each extracted specimen represents a complete cross-section of the pile as fabricated, placed in service, subjected to real structural and environmental loading throughout the service life of the bridge, and ultimately decommissioned without laboratory intervention, constituting a primary experimental resource for the multi-phase research

programme of which this dissertation forms the first analytical phase. Details of the as-built pile properties, including material properties and reinforcement layout, were provided from the original structural drawings provided to the research team at North Carolina State University in collaboration with the University of Minho, informing the assessment considerations adopted in this work in accordance with the conditions of the specimen.

1.3. Thesis Objectives

The general aim of this dissertation is to develop and apply a validated analytical framework for predicting the flexural and shear capacity of deteriorated and FRP-repaired steel-prestressed concrete piles, using the Earl C. Davis Memorial Bridge piles at Harkers Island, North Carolina, as the reference case study. The main objectives of this thesis are as follows:

- To develop a generic sectional analysis tool, following the layered sectional approach implemented within the DOCROS software, to predict the flexural behaviour and capacity of the piles before and after strengthening.
- To apply the developed sectional analysis tool to systematically predict the flexural behaviour and capacity of the pile cross-section in the as-built undamaged state, the damaged state considering two prescribed corrosion-induced deterioration states corresponding to 25% and 50% loss of longitudinal reinforcement cross-sectional area accompanied by concrete cover removal; and the strengthened rehabilitation states encompassing cover reconstruction with comprehensive cementitious matrix and FRP strengthening solutions.
- To develop an analytical shear model for circular strengthened RC sections, superposing the shear resistance of the existing deteriorated core and the new strengthening cover, each combining a critical-shear-crack-theory concrete contribution and a transverse reinforcement contribution, with explicit and physically consistent treatment of the influence of axial load relating to the neutral axis position and the compressive stress field.
- To apply the flexural and shear analytical tools developed in this work to the Earl C. Davis Memorial Bridge pile case study, systematically predicting the combined axial-flexural and shear capacity of the pile cross-section in its as-built state; in two

prescribed corrosion-induced deterioration states, corresponding to 25% and 50% loss of longitudinal or transverse reinforcement cross-sectional area, accompanied by loss of the original concrete cover; and in a comprehensive set of strengthened and rehabilitated states, encompassing cover reconstruction with plain concrete of different compressive strengths, steel-fibre-reinforced concrete across multiple performance classes, glass-fibre-reinforced polymer longitudinal bar reinforcement, and external confinement using carbon-FRP jackets.

- To evaluate, on a consistent and comparable analytical basis, the relative structural effectiveness of the different repair and strengthening strategies considered, in order to identify the mechanical pathway through which each strategy contributes to capacity restoration.

1.4. Structure of Dissertation

This dissertation is organised into six chapters, structured to progress from the motivating problem and the relevant state of the art, through the development of the analytical tools required for flexural and shear capacity assessment, to their application to the Harkers Island pile case study and the conclusions and recommendations that follow from the results obtained.

Chapter 1 introduces the motivation for the dissertation, situating the problem of corrosion-induced deterioration of marine prestressed concrete piles within its broader durability, economic and repair-technology context, before stating the general aim and specific objectives pursued in this work and outlining the structure of the remaining chapters.

Chapter 2 presents a state-of-the-art review of the materials and techniques for the repair of corroded RC structures as: the fundamental mechanisms of chloride-induced and carbonation-induced corrosion of steel in concrete; the inspection, diagnosis and quantification of corrosion damage in reinforced concrete piles, covering visual assessment, non-destructive testing methods including half-cell potential mapping, linear polarization resistance, electrochemical impedance spectroscopy and ground-penetrating radar, and complementary techniques for quantifying section loss and cracking; the materials and techniques currently available for the retrofitting of corroded piles, including conventional

repair approaches and FRP systems; and the specific challenges and solutions associated with the application of FRP repair systems to piles in wet and underwater service conditions, including wet lay-up systems with underwater-curing resins, pre-fabricated FRP shell and jacket systems, and hybrid FRP-cathodic protection systems.

Chapter 3 develops the analytical framework for the layered sectional analysis of the flexural capacity of the deteriorated and strengthened piles, implemented within the DOCROS software platform. The chapter presents the fundamental assumptions and the section discretisation procedure, the equilibrium and compatibility conditions governing the moment-curvature and axial load-moment interaction analysis, and the constitutive models adopted for each material present in the cross-section: plain concrete, steel-fibre-reinforced concrete, strain-hardening cementitious composites, prestressing steel, and fibre-reinforced polymers, culminating in the design-oriented confinement model adopted for FRP-confined reinforced concrete sections, including the treatment of heterogeneous (core-and-cover) confined sections.

Chapter 4 develops the analytical framework for the shear capacity assessment of the deteriorated and strengthened circular and octagonal pile sections, a problem for which, as discussed in this introductory chapter, no equally mature closed-form solution exists in the literature. The chapter presents the fundamental governing equations for shear resistance, including the influence of axial load, before introducing the specific procedure adopted for shear prediction in circular sections, encompassing the determination of the neutral axis and effective depth and the equivalent-rectangle idealisation used to establish the transverse reinforcement efficiency. The original two-domain analytical model proposed in this dissertation is then formulated, superposing the shear resistance of the existing and strengthening domains, and the chapter concludes with the design application of the model to the Harkers Island pile case study across the full matrix of corrosion levels, reinforcement configurations, and cover materials considered in this work.

Chapter 5 applies the analytical frameworks developed in Chapters 3 and 4 to the specific problem of capacity prediction for the Harkers Island piles, presenting and discussing the flexural (axial load-moment interaction) results for the as-built, deteriorated and strengthened configurations, followed by the discussion of the shear capacity results obtained from the model presented in Chapter 4, examined across the different corrosion levels,

reinforcement locations, cover materials and axial load levels considered, and closing with a comparative synthesis of the relative effectiveness of the different strengthening strategies evaluated.

Chapter 6 presents the main conclusions drawn from the analytical developments and case-study results of the preceding chapters, summarising the principal findings for both flexural and shear capacity assessment and their implications for repair strategy selection, and closes with recommendations for further developments, in particular the experimental and finite element validation required to confirm and refine the proposed analytical shear model and the broader flexural and confinement framework developed in this dissertation

.

THIS PAGE WAS INTENTIONALLY LEFT BLANK

2. STATE-OF-THE-ART MATERIALS AND TECHNIQUES FOR THE REPAIR OF CORRODED RC STRUCTURES

2.1. Fundamentals of Steel Corrosion in Concrete

Steel in concrete is protected by a passive oxide film at the steel-concrete interface, which comprises of a highly stable layer of iron oxides and hydroxides in the highly alkaline concrete pore solution produced during cement hydration. Corrosion is initiated when this passivating layer is chemically destabilized, either by a progressive reduction in the pH of the pore solution through carbonation or by the local accumulation of chloride ions beyond a critical threshold concentration at the steel surface [7]. Fundamentally, corrosion of steel in concrete is an electrochemical process involving the paired loss of electrons from Fe (oxidation) at the anodic zones and the gain of electrons by dissolved O_2 (reduction) at cathodic zones. The concrete pore solution acts as an ionic electrolyte, enabling these reactions. The anodic reaction produces ferrous ions (Fe^{2+}), which move through the pore solution. These ions are further oxidized, creating bulky corrosion products which expand and build up internal tensile stresses causing cracking and spalling of the concrete cover. This damage of the concrete cover accelerates the ingress of aggressive substances, leading to further corrosion damage [8].

2.1.1. Chloride-Induced Corrosion

Chloride-induced corrosion is a dominant deterioration mechanism for concrete structures in coastal and marine environments [9]. Chloride ions (Cl^-) penetrate concrete mainly by diffusion through cracks and pores, which is influenced by the chloride concentration gradient between seawater and the concrete pore solution. Capillary absorption during wetting and drying cycles also contributes to chloride ingress into RC structures. When chloride concentration at the rebar surface exceeds the critical threshold, typically 0.2% to 1.0% by mass of binder for ordinary reinforcement, and lower for high-strength prestressing steel, the breakdown of the passive film occurs, and corrosion begins [10]. This mechanism is illustrated schematically in **Figure 2.1**. Romain et al [7]. reported that the extent of corrosion damage,

whether uniform or localized pitting corrosion, was highly dependent on the chloride content level contributing to de-passivation. Localized pitting corrosion was more likely to occur at high chloride contents, while uniform corrosion occurred at low chloride content.

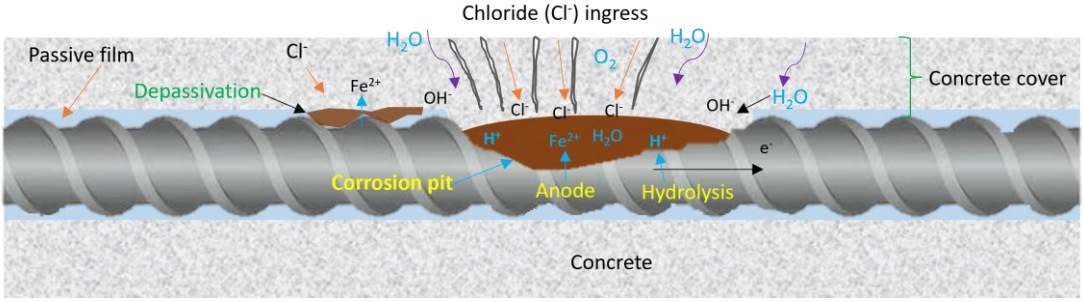


Figure 2.1: Schematic representation of chloride-induced corrosion

The performance of RC structures in marine environments depends on different exposure zones, illustrated in **Figure 2.2**. The submerged zone is generally the least aggressive for corrosion because oxygen is limited, even though chloride concentrations are high. The tidal zone is subjected to cyclic wetting and drying, creating ideal conditions for abrasion, pronounced chloride ingress by capillary action and biological growth. Studies report that this zone exhibits the highest corrosion rates in practice, thereby demanding the strongest protection systems [11]. The splash and spray zones provide intermittent wetting with frequent drying. Continuous wave action, salt spray, and high oxygen availability at the splash zone significantly accelerate corrosion, and concrete deterioration. The atmospheric zone is exposed to moisture, UV radiation, temperature fluctuations and airborne chloride deposition, which diminishes in intensity with distance from the shoreline [12].

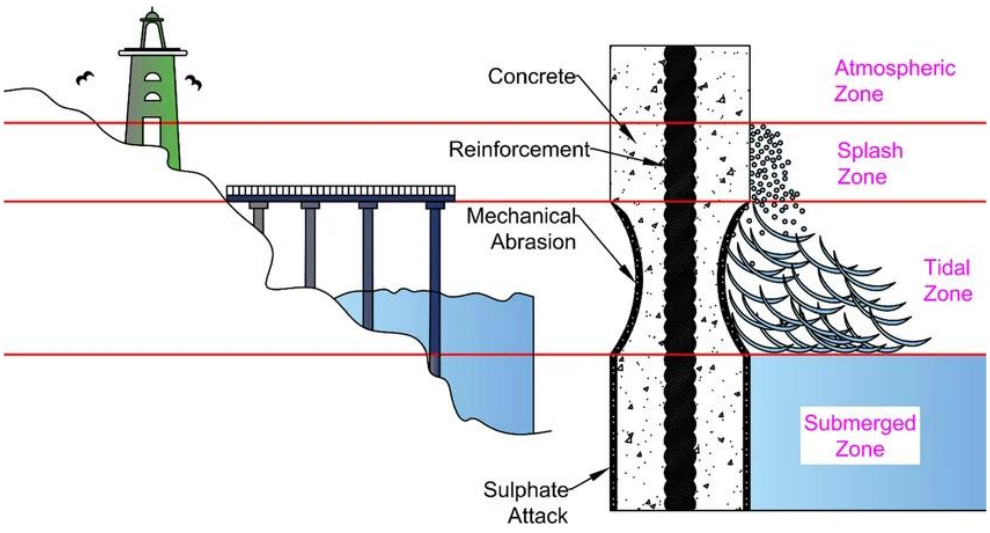


Figure 2.2: Exposure zones in marine structures [13]

The corrosion-dependence of chloride diffusivity on the exposure zone is well documented. Qu et al [11], [13] summarized diffusion coefficients for cement-based concrete across all four zones. The tidal zone shows coefficients up to 5-8 x 10^{-12} m^2/s for ordinary Portland cement at water-cement ratios of 0.5-0.65. Submerged and atmospheric zones have lower coefficients due to saturation and reduced surface chloride concentrations, respectively. Mineral admixtures like fly ash and silica fume significantly reduce the chloride diffusion coefficients, sometimes by over 50%, highlighting the crucial role of mix design in durable marine structures [14].

2.1.2. Carbon-Induced Corrosion

Carbonation-induced corrosion occurs when atmospheric CO_2 penetrates concrete via absorption and diffusion through interconnected capillary pores and microcracks, as illustrated in **Figure 2.3**. The CO_2 dissolves in pore water to form carbonic acid, which dissociates to HCO^{3-} and CO_3^{2-} and reacts with Calcium (Ca) bearing hydrates (portlandite, CSH, ettringite), progressively decalcifying the paste and precipitating $CaCO_3$. This carbonation process advances fastest at 50-70% RH and in high water to cement ratios, cracked, or otherwise more porous regions, so it is typically non-uniform around the reinforcement. Once the carbonation front reaches the steel depth, the pH of the pore solution drops below 9, dissolving the passive film and leaving the steel vulnerable to corrosion.

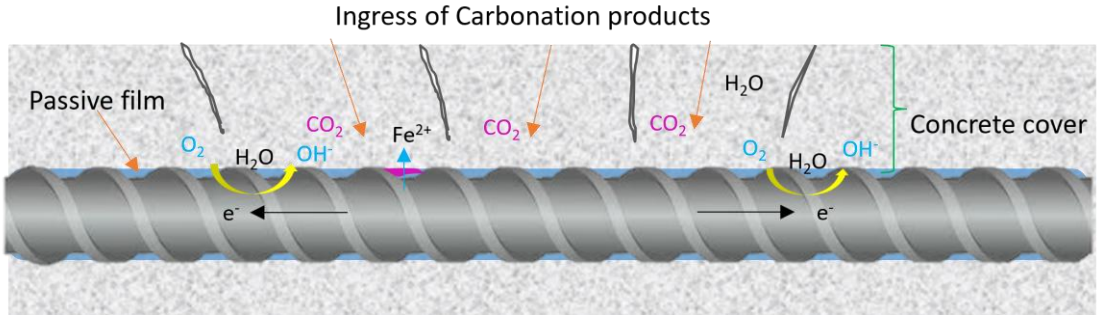


Figure 2.3: Carbon-induced corrosion

2.2. Inspection and Diagnosis of Corrosion in RC Piles

Conducting reliable and comprehensive assessment of the state of corrosion and structural condition of RC is a fundamental requirement for rational decision making in rehabilitation of

RC structures. Inspection of RC structures in marine environments with tidal and submerged zones presents unique practical challenges rarely encountered in conventional infrastructures. Access to underwater sections is difficult, substrates are often saturated, and marine organism colonization (algae, barnacles) on concrete surfaces obscures visual inspection and must be mechanically removed before non-destructive testing (NDT) measurements are taken. The most critical corrosion zones may be concentrated in the underwater or tidal region, where visual inspection is limited or impossible. A well-structured inspection program typically proceeds in three stages: preliminary visual survey, non-destructive testing (NDT), and confirmatory laboratory testing of extracted cores or reinforcement specimens.

2.2.1. Visual Inspection and Preliminary Assessment

Visual inspection remains the most basic and widely practiced approach for preliminary assessment of in-service concrete structures. The common visual indicators of corrosion in RC structures include surface cracks, rust stains at crack locations, concrete spalling and delamination, and section loss or discoloration at the water line. Carino et al. [15] emphasized that while visual inspection can confirm corrosion-induced damage, it systematically underestimates the true extent of deterioration. The corrosion front may be well advanced of the first visible surface manifestations. For underwater inspections, remotely operated vehicles (ROVs) equipped with high-definition cameras and light sources are increasingly being used, which are supplemented by tactile inspection by commercial professional divers where substrate conditions allow [16].

2.2.2. Non-Destructive Testing (NDT) Methods

Given the limitations of visual inspection, a range of electrochemical, electromagnetic, and wave-propagation NDT methods have been developed and applied to assess reinforcement corrosion without destructive intervention. Hu et al. [17] provided a comprehensive review of these methods, classifying them into direct and indirect methods. Direct methods measure corrosion parameters such as electric potential and current density, while indirect methods measure concrete resistivity, chloride content, or carbonation depth from which corrosion risk

is inferred. The common NDT techniques used for measuring corrosion in concrete are discussed below:

2.2.2.1. Half-Cell Potential Mapping

Half-cell potential (HCP) measurement is a widely used NDT technique for in-field assessment of active corrosion. The method measures the open-circuit potential of the reinforcing steel relative to a reference electrode placed on the concrete surface. Carino et al. [15] and Hu et al. [17], reported that regions with lower potential readings indicated a high probability of active corrosion. HCP mapping produces equipotential contour plans that identify the spatial distribution of anodic zones, making it particularly valuable for prioritizing repair intervention on large structural surfaces. However, HCP provides no direct information on corrosion rate, and may yield unreliable results in highly resistive concrete, in fully saturated submerged elements, and in cracked sections where the electrochemical boundary conditions are locally disturbed. Pfändler et al. [18] demonstrated a novel underground inspection probe that combines HCP mapping with steered horizontal drilling technology for inaccessible pile surfaces and confirmed that corroding zones of practically relevant size can be detected at distances of 250 mm from the reference electrode to the steel surface, highlighting the advancement in technology for assessment of concrete structures in complex environments.

2.2.2.2. Linear Polarization Resistance and Electrochemical Impedance Spectroscopy

Where a quantitative estimate of corrosion rate is required, polarization resistance techniques are employed. The linear polarization resistance (LPR) method applies a small perturbation potential (typically ±10-20 mV) around the corrosion potential and measures the resulting current; the corrosion current density i_{corr} is calculated from the Stern-Geary relationship. Alonso et al. [19] established threshold values for i_{corr} to classify corrosion activity such that values below 0.1 µA/cm^2 were considered passive, 0.1-0.5 µA/cm^2 indicated low corrosion activity, 0.5-1.0 µA/cm^2 corresponded to moderate activity, and values exceeding 1.0 µA/cm^{2}indicated high corrosion activity. Electrochemical impedance spectroscopy (EIS) provides detailed insight into the condition of the passive film and the electrochemical behaviour of the steel-concrete interface through equivalent circuit modelling. However, its

application is largely limited to laboratory environments due to the complexity of data interpretation and the requirement for controlled testing conditions [17].

2.2.2.3. Ground Penetrating Radar

Ground penetrating radar (GPR) is an electromagnetic NDT technique that transmits high-frequency radar pulses into concrete and records reflections from interfaces between materials of contrasting dielectric properties. In RC structures, GPR is commonly used to map rebar location and concrete cover depth, to identify voids and delamination, and to detect elevated moisture content that may indicate chloride ingress pathways. Hu et al. [17] noted that corrosion induced changes in the dielectric properties of concrete around corroding bars can be detected by GPR, providing spatially continuous information that HCP mapping alone cannot capture.

Other testing techniques such as Ultrasonic pulse velocity (UPV) provide rapid assessment of concrete quality and homogeneity, while acoustic emission (AE) monitoring can detect active crack propagation associated with the expansive pressure of corrosion product formation in near-real time [20]. Impact-echo testing is effective for detecting delamination and near-surface voids and has been successfully applied in bridge deck and pile condition assessments. The combination of multiple NDT techniques provides a substantially more reliable diagnosis than any single method used in isolation.

2.3. Techniques to Quantify Corrosion in RC Structures

Determination of effective repair design of corroded RC structures not only demands the detection of corrosion activity, but also the quantification of the extent to which the corrosion damage has occurred. This includes the assessment of dissipation of corroding agents, evaluation of the residual cross-sectional area of reinforcement, spatial distribution of corrosion damage, local degradation of concrete mechanical properties, the influence of corrosion on the bond properties between the concrete and steel reinforcement, and the current corrosion rate. Both field and laboratory techniques contribute to this quantification, often in a complementary manner.

2.3.1. Chloride Profiling

As discussed in Section 2, introduction of chlorides into the RC material leads to the de-passivation of the protective film at the steel-concrete interface, thereby initiating steel corrosion. Therefore, when assessing corrosion damage in RC structures, it is important to determine the rate of chloride ingress and its dissipation into the material. The standard approach to characterizing chloride ingress into concrete involves the measurement of the total (acid-soluble) and free (water-soluble) chloride content as a function of depth from the exposed face. Drilled powder samples or thin-sliced cores are extracted and analysed by potentiometric titration, ion chromatography, or the Volhard method. The resulting chloride depth profile is fitted to Fick's second law of diffusion to extract the apparent diffusion coefficient (D_a) and the surface chloride concentration (C_s), which serve as the primary parameters for service life predictions [12]. In tidal zone environments, both D_a and C_s are time-dependent, with D_a typically decreasing as secondary hydration products reduce porosity and C_s increasing as marine organisms and evaporation concentrate chlorides at the surface. Qu et al. [11] compiled and compared the data for diffusion coefficient across various exposure zones, noting that tidal zone concrete showed the highest C_s values and, consequently, the highest chloride ingress rates, consistent with the observed concentration of corrosion damage in this zone on extracted bridge piles.

2.3.2. Gravimetric Mass Loss Measurement

The most direct and reliable measure of corrosion severity in extracted specimens is by establishing gravimetric mass loss, where the difference in mass between the original uncorroded steel and the cleaned, corroded section, is expressed as a percentage of the original mass. ASTM International G1 [21], prescribes a standard practice for preparing and chemical cleaning to remove corrosion products without attacking the base metal. In prestressing strands, this technique is applied to each wire individually, as corrosion is frequently localized and pitting depths can vary significantly along the strand length. González et al. [22] highlighted that the maximum pit depth, rather than average mass loss, governs residual tensile strength and fracture probability in prestressing wires. This is a consequence of the stress concentration factors introduced by pitting that can precipitate wire fracture at loads well below those predicted from uniform section loss models. This is particularly critical

for the assessment of prestressed RC structures that have experienced decades of marine exposure, and localized pitting corrosion on high-stress strands may represent the true governing damage state.

2.3.3. Assessment of Corrosion-Induced Cracking and Cover Spalling

Corrosion-induced cracking and concrete cover spalling are visual indicators of volumetric expansion of corrosion products. The measurement of crack width, crack pattern geometry, and the extent of cover delamination provide indirect but practical information on the level of ongoing corrosion activity and the cumulative loss of cross-sections. Vidal et al. [23] established empirical correlations between crack width and rebar mass loss for naturally corroded beams after long term outdoor exposure, which demonstrated that the relationship is highly dependent on the concrete cover-to-rebar diameter ratio and environmental exposure conditions. Zhuang et al. [24] performed controlled experiments to simulate the cracking behaviour of RC piles exposed to marine tidal cycling, which demonstrated that isolated longitudinal cracks, distributed map cracking, and eventual cover spalling occurred and propagated gradually in distinct exposure zones (tidal, atmospheric, underwater) depending on the level of corrosion, as shown in **Figure 2.4**.

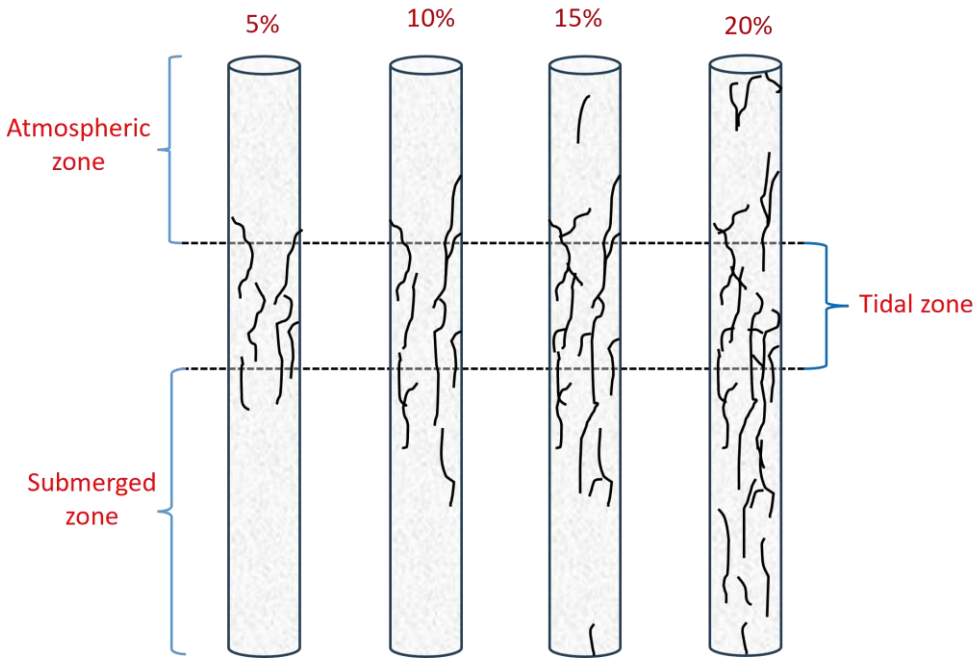


Figure 2.4: Spatial cracking patterns of corrosion damaged concrete at different corrosion level.

The conversion of crack width observations to section loss is, however, less reliable especially where multi-wire strand geometry with the tendency for localized pitting occurs without triggering circumferentially uniform expansive pressure. Identification of spatial cracking patterns (isolated longitudinal cracks vs map cracking vs spalling), on the other hand, remains valuable in distinguishing corrosion mechanisms and damage severity levels.

2.3.4. Photogrammetry, 3D Scanning, and Section Reconstruction

In recent years, the development of close-range photogrammetry and structured light 3D scanning has enabled precise 3D mapping of corrosion damage on extracted reinforcement. Scanning corroded bars or strands before cleaning allows for detailed mapping of pit geometry, pit depth distribution, and section profile variation along the specimen. Integration with digital image correlation (DIC) methods, as reviewed by Andisheh et al. [25], facilitates real-time measurement of surface strain fields during loading of corroded specimens, thereby providing experimental data for calibrating numerical models. These quantification techniques are particularly relevant to research programs involving destructive testing of extracted piles with known service histories, as they offer a unique opportunity to correlate quantified corrosion damage with structural performance.

2.3.5. Structural Health Monitoring and Embedded Sensor Systems

For in-service RC structures, long-term monitoring of the rate of corrosion can be achieved by embedding sensor systems (ESS) within the concrete during construction or subsequent repair. Electrochemical sensors (galvanic or impressed-current probes), embedded reference electrodes, and electrical resistance (ER) probes enable continuous or periodic monitoring of corrosion potential and current density at selected locations [17]. Fiber-optic sensors, including fibre Bragg grating (FBG) networks, provide strain measurements with millimetre-scale spatial resolution and have been used to detect the onset of corrosion-induced cracking in laboratory specimens. Multi-sensor fusion approaches that combine electrochemical, acoustic, and optical data streams, processed by machine learning algorithms, represent the current frontier of structural health monitoring for RC structures in aggressive environments [26].

2.4. Material and Techniques for Retrofitting Corrosion Damaged RC Piles

The decision to rehabilitate rather than replace RC structures affected by corrosion is influenced by the technical feasibility of the repair technique, accessibility constraints, structural condition of the existing structure, and the life-cycle assessment. When repairing RC in marine environments, additional constraints including underwater installation, the necessity for corrosion arrestment in the repaired section, and the need to restore or enhance structural capacity under eccentric axial and lateral loading. These factors collectively define the technical performance envelope for any viable repair system.

2.4.1. Conventional Repair Approaches

Traditional repair of corroded RC involves the removal of deteriorated concrete, treatment or replacement of corroded reinforcement, and restoration of the section geometry using compatible repair mortar or concrete. Sharma et al. [16] reviewed the repair options for corrosion-damaged prestressed concrete bridges, noting that cementitious patch repair with Portland cement-based or polymer-modified mortars remains the most common intervention. However, the long-term performance of patch repairs in prestressed concrete elements has been reported to be unsatisfactory, with failures occurring after three to four years due to renewed cracking and delamination at the corrosion front. This behaviour is mainly attributed to the fact that patch repairs do not eliminate the root cause of deterioration. Residual chlorides remaining in the surrounding concrete continue to promote corrosion in adjacent, unrepaired steel regions. In addition, the electrochemical potential difference between the passive repair zone and the actively corroding surrounding concrete may accelerate corrosion at the repair boundary, a phenomenon known as the incipient anode effect [27]. Alternatively, the technique of cathodic protection (CP) has been applied to bridge substructures, including piles in seawater, due to its potential to arrest ongoing corrosion by shifting the electrochemical potential of the steel into an immune or passive range. Integration of CP with FRP jacketing systems has been investigated as a dual-function repair strategy, exploiting the impermeable jacket as both a structural element and as the anode medium for the CP system.

2.4.2. Fibre-Reinforced Polymer (FRP) Systems

FRP composites are increasingly becoming widely adopted for structural strengthening and retrofitting of deteriorated RC structures, especially corrosion damaged RC elements in marine environments. The principal advantages of FRP for the application in strengthening corrosion damaged RC structures are: high stiffness-to-weight and strength-to-weight ratios; inherent resistance to corrosion; the ability to provide passive confinement that arrests corrosion-induced concrete dilation and restores lost structural capacity; and, critically, the availability of both resin and cementitious grouts that cure effectively under water, enabling installation in wet submerged conditions without elaborate access systems [27].

2.4.2.1. FRP Material Types and Mechanical Properties

FRP composites are made of a polymer matrix (such as epoxy or polyester) reinforced with high-strength fibres. The principal fibre types commonly used in repair applications of deteriorated RC structures include Carbon, Glass, and Basalt fibres, respectively. **Figure 2.5** shows the stress-strain relationship for typical FRPs compared to that of steel prestressing strand and mild steel. Of particular note is the linear-elastic nature of the FRP composites. CFRP offers the highest tensile strength (typically 3400-5000 MPa in the fibre direction) and elastic modulus (230-650 GPa), making it particularly suitable for applications where structural strengthening, confinement, resistance to corrosion and durability are primary objectives. GFRP provides strengthening benefits with lower stiffness at a significantly lower cost compared to CFRP, making it economically attractive for strengthening applications of corrosion damaged RC elements where confinement enhancement rather than flexural strengthening dominates the design. BFRP has attracted growing research interest as a cost-intermediate alternative with better thermal stability and alkaline resistance than GFRP [27]. The durability of FRP composites in marine conditions, specifically resistance to moisture absorption, UV degradation, and seawater chemical attack is highly crucial for applications in bridge substructures. Karbhari et al. [28] and Mullins et al. [29] conducted a durability gap analysis with extensive field observations, establishing that properly applied CFRP systems show no significant degradation in bond or mechanical properties after multiple years of marine exposure, provided that surface preparation achieved intimate contact between the FRP and the concrete substrate.

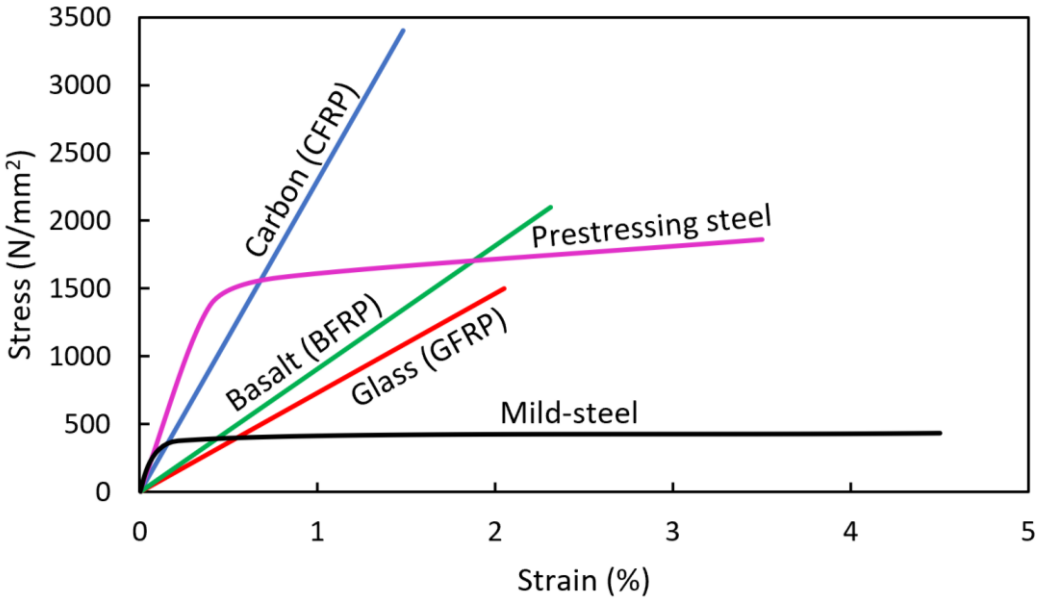


Figure 2.5: Tensile Properties of FRP material types compared to steel

2.4.2.2. Confinement Properties of FRP systems

The structural enhancement provided by FRP wrapping derives from the passive confinement of the existing concrete. As axial load increases, the concrete dilates and is resisted by the FRP jacket, which develops hoop stresses, imposing a confining pressure on the concrete. This mechanism causes a significant increase in both the peak compressive strength ($f'_{cc}>f'_{c0}$) and the ultimate compressive strain ($\varepsilon_{ccu}>\varepsilon_{cu}$) of the confined concrete relative to its unconfined state [30]. When a RC pile cross-section is repaired and strengthened with FRP, two relevant structural configurations, the concrete core and concrete cover respectively contribute to the overall confinement benefits of the cross-section based on distinct frameworks. The concrete cover zone occupying the annular region is in direct contact with the FRP jacket but receives no lateral support from the spiral, which acts only on the inner region of the concrete core. The concrete core is therefore simultaneously enclosed by both the FRP jacket externally and the spiral internally. These two zones therefore experience fundamentally different confinement effects, and have been researched extensively in previous works. The characteristic stress-strain responses of unconfined concrete, steel-confined concrete, and FRP-confined concrete are illustrated in **Figure 2.6:** .

The theoretical framework for steel confinement by Mander et al. [31] established the relationship for steel-confined concrete, validated extensively across a broad range of column

dimensions, concrete strengths, and reinforcement configurations. For FRP-confined concrete, the governing confinement mechanism differs fundamentally: as FRP composites are linearly elastic to rupture, the lateral confining pressure increases continuously with concrete dilation rather than reaching a fixed yield plateau as in steel spirals, producing a distinct compressive response shown in **Figure 2.6:** .

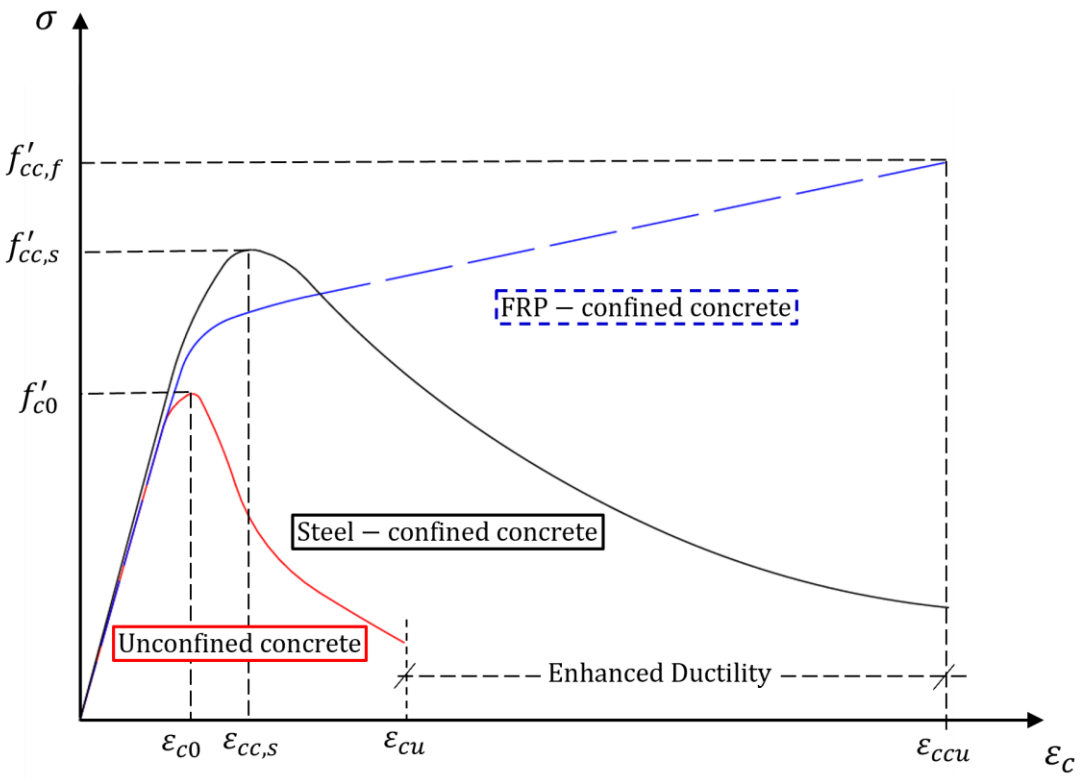


Figure 2.6: Stress-strain relationship for confined and unconfined concrete

This phenomenon led to the development of numerous design-oriented constitutive models, with the Lam and Teng [32] being widely adopted in both ACI PRC-440.2R [33] and fib Bulletin 14 [30] and refined by Teng et al. [34] on the basis of an expanded experimental database. Considering the combined FRP-and-steel confinement configuration relevant to FRP-wrapped RC columns with internal spiral reinforcement, Lin et al. [35] demonstrated that the dual confinement mechanism produces a response distinct from either system acting alone. Subsequently, Shayanfar et al., [36] proposed the most statistically comprehensive design-oriented model for this FRP-confined RC column (FCRC) case, calibrated against 97 independent experimental results. This model is adopted in the present work for all CFRP strengthened pile scenarios and is discussed in Chapter 3.

2.4.3. FRP Repair Systems for Piles in Wet and Underwater Conditions

The installation of FRP systems in submerged or tidal zones faces a series of challenges absent from conventional above-water applications. These include: the difficulty in achieving a dry substrate for conventional epoxy resin application; reduced working time due to heat dissipation in cold water; and the presence of marine growth that must be removed before FRP can bond to or contact the concrete surface [29], [37]. The common techniques deployed in the industry including wet lay-up and FRP jacketing solutions are shown in the **Figure 2.7**.

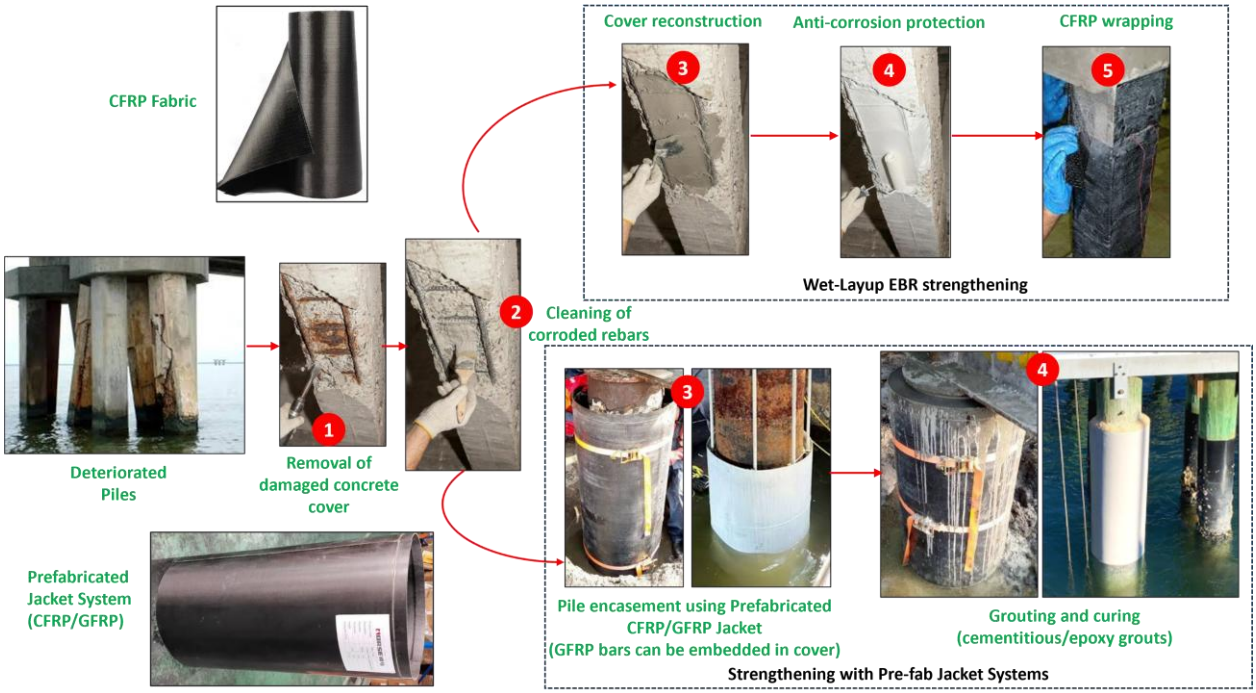


Figure 2.7: FRP strengthening techniques in marine environments

2.4.3.1. Wet Lay-Up Systems with Underwater-Cure Resins

Wet lay-up FRP systems use a fibre fabric (unidirectional or bidirectional) that is impregnated with a thermosetting resin (typically epoxy or vinylester), which cures in the presence of moisture or when fully submerged. Sen et al. [29] demonstrated the feasibility and durability of underwater FRP wrapping in multiple field demonstration projects on corroding RC and prestressed piles in the tidal waters of Tampa Bay, Florida, including the Friendship Trail Bridge and the Allen Creek Bridge. Their study systematically compared wet lay-up and pre-impregnated systems, evaluating both corrosion suppression and structural performance. Corrosion rate measurements in wrapped piles exhibited consistently low, stable values,

compared to the progressive increase observed in the unwrapped control piles over a two-year monitoring period. Long-term bond testing conducted 2 years after installation confirmed adequate FRP-concrete adhesion for both systems despite challenging installation conditions. However, the practical application of wet lay-up FRP to RC structures in tidal and submerged environments is generally more complex and less controllable than equivalent above-water installations. Five critical challenges must be well understood and addressed for better installations; these include: a) achieving a clean, sound substrate is far more difficult due to marine organisms which invade and colonize the concrete surfaces; b) maintaining intimate contact between the saturated FRP fabric and the concrete substrate during the entire resin cure period is critical and extremely difficult on vertical surfaces in water; c) the thermal environment of seawater significantly reduces resin reactivity, extending open times and cure durations while also reducing the peak exothermal temperature; in cold water, some formulations may fail to reach adequate cure without supplementary heating; d) wet lay-up requires on-site fibre saturation, which must be completed within the resin pot-life window, that is already shortened by water contamination and ambient temperature variability; e) in non-circular cross-sections such as the case of octagonal piles, the flat faces and sharp corner geometry impose localized gradient of stresses in the fabric at corner transitions, causing localized stress concentrations that trigger premature failure of the FRP wrap. Providing an adequate corner radius mitigates these gradients, thereby delaying FRP rupture and improving bonding by ensuring continuous, uniform contact with the concrete substrate.

Therefore, surface preparation is a key governing factor for achieving effective FRP-concrete bond in underwater wet lay-up applications. ACI PRC-440.2R [33] recommendations require intimate, continuous contact between the saturated FRP fabric and the concrete substrate during cure; loss of contact at corners or over voids leads to unbonded zones that compromise both confinement effectiveness and corrosion protection. The recommended repair sequence involves: (i) mechanical removal of all marine growth; (ii) repair of major spalled areas using a compatible underwater-curing mortar; (iii) cleaning of the rebar surface, where exposed; (iv) grinding of all corners to a minimum radius of 19 mm (for rectangular and octagonal sections) to prevent premature FRP fracture due to stress concentrations; and (v) application of a compatible primer or conditioning coat when the substrate is saturated but not running wet.

2.4.3.2. Prefabricated FRP Shell and Jacket Systems

Prefabricated FRP shells and jackets are an alternative to wet lay-up for repair of deteriorated RC, particularly in water splash zones and submerged applications. Used in a contact-critical (as opposed to a bond-critical) configuration, the FRP jacket, typically fabricated from glass or carbon fibre, as shown in **Figure 2.8**, encases the RC element in the selected critical zone without adhesive bonding to the concrete substrate; the annular space between the jacket and the existing pile section is filled with underwater-cure cementitious grout or epoxy mortar to restore section geometry and transfer loads. More often, additional reinforcement is incorporated using FRP rebars which are non-corroding, just before the placement of the FRP shell and grouting. This approach increases the capacity of the existing structure to more than the original as-built reinforcement capacity, eliminates the need for dry-substrate bonding conditions, and can be easily installed by specialists even underwater.



Figure 2.8: Strengthening of marine piles with prefabricated GFRP and CFRP jackets

The structural design premise of prefabricated jacket systems is that confinement is provided by the hoop stiffness of the shell, while axial load continuity and concrete section restoration is provided by the grout infill, which is composed of either cementitious material or epoxy resins. FRP jackets physically prevent outward cover spalling under compressive load, ensuring the full gross concrete section remains engaged up to the point of FRP rupture, an additional capacity benefit absent in both the unconfined and conventionally steel-confined cases. The structural design with FRP jackets must therefore account for the confinement

behaviour of the jacket during loading, and possible long-term creep or shrinkage effects on the infill.

2.4.3.3. FRP systems with cathodic protection (CP)

Despite the performance of FRP systems in enhancing the capacity of deteriorated structures, it is widely acknowledged that the technique only reduces the rate of ongoing corrosion by limiting the ingress of oxygen and moisture to the rebar surface, and by restraining the radial expansion of corrosion products that would otherwise contribute to cover cracking and further damage progression. However, FRP alone does not arrest corrosion activity in reinforcement that was already actively corroding at the time of repair: chloride ions already present within the concrete cover will continue to sustain the corrosion cell indefinitely as long as the electrochemical conditions favouring it are not disrupted. Andisheh et al. [25] specifically noted this limitation through multiple experimental studies involving bridge pier rehabilitation, which confirmed that FRP wrapping of already corroded RC structures was reduced, but did not eliminate active corrosion, with residual corrosion rates in wrapped specimens remaining detectable several years after repair [25], [29].

Cathodic protection (CP), on the other hand, is reportedly the only scientifically proven technique known to effectively stop corrosion [38]. As a result, a new method of repairs has been developed and investigated in recent years, combining CP with FRP systems to address the corrosion problem from the root cause. The mechanism of operation is such that the FRP jacket provides structural confinement and physical protection from the external environment, while the CP system shifts the electrochemical potential of the corroding reinforcement into the immune or passive range, thereby arresting the occurring corrosion rather than merely slowing it. Aguiler et al. [38] in their study utilized a sacrificial zinc mesh anode system incorporated within the annular grout space, electrically connected to the reinforcing steel, thereby creating a galvanic CP cell in which the zinc functioned as the sacrificial anode and the corroding reinforcement served as the cathode. The study established that the system was practically deployable in underwater tidal and splash conditions and yielded electrochemical protection criteria consistent with effective corrosion arrest. Therefore, this hybrid approach transforms the FRP repair from a passive barrier and structural intervention to an active electrochemical intervention that directly suppresses the

anodic dissolution of the reinforcing steel by corroding agents. This is of special importance for high-strength prestressed concrete elements, where even modest post-repair corrosion rates acting over decades can result in hazardous pit depths at which stress corrosion cracking or brittle strand fracture failure modes become imminent.

3. Analytical Framework for Flexural and Axial Capacity Assessment of the Deteriorated and Strengthened RC Piles

3.1. Introduction

The structural assessment of the deteriorated reinforced concrete piles requires a robust analytical framework capable of capturing the material behaviour that governs the response of RC cross-sections under combined axial and flexural loading. This chapter presents the theoretical basis of the analysis, constitutive material models, confinement frameworks, and structural performance indicators that together define the analytical methodology adopted in this study.

The methodology is based on layered sectional analysis, in which the cross-section is discretized into a finite number of horizontal layers, each assigned an independent constitutive law. This approach accommodates the complex heterogeneity of repaired pile cross-sections comprising a deteriorated concrete core, various cover repair and strengthening materials, discrete prestressing cables, and in some scenarios an externally bonded FRP confinement wrap. The interactions between these materials, and the way their responses combine to produce the overall sectional capacity, are mediated entirely through the equilibrium and compatibility conditions that the layered model enforces at every loading step.

All constitutive models described in this chapter were selected to reflect the state-of-the-art for each material class, and are implemented within DOCROS (Design of Cross-Sections), a layered sectional analysis software developed at the University of Minho. DOCROS has the potential to analyse sections with complex shapes and sizes, making it highly relevant to the study of the deteriorated octagonal steel prestressed concrete piles utilized in this work. The constitutive laws are implemented through a library of nonlinear material models (NLMMs) present in DOCROS, each capturing a specific material behaviour class presented in the next sections.

3.2. Layered Sectional Analysis

3.2.1. Fundamental Assumptions and Section Discretization

The method of layered sectional analysis is implemented on the basis of the following fundamental assumptions, which have been validated extensively for RC sections subjected to combined axial force and bending moment, that:

- Plane sections remain plane: the strain distribution across the section depth is linear at every loading stage, regardless of the material nonlinearity.
- Perfect bond between materials: full composite action is assumed between concrete layers, steel reinforcement, FRP jacket, and repair materials. Slip-bond behaviour at material interfaces is not modelled.
- Uniaxial stress state: all materials respond in uniaxial compression or tension along the pile axis. Transverse stresses from confinement are accounted for implicitly through the confined material constitutive law, not as an explicit biaxial stress state.
- Monotonic loading: the stress-strain envelopes of all materials represent a monotonic (non-cyclic) response, corresponding to the ultimate limit state assessment.

3.2.2. Section Discretization

The section is discretized by dividing it into multiple horizontal layers of defined thickness and width depending on the cross-section geometry and the existing reinforcement, as illustrated in **Figure 3.1**. The steel and surrounding concrete are modelled as separate material components with widths computed from the respective cross-sectional areas and layer thickness. The chord width (b_{chord}) for each layer is obtained directly from the section geometry, ensuring geometric accuracy across the full section depth.

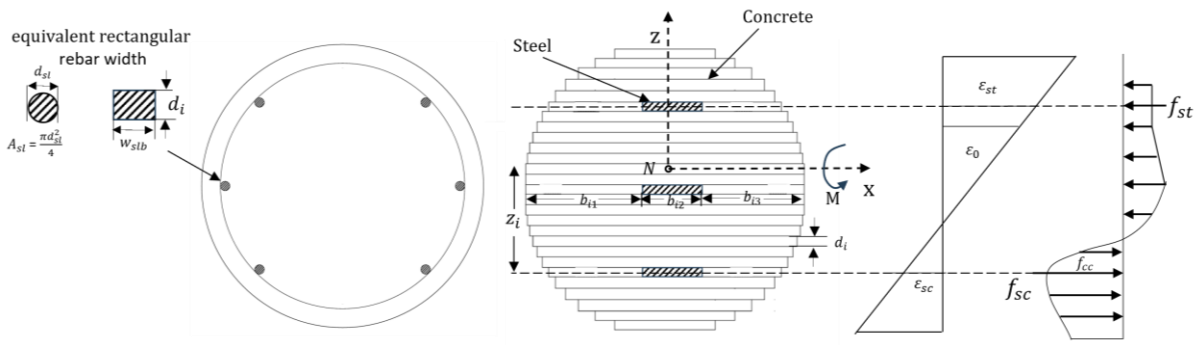


Figure 3.1: Section discretization in DOCROS [4]

The equivalent width (w_{slb}) for each of the longitudinal reinforcement, in either the existing or the strengthening configurations, in their respective layers is computed as: $w_{slb} = \frac{(n_{slb} \times A_{slb})}{d_i}$, where n_{slb} is the number of bars at the same layer or depth, A_{slb} is the cross-sectional area of the reinforcement, and d_i is the layer thickness. This is particularly critical when considering the changes in cross-sectional area of the reinforcing steel due to corrosion damage, where in this work, uniform corrosion was maintained and applied to the area of the existing reinforcing steel.

3.2.3. Equilibrium Conditions

For a cross-section subjected to an applied axial force *N* and bending moment *M* about the horizontal axis, with the section discretized into *n* layers along the depth direction (z-axis), the internal axial force and bending moment are computed by integration of the stress resultants over the layer set:

$$N_{int} = \sum_{i=1}^{n} \left(\sum_{j=1}^{m} \sigma_{ij} d_i b_{ij} \right) \tag{3.1}$$

$$M = \sum_{i=1}^{n} \left(\sum_{j=1}^{m} \sigma_{ij} d_i b_{ij} z_i d_i \right) \tag{3.2}$$

where n is the total number of layers along the depth z, m is the number of material components in layer i (for composite layers containing concrete, steel and FRP simultaneously), σ_{ij} is the stress in the j^{th} material component of layer i, b_{ij} is the width of that component, d_i is the layer thickness, and z_i is the distance from the centroid of layer i to

the reference axis. Compressive stresses and strains are taken as negative, tensile as positive, in accordance with the sign convention of EN 1992-1-1.

3.3. Constitutive Models for Structural Materials

This section presents the non-linear constitutive laws adopted for each material and strengthening configurations considered in this dissertation, including plain concrete, steel reinforcement, GFRP reinforcement, SFRC, SHCC, and FRP-confined reinforced concrete. The constitutive properties are formulated considering the design values obtained by applying partial safety factors $\gamma_c = 1.5$ and $\gamma_s = 1.15$ for concrete and steel respectively. These laws are implemented directly within the layered sectional analysis framework in DOCROS, where the moment-curvature response relating to the behaviour of the cross-section under combined axial-bending loading conditions are obtained, forming the basis for the axial and flexural capacity predictions through the N-M interaction diagrams presented in chapter 5.

3.3.1. Plain Concrete

The mechanical response of plain concrete under compression has been well documented, and is characterized by a non-linear ascending branch leading to a well-defined peak stress, followed by progressive softening as micro-cracks coalesce and the compression zone degrades [39], as shown in **Figure 3.2 a)**.

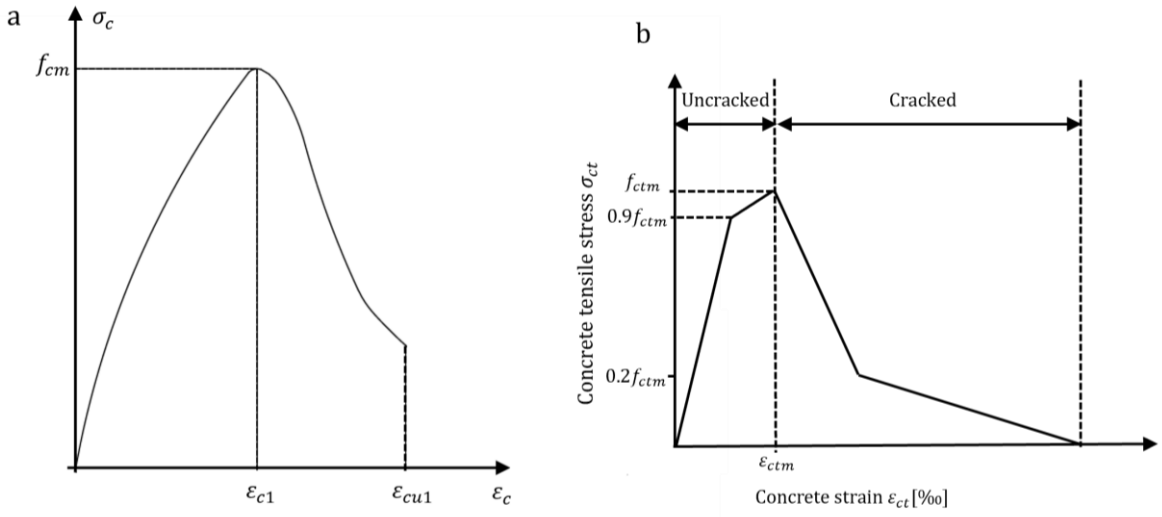


Figure 3.2: a) Schematic representation of concrete in compression [39] b) Simplified design stress-strain relationship of concrete in tension [40]

As shown in **Figure 3.2: a)**, the compressive behaviour of plain concrete is modelled using the Sargin stress-strain relationship for short term uniaxial loading defined by the expression:

$$\frac{\sigma_c}{f_{cm}} = \frac{k\eta - \eta^2}{1 + (k-2)n} \text{ for } 0 < |\varepsilon_c| \leq |\varepsilon_{c1}| \tag{3.3}$$

$$\sigma_c = f_{cd} \text{ for } \varepsilon_{c1} \leq \varepsilon_c \leq \varepsilon_{cu1} \tag{3.4}$$

where $f_{cm} = f_{ck} + 8$ (f_{cm} in MPa) is the mean compressive strength, ε_{c1} is the strain at peak stress, ε_{cu1} is the nominal ultimate compressive strain, $n = {\varepsilon_c}/{\varepsilon_{c1}}$ and $k = 1.05E_{cm} \times |\varepsilon_{c1}|/ f_{cm}$. The initial tangent elastic modulus is taken as the mean secant modulus such that:

$$E_{cm} = 22\left[\left(\frac{f_{cm}}{10}\right)^{0.3}\right] \ (f_{cm} \text{ in MPa}) \tag{3.5}$$

This modulus is used as the elastic stiffness in the initial ascending branch, and governs the tension envelope of the concrete.

In tension, however, plain concrete is inherently brittle. Its tensile capacity is much lower than its compressive strength, and its response is governed by two distinct regimes, the uncracked ad cracked regimes respectively (see **Figure 3.2 b**). In the uncracked regime, the response is essentially linear elastic up to about 90% of the tensile strength, followed by a short, non-linear rise associated with the onset of distributed micro-cracking, up to the full tensile strength (f_{ctm}) at the cracking strain $\varepsilon_{ctm} = \frac{f_{ctm}}{E_{cm}}$. The mean tensile strength is determined as:

$$f_{ctm} = 0.3f_{ck}^{(2/3)} \text{ for } f_{ck} \leq 50 \text{ MPa} \tag{3.6}$$

$$f_{ctm} = 2.12In\left(1 + \frac{f_{cm}}{10}\right) \text{ for } f_{ck} > 50 \text{ MPa} \tag{3.7}$$

Beyond this point, the section cracks and enters into a softening regime, reflecting the loss of load transfer across the newly formed crack face, before declining much more gradually over a substantially larger strain range as a small residual capacity, sustained by aggregate interlock and crack-bridging, is progressively exhausted. In marine environments relevant to the context of this study, the tensile cracks provide diffusion pathways for chloride ions to reach the embedded prestressing cables, initiating the corrosion-driven deterioration cycle observed in the extracted Earl C. Davis Bridge specimens. The constitutive model for concrete

in compression and tension adopted in DOCROS for plain unconfined concrete is shown in the **Figure 3.3**:

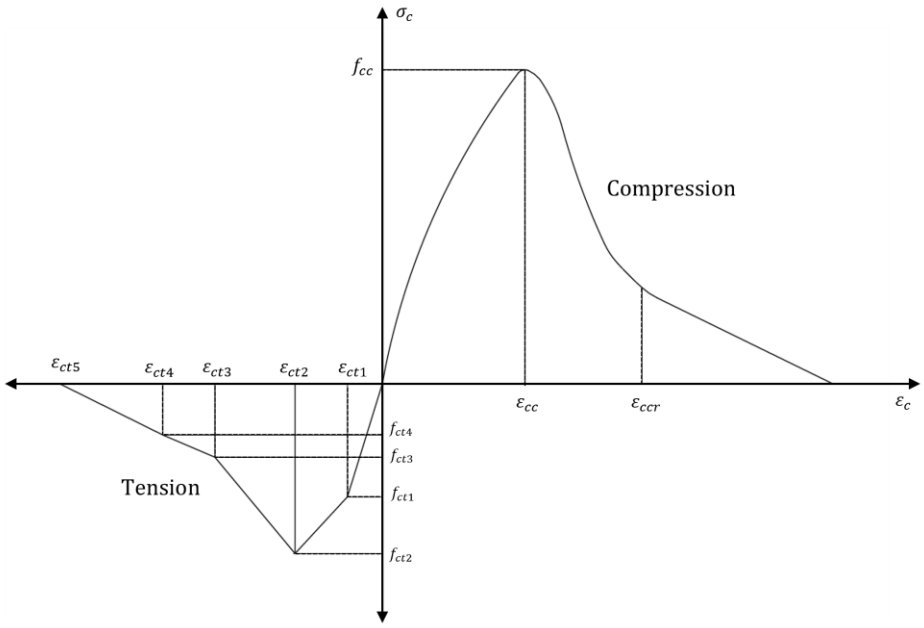


Figure 3.3: Constitutive model adopted for plain concrete in compression and tension

The model parameters for the plain concrete grades used in this study are summarized in **Table 3.1**, where the residual post-crack stresses are set to small but non-zero values (typically 1×10^{-3} MPa to 1×10^{-4} MPa) to maintain numerical stability in the constitutive law algorithm.

Table 3.1: Constitutive model parameters for plain concrete grades C35 and C60

Parameter	C35	C60
f_{ck} (MPa)	35	60
f_{cm} (MPa)	43	68
f_{cc} (MPa)	-23	-40
E_{cm} (GPa)	34	39
ε_{cc}	-2.250×10^{-3}	-2.600×10^{-3}
ε_{ccr}	-3.500×10^{-3}	-2.900×10^{-3}
n	2.000	1.589
f_{ct1} (MPa)	1.610	2.200
f_{ct2} (MPa)	3.210	4.400
f_{ct3} (MPa)	1.000×10^{-3}	1.000×10^{-3}
f_{ct4} (MPa)	100.000×10^{-6}	100.000×10^{-6}

Parameter	C35	C60
ε_{ct1}	47.098×10^{-6}	55.687×10^{-6}
ε_{ct2}	9.419×10^{-5}	111.375×10^{-6}
ε_{ct3}	1.000×10^{-3}	1.000×10^{-3}
ε_{ct4}	5.000×10^{-3}	5.000×10^{-3}
ε_{ct5}	10.000×10^{-3}	10.000×10^{-3}

3.3.2. Steel Fibre Reinforced Concrete (SFRC)

The fundamental limitation of plain concrete in structural applications is the inability to transfer stress across cracked sections. Once the concrete matrix fractures, the cracks propagate and open freely, and the load-carrying capacity in the cracked zone is lost. The incorporation of short, randomly dispersed steel fibres into the cementitious matrix introduces a crack-bridging mechanism where the fibres crossing a fracture plane engage in pullout resistance, sustaining a post-crack tensile stress that decays gradually rather than collapsing abruptly [41]. As a result, SFRC is able to absorb a significantly higher amount of energy per unit volume than plain concrete, with improved resistance to crack propagation under both static and cyclic loading. The degree of post-crack residual strength depends on the fibre geometry, volume fraction, and matrix bond characteristics, and is formally characterized in EN 1992-1-1:2023 Annex L [42], through characteristic residual flexural tensile strengths at defined crack mouth opening displacements (CMOD) measured in standard notched beam tests per EN 14651 [43]. Notably, the residual flexural tensile strengths $f_{R,1k}$ was measured at CMOD = 0.5 mm and $f_{R,3k}$ at CMOD = 2.5 mm. The performance class designation takes the form SC-DC, where SC is the strength class (minimum $f_{R,1k}$ in MPa) and DC is the ductility class (characterized by letters a through e, indicating the ratio $f_{R,3k}/\mathrm{SC}$).

The compressive constitutive law for SFRC is a modification of the plain concrete model, in which the strain at peak compressive stress is elevated by the fibre contribution to post-cracking compression ductility [42]:

$$\varepsilon_{c1,SFRC(‰)} = 0.7 f_{cm}^{(2/3)}\left(1 + 0.03 f_{R,1k}\right), f_{R,1k} \text{ in MPa} \tag{3.8}$$

The ultimate compressive strain is fixed at $\varepsilon_{cu} = 6.0 \times 10^{-3}$ for all SFRC classes regardless of strength class [42], reflecting the improved post-peak compression ductility provided by the fibres.

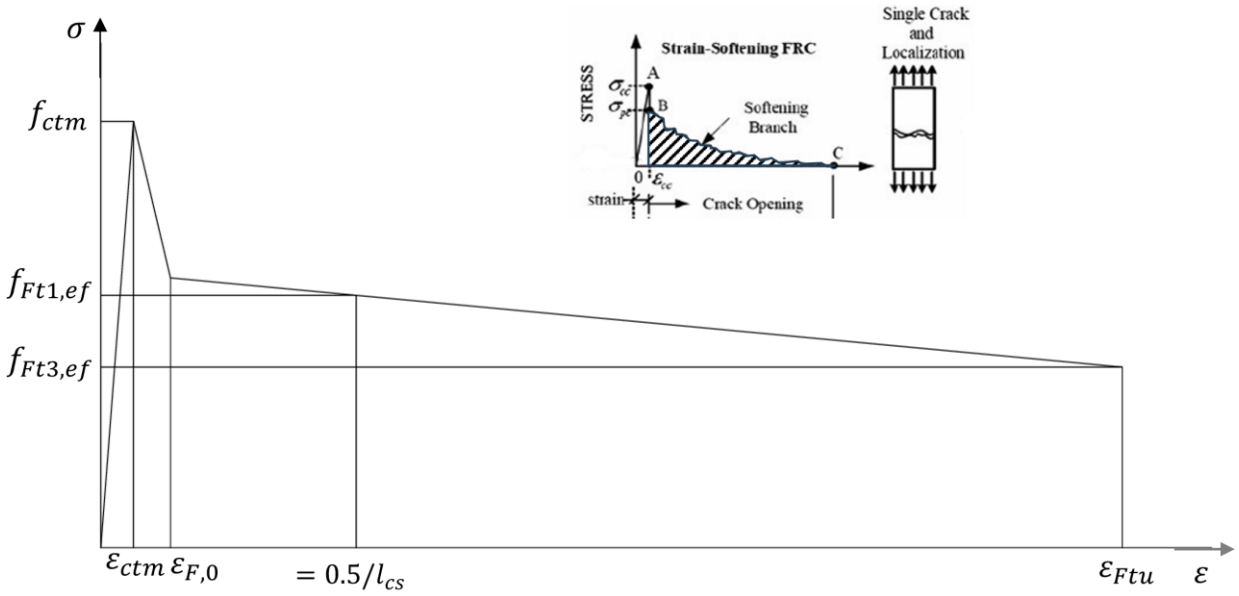


Figure 3.4: Constitutive law for SFRC in tension [4], [42]

The tensile constitutive law for SFRC follows the constitutive model relating to **Figure 3.4**: which consists of a linear elastic rising branch up to the matrix cracking stress f_{ctm}, followed by a bilinear post-crack descending or ascending branch defined by two residual effective stresses:

$$f_{Ft1,ef} = k_0 . k_G . 0.37 f_{R,1k} \quad (3.9)$$

$$f_{Ft3,ef} = k_0 . k_G . (0.57 f_{R,3k} - 0.26 f_{R,1k}) \quad (3.10)$$

where $k_0 = 1$ for bending with axial force (EN 1992-1-1:2023, cl. L.5.5.1(4)) and $k_G = 1.0 + A_{ct} . 0.5 \leq 1.5$. The strain corresponding to $f_{Ft1,ef}$ is $\varepsilon_{F,0} = 0.5/l_{cs}$ and the ultimate strain is $\varepsilon_{Ftu} = 2.5/l_{cs}$, where $l_{cs} = 125$ mm is the simplified characteristic length. The terminating point ε_{ct5} is set to 22×10^{-3} (slightly beyond ε_{Ftu}) with zero stress, ensuring a non-zero terminal slope to maintain numerical stability.

If $f_{Ft3,ef} > f_{Ft1,ef}$, the SFRC exhibits a post-crack rising branch (near strain-hardening behavior, ductility class d and e). If $f_{Ft3,ef} < f_{Ft1,ef}$, the behavior is strain-softening (ductility class a through c). **Table 3.2** summarizes the characteristic and design residual tensile and strain properties of different SFRC performance classes considered in this study.

Table 3.2: Residual tensile and strain properties of SFRC for different performance classes

Class	$f_{R,1k}$ (MPa)	$f_{R,3k}$ (MPa)	$f_{Ft1,ef}$ (MPa)	$f_{Ft3,ef}$ (MPa)	$\varepsilon_{c1,SFRC}$(‰)
3a / C60	3.0	1.5	1.136	0.076	3.114×10^{-3}
3c / C60	3.0	2.7	1.136	0.777	3.114×10^{-3}
3e / C60	3.0	3.9	1.136	1.477	3.114×10^{-3}
6a / C60	6.0	3.0	2.273	0.153	3.370×10^{-3}
8a / C60	8.0	4.0	3.031	0.204	3.540×10^{-3}
8e / C60	8.0	10.4	3.031	3.940	3.540×10^{-3}

3.3.3. Strain-Hardening Cementitious Composites (SHCC)

Strain-hardening cementitious composites (SHCC) represent a class of ultra-ductile cementitious materials characterized by a sustained post-cracking tensile hardening response attributed to intensive fibre bridging across multiple tight cracks. Unlike SFRC, which typically exhibits either softening or near-hardening post-crack tension, SHCC develops a true hardening branch with residual stresses exceeding the first cracking stress over extended strain ranges [44].

Strain-softening fibre reinforced Concrete (SSFRC), despite improving post-crack energy absorption behaviour of the concrete matrix, still exhibits localized fracture such that deformation is concentrated at a single dominant crack while the rest of the matrix remains essentially undeformed. SHCC overcomes this limitation by developing multiple parallel micro-cracks, while the tensile stresses continue to rise with the extended tensile strains [44], as shown in **Figure 3.5**.

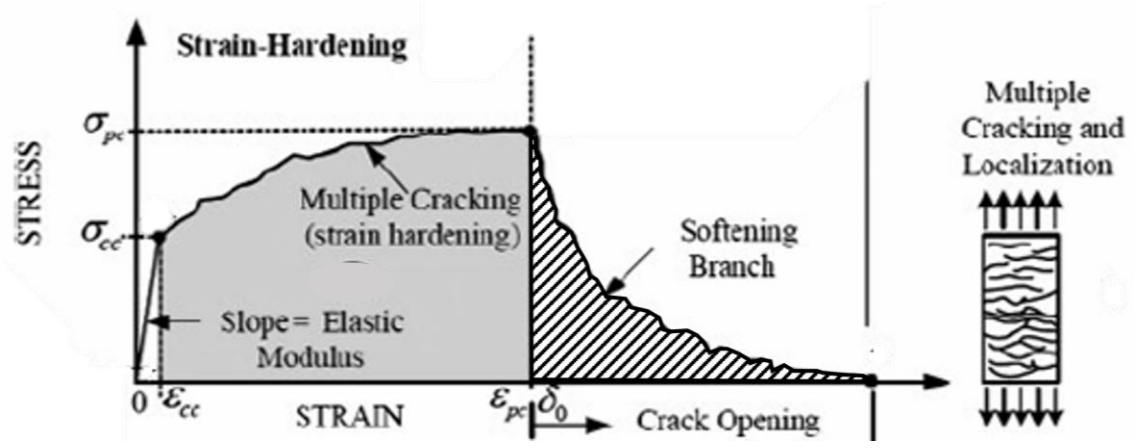


Figure 3.5: Characteristic stress-strain and cracking behavior of SHCC [4]

This multiple-cracking behaviour is due to the enhancement of the matrix fracture toughness and fibre-matrix bond characteristics, such that the energy available for crack propagation is always exceeded by the fibre bridging resistance at each crack plane, preventing localization until the bridging capacity is exhausted [45]. In the context of marine pile repair which is relevant to this work, the small crack widths produced by this regime are particularly significant, such that cracks below approximately 50 micrometres (μm) are known to undergo autogenous self-sealing through continued cement hydration [46], effectively blocking the chloride diffusion pathways that drive ongoing corrosion of the reinforcement steel.

The compressive behaviour of SHCC adopted in this work follows the constitutive model for plain concrete in **Figure 3.3**, with modifications to the peak strain and ultimate strain to reflect the absence of coarse aggregate and the influence of the fibre bridging on compression failure. The compression peak strain ε_{cc} and the ultimate strain ε_{ccr} are elevated above the plain concrete values, reflecting the post-peak ductility provided by fibre bridging of cracks. **study.**

Table 3.3 summarizes the constitutive model properties for SHCC adopted in this study.

Table 3.3: Constitutive model properties for SHCC

Parameter	C35
f_{cc} (MPa)	-35
E_c (GPa)	18.420
ε_{cc}	-2.000×10^{-3}
ε_{ccr}	-8.000×10^{-3}
n	2.000
f_{ct1} (MPa)	2.500
f_{ct2} (MPa)	3.750
f_{ct3} (MPa)	275.000×10^{-3}
f_{ct4} (MPa)	137.500×10^{-3}
ε_{ct1}	135.722×10^{-6}
ε_{ct2}	15.400×10^{-3}
ε_{ct3}	77.000×10^{-3}
ε_{ct4}	107.800×10^{-3}
ε_{ct5}	138.680×10^{-3}

3.3.4. Steel Reinforcement

The longitudinal reinforcement of the assessed piles extracted during the replacement of the Earl C. Davis Bridge consists of stress-relieved (normal relaxation) prestressing strands, characterized by a relatively high tensile strength, compared to conventional mild steel. The stress-relieved prestressing steel was modelled in DOCROS as normal mild steel without any prestress in them, using the constitutive model shown in **Figure 3.6**, where the stress-strain behaviour of prestressing strands is characterized by a continuously curved stress-strain response without a distinct yield plateau, exhibiting a gradual transition from elastic to inelastic behaviour, instead of a sharp precisely defined yield point.

The structural assessment in this study was conducted under monotonic loading with the constitutive model shown in **Figure 3.6**, which represents a bilinear model comprising two successive linear branches separated at the yield stress. In the first branch, the material responds elastically in direct proportion to the applied strain. At the yield strain, the curve transitions to the second branch, in which the stress continues to rise linearly but at a reduced rate governed by the post-yield hardening modulus E_{sh}.

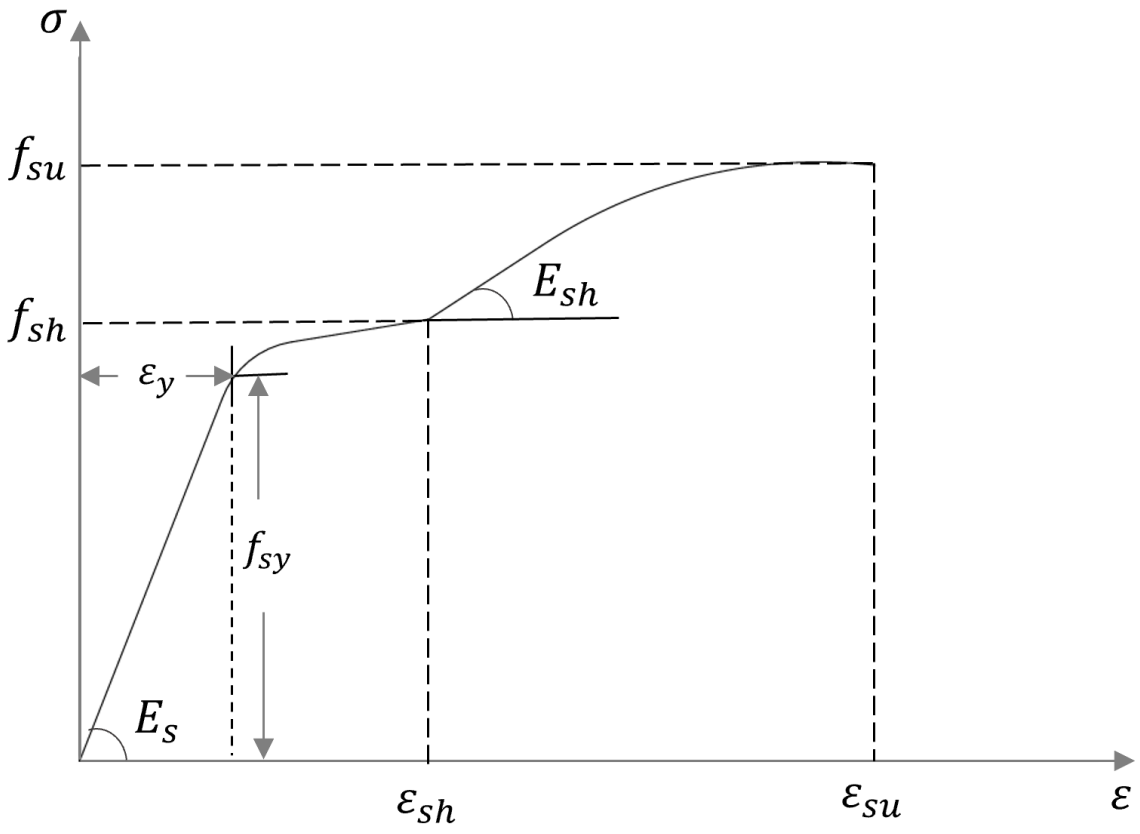


Figure 3.6: Constitutive model for steel

The material properties of the strand are specified in accordance with ASTM A416/A416M-12a [47], the standard specification for stress-relieved strand for prestressed concrete. For Grade 270 stress-relieved strand of 1860 MPa, ASTM A416/A416M-12a specifies that the yield stress shall not be less than 85% of this breaking strength (f_{pu}). The characteristic yield stress is therefore obtained as:

$$f_{sy} = 0.85 \times f_{pu} \tag{3.11}$$

The minimum elongation at rupture is specified by ASTM A416/A416M-12a as 3.5% in a 24-inch (610-mm) gauge length, establishing the characteristic ultimate strain as $\varepsilon_{uk} = 35\times10^{-3}$. The characteristic values were converted into corresponding design values for use in the constitutive model considering design conditions at ultimate limit state as:

$$f_{pud} = \frac{f_{pu}}{\gamma_s} \tag{3.12}$$

$$f_{syd} = \frac{f_{sy}}{\gamma_s} \tag{3.13}$$

$$\varepsilon_{syd} = \frac{f_{syd}}{E_s} \tag{3.14}$$

$$\varepsilon_{ud} = 0.9\varepsilon_{uk} \tag{3.15}$$

where f_{pud} is the design value for the ultimate breaking strength of the prestressing steel, f_{syd} is the design value of the yield stress, γ_s=1.15 is the partial safety factor, ε_{sy} is the yield strain. The material properties of the steel strands are presented in **Table 3.4**.

Table 3.4: Constitutive model properties for the longitudinal reinforcing steel

Parameter	Value
E_s (GPa)	200
f_{su} (MPa)	1617
f_{sh} (MPa)	1375
ε_{su}	31.500× 10^{-3}
ε_{sh}	8.000 × 10^{-3}
E_{sh} (GPa)	10.314

Notes: Where $\varepsilon_{sh} = \varepsilon_{sy}+0.15\varepsilon_{sy}$, $f_{sh} = f_{sy}$

The transverse reinforcement is not modelled in DOCROS given its insignificance to axial loading stress distribution.

3.3.5. Fibre Reinforced Polymers (FRP)

FRP composites consist of high strength fibres embedded in a resin matrix. Fibers are known to carry the mechanical loads in the fibre direction, while the matrix transfers the stresses between fibres and provide protection from external environmental conditions. Two FRP systems were carefully selected and adopted in this study, where glass fibre-reinforced polymer (GFRP) bars were used as internal reinforcement within the cover repair zone, and carbon fibre-reinforced polymer (CFRP) sheets as an external confinement jacket wrapped around the pile perimeter.

The predominant mechanical property of all FRP composites is that they are linear elastic up to failure. Unlike steel, which undergoes progressive plastic deformation beyond its yield point, FRP fibres fracture suddenly when the ultimate tensile strain is reached, with no prior warning through inelastic strain accumulation. They maintain a constant elastic modulus up to sudden brittle rupture at the characteristic tensile strength. The effective design rupture strain for GFRP reinforcement is determined by applying an environmental reduction factor $CE = 0.70$ to the characteristic fibre strain, in accordance to the specifications in Table 6.2 of the ACI 440. 1R-15[48]. The material properties for GFRP and CFRP used in this study are summarized below:

Table 3.5: Summary of FRP Material Properties

Property	GFRP bars	CFRP Fabric
Design ultimate tensile strength, f_{fu} (MPa)	1000	3800
Tensile modulus, E_f (GPa)	50	242
Characteristic rupture strain	0.020	0.016
Diameter/thickness (mm)	Φ10	t_f = 0.171

3.4. Constitutive Model for FRP Confined Reinforced Concrete

As discussed in the state-of-the-art review, wrapping a concrete column with an FRP jacket in the hoop direction generates a passive lateral confining pressure that elevates both compressive strength and ultimate strain, the effectiveness of which depends critically on the confinement stiffness, the concrete dilation characteristics, and the presence or absence of

internal steel reinforcement. In the repaired pile cross-sections examined in this study, two structurally distinct concrete zones co-exist: the cover, confined by the FRP jacket alone, and the core, enclosed simultaneously by the FRP jacket and the internal steel spiral. These two zones require separate constitutive treatment, as the combined FRP-steel confinement in the core produces a qualitatively different stress-strain response from the FRP-only case [36], [49]. The model adopted in this study to address this dual confinement mechanism is described in the following sections.

3.4.1. Design-Oriented Model (DOM) for FRP Confined Reinforced Concrete

The DOM of Shayanfar et al. [36], adopted for all FRP-confined repair configurations in this study was developed specifically for circular FRP-confined reinforced concrete (FCRC) columns, calibrated from a database of 97 axial compression tests spanning a wide range of concrete strengths, FRP stiffnesses, and spiral configurations. Experimental evidence demonstrates that the presence of longitudinal reinforcement and transverse spiral reinforcement in an RC column fundamentally alters the post-peak dilation behaviour and the confinement interaction between the two confinement sources. The principal merit of the DOM over existing FRP confinement models is the explicit and independent treatment of the cover and core concrete zones within the same cross-section, each governed by separate constitutive parameters whilst sharing a common strain field.

3.4.1.1. Prediction of the stress-strain relationship

The pile sections are partitioned into two concentric zones as the cover zone and the core zone, respectively, and the DOM prescribes a two-branch stress-strain relationship for each zone as a parabolic ascending first branch from the origin to the transition point, followed by a second linear ascending branch with hardening behaviour extending to the ultimate strain, as shown in **Figure 3.7**.

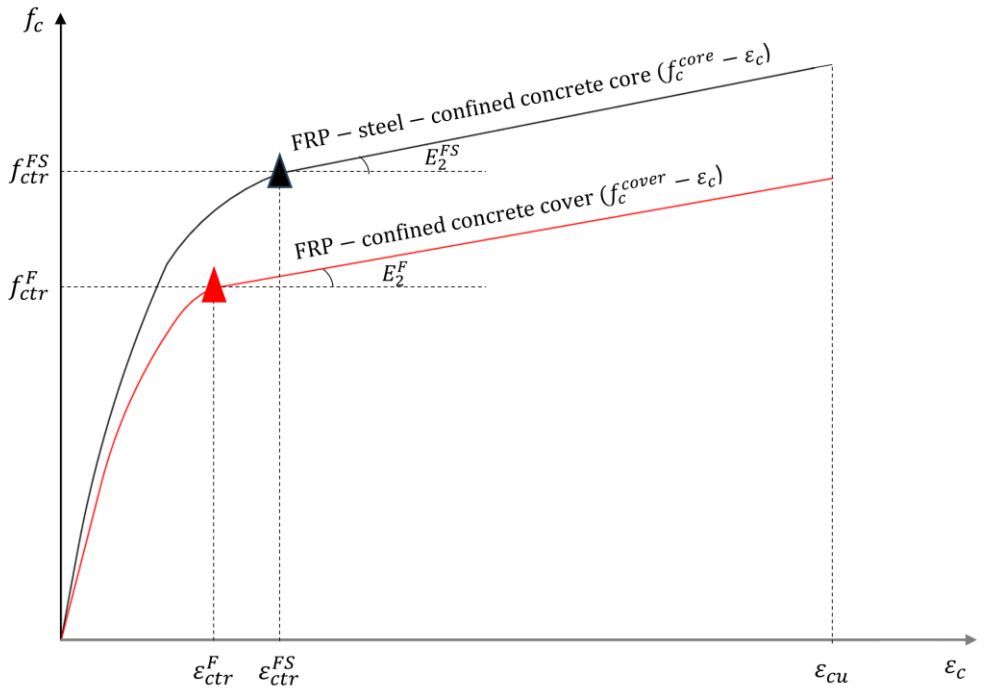


Figure 3.7: Stress-strain relationship of FCRC [36]

On the basis of the stress-strain behaviour of the FRP confined concrete (FCC), the following formulations for the stress-strain behaviour of FCRC for the core and cover contributions, respectively. The general form of the core zone is:

$$f_c^{core} = \left[A_1^{FS}\left(\frac{\varepsilon_c}{\varepsilon_{ctr}^{FS}}\right)^{nd} + A_2^{FS}\left(\frac{\varepsilon_c}{\varepsilon_{ctr}^{FS}}\right)\right] f_{ctr}^{FS} \quad \text{for } \varepsilon_c \leq \varepsilon_{ctr}^{FS} \tag{3.16}$$

$$f_c^{core} = f_{ctr}^{FS} + E_2^{FS}(\varepsilon_c - \varepsilon_{ctr}^{FS}) \quad \text{for } \varepsilon_c \geq \varepsilon_{ctr}^{FS} \tag{3.17}$$

where the superscript "FS" represents the FRP-steel confinement on the concrete core, A_1^{FS} and A_2^{FS} are polynomial coefficients determined at the transition point using the expressions below.

$$A_1^{FS} = \frac{1 - E_2^{FS}/E_{ctr}^{FS}}{1 - n_d} \tag{3.18}$$

$$A_2^{FS} = \frac{E_2^{FS}}{E_{ctr}^{FS}} - \frac{n_d}{1 - n_d}\left(1 - \frac{E_2^{FS}}{E_{ctr}^{FS}}\right) \tag{3.19}$$

where $E_{ctr}^{FS} = \frac{f_{ctr}^{FS}}{\varepsilon_{ctr}^{FS}}$ is the secant modulus to the transition point. The shape exponent $(n_d > 1)$ governs the curvature of the first branch and is expressed as $(n_d = n_{d0}.\psi_f.\psi_s)$, the product

of an unconfined concrete base term, an FRP modifier, and a spiral modifier, calibrated from the regression analysis and equations 39-41 in Shayanfar et al. [32].

The cover zone follows an identical formulation structure, but with the superscript "F" replacing "FS" to represent FRP confined concrete as:

$$f_c^{cover} = \left[A_1^F \left(\frac{\varepsilon_c}{\varepsilon_{ctr}^F}\right)^{nd} + A_2^F \left(\frac{\varepsilon_c}{\varepsilon_{ctr}^F}\right)\right] f_{ctr}^F \quad \text{for } \varepsilon_c \leq \varepsilon_{ctr}^F \tag{3.20}$$

$$f_c^{cover} = f_{ctr}^F + E_2^F(\varepsilon_c - \varepsilon_{ctr}^F) \quad \text{for } \varepsilon_c \geq \varepsilon_{ctr}^F \tag{3.21}$$

where the polynomial coefficients A_1^F and A_2^F are determined at the transition point as:

$$A_1^F = \frac{1 - E_2^F/E_{ctr}^F}{1 - n_d} \tag{3.22}$$

$$A_2^F = \frac{E_2^F}{E_{ctr}^F} - \frac{n_d}{1 - n_d}\left(1 - \frac{E_2^F}{E_{ctr}^F}\right) \tag{3.23}$$

$$E_{ctr}^F = \frac{f_{ctr}^F}{\varepsilon_{ctr}^F} \tag{3.24}$$

3.4.1.2. Transition zone coordinates

The stress (f_{ctr}^F) and strain (ε_{ctr}^F) coordinates for the cover transition zone are computed from the FRP lateral stiffness (K_{LF}) and the size corrected unconfined concrete strength (f_{c0}) using the formulations developed for FCC as:

$$\frac{f_{ctr}^F}{f_{c0}} = 1 + 0.043\left(\frac{K_{Lf}}{f_{c0}}\right)^{0.4} \tag{3.23}$$

$$\frac{\varepsilon_{ctr}^F}{\varepsilon_{c0}} = 0.045\psi_K f_{c0}^{0.25} + 0.0075K_{LF}^{0.37} \tag{3.24}$$

where $\psi_K = 0.7K_{LF}^{0.07} \leq 1$, and the lateral stiffness $K_{Lf} = 2\frac{n_f t_f E_f}{D}$; n_f is the number of layers of FRP wrap, t_f is the thickness of the CFRP fabric, E_f is the modulus of elasticity of the FRP. To account for steel confined improvements on the concrete core, the corresponding transition zone coordinates f_{ctr}^{FS} and ε_{ctr}^{FS} are computed using the normalized strength enhancement of the steel confinement effectiveness index by Mander et al. [50], modulated by the terms η_f and η_s as shown below.

$$\frac{f_{ctr}^{FS}}{f_{ctr}^{F}} = 1 + \frac{\Delta_{f,s}}{1+\eta_f} \tag{3.25}$$

$$\frac{\varepsilon_{ctr}^{FS}}{\varepsilon_{ctr}^{F}} = 1 + 5\frac{\Delta_{f,s}}{1+\eta_f} \tag{3.26}$$

The modulation terms $\eta_f$and η_s are calibrated regression functions of the FRP and steel stiffness parameters, spiral/hoop configurations, concrete strength and column dimensions. Their full expressions are covered in Equations 20-28 of Shayanfar et al. [36].

3.4.1.3. Second branch slopes

The second branch slope of the cover concrete is determined from the calibrated FRP confinement stiffness as:

$$E_2^F = 3.38\gamma_{fc}E_f^{0.15}K_{Lf}^{0.47}f_{c0}^{0.31} \tag{3.27}$$

where $0.8 \leq \gamma_{fc} = \frac{f_{c0}}{25} \leq 1$. The second branch for the core is obtained by scaling E_2^F with a factor η_E capturing the contribution to the post transition hardening rate, as shown in Eq. (3.28) and Eq. (3.29):

$$E_2^{FS} = \eta_E E_2^F \tag{3.28}$$

$$\eta_E = 1.7\frac{K_{Ls}^{0.1}f_{c0}^{0.08}}{\lambda_E K_{Lf}^{0.1}f_{yh}^{0.1}(1.15 - 1.85\,c/D)} \tag{3.29}$$

where $\lambda_E = 1$ for spirals K_{Ls} is the lateral stiffness due to steel hoops, f_{yh} is the yield stress of the steel, and c/D is the cover to diameter ratio.

3.4.1.4. Ultimate strain

The DOM prescribes the shape of the ascending response of the FCRC, but does not determine the ultimate strain correlating to FRP rupture. The ultimate strain is determined from the Analysis Oriented Model of Shayanfar et al. [51], which considers two distinct failure mechanisms that may govern depending on the confinement configuration. The first corresponds to the rupture of the FRP jacket, which occurs when the maximum concrete hoop

strain along the column height reaches the FRP hoop rupture strain $\varepsilon_{h,rup}$. The corresponding ultimate axial strain is:

$$\frac{\varepsilon_{cu,r}}{\varepsilon_{c0}} = 17.7 f_{c0}^{-0.27} \rho_{K,f}^{0.61} \rho_{\varepsilon} \geq 1.5 \tag{3.30}$$

where $\rho_{K,f}$ is the effective FRP confinement stiffness index accounting for the non-uniform distribution of concrete lateral expansion along the column height (Equation 5 and 6 of Shayanfar et al. [51]), and $\rho_{\varepsilon} = \frac{\varepsilon_{fu}}{\varepsilon_{c0}}$ is the ratio of the FRP rupture strain to the strain of the unconfined concrete strain at peak. The second criterion corresponds to concrete crushing, which may govern in configurations where the FRP spacing reduces the effectiveness of lateral confinement between the strips, allowing localized concrete failure before the FRP jacket reaches its rupture strain. The ultimate axial strain associated with this mechanism is:

$$\frac{\varepsilon_{cu,c}^{FPC}}{\varepsilon_{c0}} = 1.5 + 4\left(\frac{\varepsilon_{cu,r}}{\varepsilon_{c0}}\right)\left(1 - R_f\right) \geq 1.5 \tag{3.31}$$

where $R_f = s_f/D$ is the normalized FRP strip spacing. For a full wrap FRP configuration, $s_{f=0}$, hence $R_f = 0$. The governing ultimate strain is then taken as a minimum value of the two criteria as:

$$\varepsilon_{cu} = min\left(\varepsilon_{cu,r}, \varepsilon_{cu,c}^{FPC}\right) \tag{3.32}$$

3.4.1.5. Equivalent Concrete Strength for Heterogenous sections

The DOM was developed and calibrated on homogenous specimens, in which the existing concrete core and the cover are made of the same cementitious matrix, requiring a single uniform value of f_{c0} as a primary input for the concrete compressive strength. However, in the repair configurations explored in this work, the original in-situ pile concrete is mostly considered as part of the existing concrete core, while the cover zone is replaced with different cementitious material with distinct compressive strengths and enhanced tensile properties, thereby creating a heterogenous concrete matrix. To accommodate this within the DOM's single input framework, an area weighted equivalent strength is adopted as:

$$f_{c,eq} = \frac{\left(f_{c0,core}.A_{c,core} + f_{c0,cover}A_{c,cover}\right)R}{A_{c,core} + A_{c,cover}} \tag{3.33}$$

where $f_{c0,core}$ is the compressive strength of the existing concrete core, $f_{c0,cover}$ is the compressive strength of the repair material in the cover zone; $A_{c,core}$ and $A_{c,cover}$ are the cross-sectional areas of the corresponding core and cover zones, respectively. R is a reduction factor taking into consideration different that the different materials with different elastic moduli of elasticity do not mobilize their full strengths simultaneously under the same axial strain, such that $R \leq 1$. In this work, $R = 1$ is adopted providing an upper-bound estimate of $f_{c,eq}$. Alternatively, in cases where the contribution of the concrete cover is considered negligible, $f_{c,eq} = f_{c,core} = f'_{c0}$ can be recommended for use in this model. The equivalent compressive strength ($f_{c,eq}$) can then be used as a substitute for the characteristic compressive strength (f'_{c0}) in determining the compressive strength of the unconfined concrete (f_{c0}) as shown in Eq. (3.34):

$$f_{c0} = 1.063\left(\frac{150}{D}\right)^{0.122}\left(\frac{D}{L}\right)^{0.088} f_{c,eq} \tag{3.34}$$

3.4.1.6. Predicted stress-strain response and constitutive model parameters

Following the approach presented above, and the detailed iterative approach in Shayanfar et al. [36], the corresponding stress-strain response for two fundamental strengthening configurations evaluated with two levels of corrosion damage on the existing steel reinforcement were predicted as follows: the homogenous case in which the compressive strength of the concrete core and cover were the same (f'_{c0}=$f_{c0,core}$=$f_{c0,cover}$ = 35MPa); and the heterogenous case where the concrete cover was replaced with a concrete grade of 60MPa, different from the existing core with 35MPa, as shown in **Figure 3.8** and **Figure 3.9**.

In both cases, the confinement model produces a characteristic two-branch ascending response, with a parabolic first branch rising to the respective transition zones where the dual FRP-steel confinement mechanism is mobilized, followed by a linearly ascending second branch extending to the ultimate confined strain governed by FRP hoop rupture. This response is fundamentally different from the softening post-peak of unconfined concrete and directly attributable to the passive lateral pressure continuously generated by the CFRP jacket as the concrete core dilates.

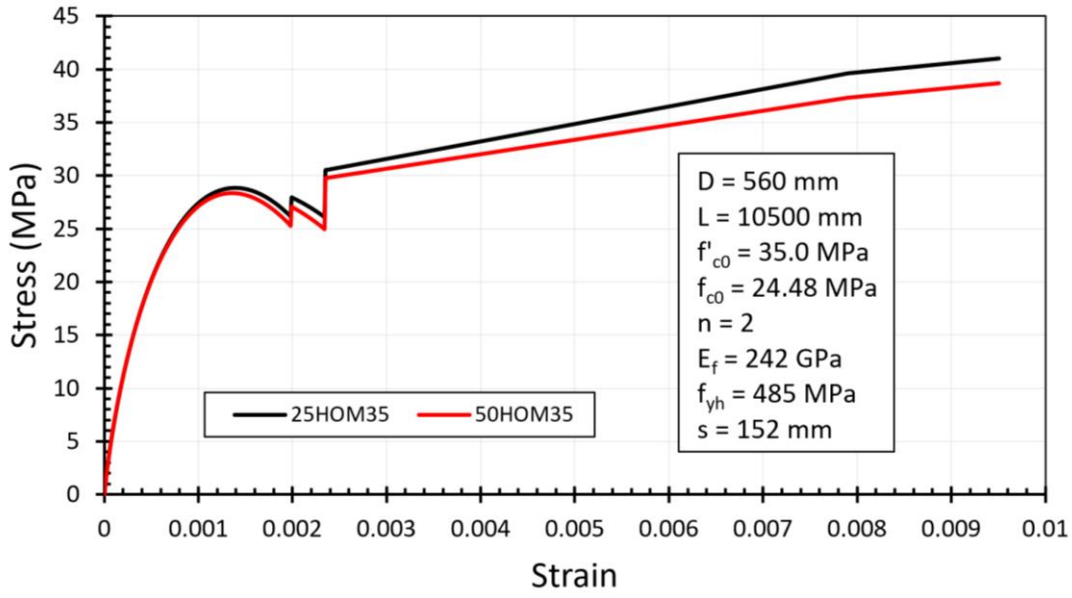


Figure 3.8: Predicted stress-strain behavior for FCRC pile with homogenous strengthening

Notably, the transition zones are characterized by kinking behavior, reflecting the onset of spiral steel yielding. This gives way to the reduced but sustained linear stiffness of the post-yield branch, where the steel confinement contribution has reached its plastic limit, and the FRP jacket progressively assumes the dominant role in arresting lateral dilation. At 25% corrosion level, the spiral retains greater transverse reinforcement area, contributing a higher steel confinement pressure and consequently producing elevated transition stress, a steeper second-branch slope, and a larger ultimate confined strength (f'_{cc}) relative to the 50% corrosion case, which experiences reduced spiral effectiveness (see **Figure 3.8** and **Figure 3.9**).

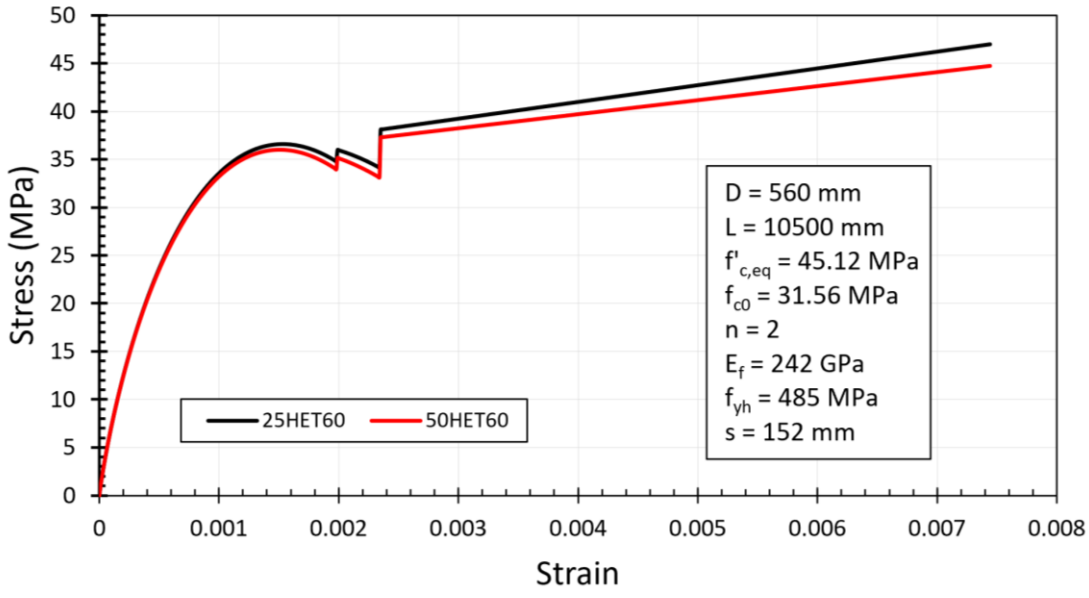


Figure 3.9: Predicted stress-strain behavior for FCRC pile with heterogenous strengthening

In the heterogeneous case, where the cover concrete was strengthened with C60 instead of C35, the approach adopted for obtaining the equivalent compressive strength ($f_{c,eq}$) of the strengthened cross-section, increased the effective unconfined concrete compressive strength (f'_{c0}), from 24.48MPa in the homogenous case to 31.56MPa. This increase in f'_{c0} is propagated through the confinement equations, resulting in higher predicted transition coordinates, a steeper second branch, and a greater peak confined stress (f'_{cc}) at both corrosion levels, confirming the additional structural benefit of the higher-strength cover material even within the unified FCRC constitutive framework.

The corresponding values of the predicted peak confinement stress and strain are obtained from the stress-strain results shown in **Figure 3.8** and **Figure 3.9**, and calibrated into the constitutive model shown in **Figure 3.10**, where the behaviour of the confined concrete in compression is modelled using the parabola-rectangle stress-strain relationship of EN 1992-1-1:2004.

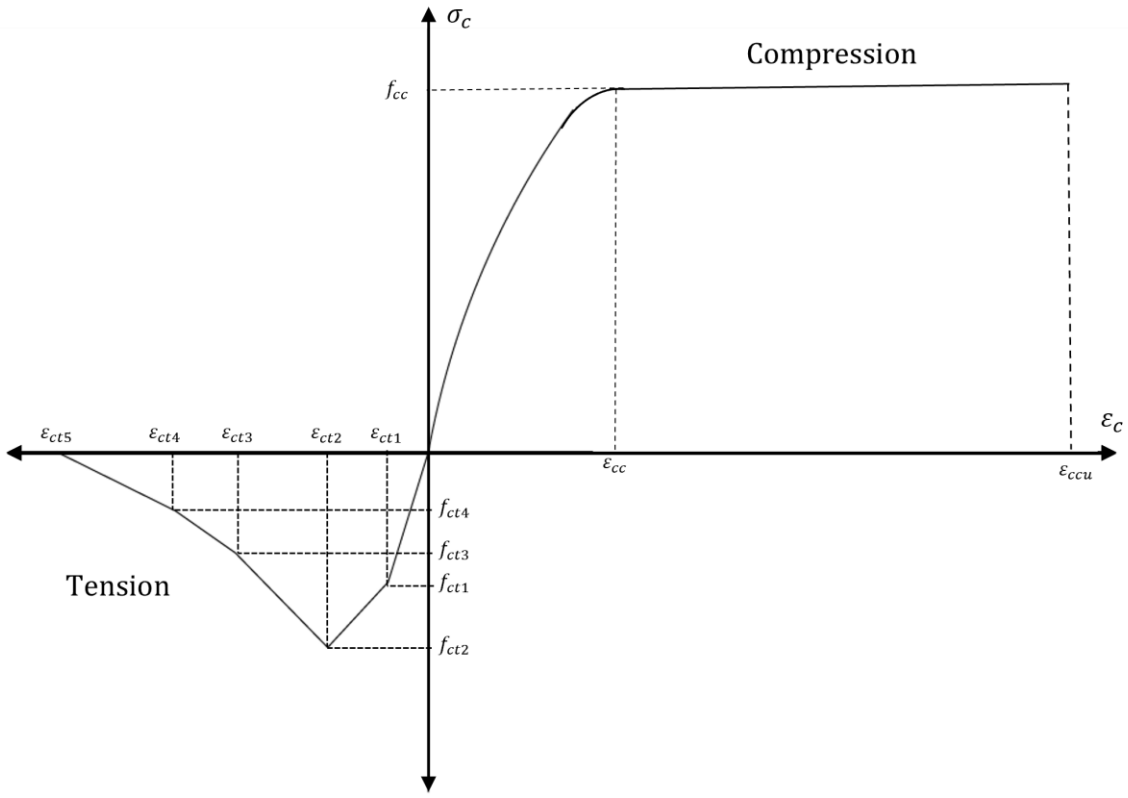


Figure 3.10: Schematic representation of the constitutive model adopted for confined concrete

The model parameters for the analysis of the homogenous and heterogenous strengthening configurations with FRP confinement are summarized in the **Table 3.6**, and the results are discussed in Chapter 5.

Table 3.6: Constitutive model properties for FCRC

Parameter	Homogenous strengthening (C35)		Heterogenous strengthening (C35+C60)	
	25% corrosion	50% corrosion	25% corrosion	50% corrosion
f_{cc} (MPa)	-41.022	-38.658	-46.988	-44.752
ε_{cc}	-2.000×10^{-3}	-2.000×10^{-3}	-2.000×10^{-3}	-2.000×10^{-3}
ε_{ccu}	-9.510×10^{-3}	-9.510×10^{-3}	-7.400×10^{-3}	-7.440×10^{-3}
n	2.000	2.000	2.000	2.000
f_{ct1} (MPa)	1.800	1.700	2.000	1.900
f_{ct2} (MPa)	3.600	3.400	3.900	3.800
f_{ct3} (MPa)	1.000×10^{-3}	1.000×10^{-3}	1.000×10^{-3}	1.000×10^{-3}
f_{ct4} (MPa)	100.000×10^{-6}	100.000×10^{-6}	100.000×10^{-6}	100.000×10^{-6}
ε_{ct1}	50.338×10^{-6}	49.107×10^{-6}	53.241×10^{-6}	52.184×10^{-6}
ε_{ct2}	100.676×10^{-6}	98.216×10^{-6}	106.482×10^{-6}	104.368×10^{-6}
ε_{ct3}	1.000×10^{-3}	1.000×10^{-3}	1.000×10^{-3}	1.000×10^{-3}
ε_{ct4}	5.000×10^{-3}	5.000×10^{-3}	5.000×10^{-3}	5.000×10^{-3}
ε_{ct5}	10.000×10^{-3}	10.000×10^{-3}	10.000×10^{-3}	10.000×10^{-3}

4. Analytical Framework For Determining the Shear Capacity of Strengthened RC Piles with Circular Cross-sections

4.1. Introduction

This chapter explores the shear behaviour of RC, and presents an analytical model adapted for circular cross-sections, to assess the shear capacity of the deteriorated prestressed steel concrete piles strengthened with different techniques, particularly different cementitious matrices reinforced with steel or GFRP bars and CFRP wraps. The original piles with an octagonal shape are treated as circular cross-sections, and then transformed to equivalent rectangular blocks whose behaviour is described by superposing the contribution of the existing core and the newly applied strengthening layer in the cover region realized in this work, using either steel or FRP reinforced concrete cover configurations comprising different cementitious matrix. The proposed model: (i) formalizes the approach to translate a circular geometry of a strengthened cross-section into an equivalent rectangular cross-section; (ii) presents a segment-based iteration approach for circular sections to determine the position of neutral axis, thereby establishing the boundary between the compression zone and tensile zone; and (iii) predicts the shear capacity of strengthened circular cross-sections considering the discrete contribution of the existing longitudinal steel and strengthening GFRP bars in the established tension zone, and evaluates the influence of corrosion and axial compression on the shear capacity of the strengthened RC piles.

4.2. Fundamental Governing Equations

Shear strength evaluation in concrete members has been addressed through various analytical approaches, with two prominent models dominating the field: the classical truss analogy [52], and the Modified Compression Field Theory developed as a more sophisticated equilibrium and compatibility method. While both approaches offer valuable insights into shear transfer mechanisms, the fundamental governing equations utilized in this work are based on the well-established truss model framework as adopted in Eurocode 2. The truss

analogy provides a rational basis for calculating the shear reinforcement contribution V_{Rds}, unlike the concrete contribution V_{Rdc} which remains controversial and relies on empirical methods. This chapter extends the traditional truss model approach, following the Eurocode 2 methodology, to develop analytical formulations specifically for strengthened circular concrete members with circular or spiral transverse reinforcement.

4.2.1. Formulations from the Truss Model

The shear strength of a RC beam V_{Rd} is often considered as a combination of the shear strength in concrete V_{Rdc} and the shear reinforcement V_{Rds}, as shown in Eq. (4.1).

$$V_{Rd} = V_{Rdc} + V_{Rds} \tag{4.1}$$

The relative contribution of each shear mechanism evolves with the cracking behaviour of the RC during loading. The concrete contribution V_{Rdc} is primarily considered in uncracked concrete in the compression zone, where the shear is predominantly carried by the concrete. Once cracking has occurred, shear transfer is redistributed among several coexisting mechanisms including the residual capacity of the compression zone above the top diagonal crack; aggregate interlock across the rough crack faces, estimated to carry up to half of the shear resisted by an uncracked member; the dowel action of the longitudinal reinforcement; and the tension carried by transverse reinforcement V_{Rds}. The methods to calculate V_{Rdc} and V_{Rds} in rectangular RC beams have been well explored in ACI 318-05 [53] and Eurocode 2 [54], based on the truss analogy that idealizes the cracked web as a parallel-chord truss as shown in **Figure 4.1**.

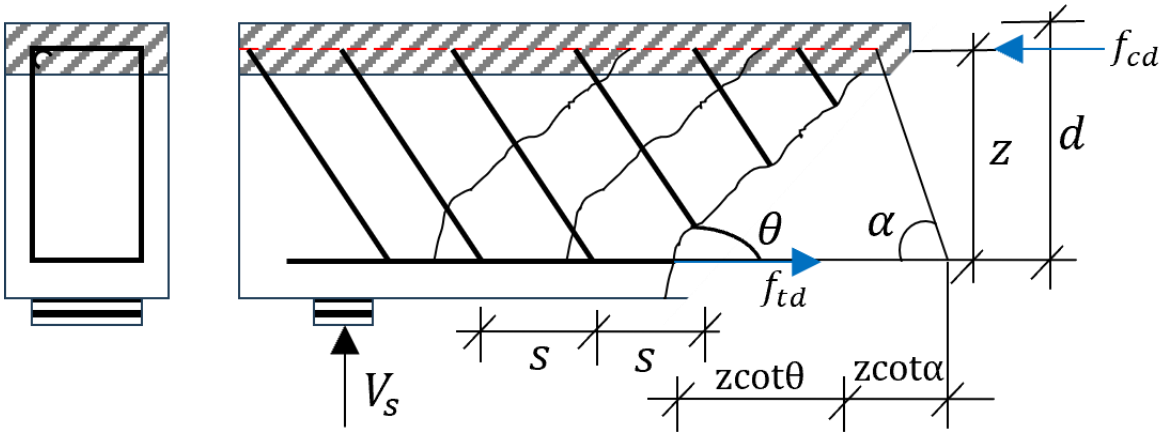


Figure 4.1: Shear Truss Analogy

Hence, the approach to determine V_{Rds} is widely adopted using Eq. (4.2).

$$V_{Rds} = \frac{A_{sw} \cdot f_{sydw}}{s} \cdot z \cdot (cot\theta + cot\alpha) \cdot sin\alpha \tag{4.2}$$

where θ is the inclination of the concrete strut, α is the angle between the shear reinforcement and the perpendicular axis, A_{sw} is the area of the transverse reinforcement, s is the spacing between the transverse shear reinforcement, f_{sydw} is the design value of the yield stress of the stirrups, and z is the internal lever arm taken as $0.9d$. The shear strength contribution of the concrete can be calculated as:

$$V_{Rdc} = \tau_{Rdc} \cdot b_w \cdot d \tag{4.3}$$

where τ_{Rdc} is the design shear resistance of the RC beam without shear reinforcement, b_w and d is the width and depth of the rectangular cross-section respectively. τ_{Rdc} is calculated using the following expression:

$$\tau_{Rdc} = \frac{0.66}{\gamma_v} \cdot \left(100 \cdot \rho_l \cdot f_{ck} \cdot \frac{d_{dg}}{d}\right)^{1/3} \geq \tau_{Rdc,min} \tag{4.4}$$

where γ_v is a partial safety factor for shear design according to Table 4.3 (NDP) in the EN 1992-1-1:2023, ρ_l is the reinforcement ratio for longitudinal steel calculated as $\rho_l = \frac{A_{sl}}{b_w.d} \leq 0.02$, f_{ck} is the characteristic compressive strength of the concrete, d_{dg} is the parameter for the roughness size of the aggregates, d is the effective depth of the section, and $\tau_{Rdc,min} = \frac{11}{\gamma_v} \cdot \sqrt{\frac{f_{ck}}{f_{yd}} \cdot \frac{d_{dg}}{d}}$ is the minimum shear stress resistance.

4.2.2. Influence of Axial Loading

In the design of deep foundations such as bridge piles, structural members are primarily designed as vertical compression elements to safely transfer heavy dead and traffic live loads into the ground. The influence of axial compression is primarily explored in this study. As axial compression increases, the concrete compression zone expands and the internal strain field shifts toward a predominantly compressive state, reducing tensile demand in the longitudinal reinforcement and suppressing diagonal cracking. This modification of the internal stress field flattens the diagonal compression field angle, increases the effective width of the compression

strut, and reduces the principal tensile strains that govern crack opening and propagation. The combined effect is a more stable and efficient shear-transfer mechanism, in which the diagonal strut carries shear at lower stress levels and is less susceptible to crushing. While axial compression introduces substantial gains in shear capacity as axial load increases beyond moderate load levels, the influence of axial tension due to lateral and seismic loads on the other hand increases the inclined crack width, which decreases the shear stresses transmitted by the concrete strut, leading to reduced shear capacity of the member.

To assess the shear capacity of the pile sections under axial compression, the mathematical modifications on shear resistance of concrete and SFRC are adopted based on the EN 1992-1-1:2023 framework as discussed below.

4.2.2.1. Shear Resistance Modification in Plain Reinforced Concrete

The presence of an axial compressive stress (σ_{cp}) fundamentally alters the concrete matrix's internal cracking behavior and aggregate interlocking mechanism, directly modifying the ultimate shear resistance of the plain RC (τ_{Rdc}), and is calculated as:

$$\tau_{Rdc,min} \leq \tau_{Rdc} = \tau_{Rdc,0} - k_1\sigma_{cp} \leq \tau_{Rdc,max} \tag{4.5}$$

where $\tau_{Rdc,0}$ is the design value of shear resistance calculated using Eq. (4.4), the value for $\tau_{Rdc,max}$ is determined as in Eq. (4.9), σ_{cp} is the design axial stress calculated as:

$$\sigma_{cp} = \frac{N_{Ed}}{A_c} \tag{4.6}$$

where N_{Ed} is the design axial compressive load (considered with a negative sign in compression) and A_c is the area of the cross-section. The factor k_1 in Eq. (4.5) is calculated as:

$$k_1 = \frac{0.5}{\alpha_{cs,0}}\left(e_p + \frac{d}{3}\right) \cdot \frac{A_c}{b_w.z} \leq 0.18 \cdot \frac{A_c}{b_w \cdot z} \tag{4.7}$$

where e_p is the eccentricity of the external load that produces the axial force, $\alpha_{cs,0}$ is the effective shear span expressed as the ratio of the design value of the bending moment to the shear capacity as:

$$\alpha_{cs,0} = \frac{M_{Ed}}{V_{Ed}} \geq d \tag{4.8}$$

$$\tau_{Rdc,max} = 2.15 \cdot \tau_{Rdc0} \left(\frac{\alpha_{cs,0}}{d}\right)^{1/6} \leq 2.7 \cdot \tau_{Rdc0} \quad (4.9)$$

4.2.2.2. Shear Resistance for SFRC in members without Transverse Shear Reinforcement

The post-cracking residual tensile strength provided by the fibre matrix is integrated into the shear resistance model of SFRC. Where the steel fibres are used as the sole mechanism to carry shear forces without stirrups or hoops, the total design shear resistance ($\tau_{Rd,cF}$) is formulated as:

$$\tau_{Rd,cF} = \eta_{cF}.\tau_{Rdc} + \eta_F.f_{Ftud} \quad (4.10)$$

where τ_{Rdc} is shear resistance calculated from equation (4.5), f_{Ftud} is the design value for the residual tensile strength of the fibers, $\eta_F = 1$ and η_{cF} is a scaling factors determined as:

$$\eta_{cF} = max\{1.2 - 0.5f_{Ftuk}; 0.4\} \leq 1.0 \quad (4.11)$$

The characteristic value for residual tensile strength f_{Ftuk} and its corresponding design values f_{Ftud} are determined using the formulations in Annex L, Section L.5.5.1 of the EN 1992-1-1:2023.

4.2.2.3. Shear Resistance for SFRC in members with Transverse Shear Reinforcement

Where steel fibres are combined with traditional transverse reinforcement (stirrups or hoops), the structural model is shifted from a concrete-tension mechanism to an inclined truss framework. In this hybrid state, the term for plain concrete (τ_{Rdc}) is omitted, and the design value of shear strength ($\tau_{Rd,sF}$) is calculated as:

$$\tau_{Rd,sF} = \left(\eta_{sw}.\rho_w.f_{ywd} + \eta_F.f_{Ftud}\right).cot\theta \geq \rho_w.f_{ywd}.cot\theta \quad (4.12)$$

where $\eta_{sw} = 0.75$, $\eta_F = 1$, $\rho_w = \frac{A_{sw}}{s.b_w}$ is the reinforcement ratio of the transverse reinforcement, and f_{ywd} is the value for the design yield stress of the transverse reinforcement.

4.3. Shear Prediction in Circular Sections

The truss analogy, while widely adopted for shear design of RC, was developed and validated principally against rectangular test specimen, making its direct application to circular sections difficult to justify. Unlike rectangular sections, the geometry of circular sections is such that the longitudinal reinforcement is distributed around the section perimeter rather than concentrated in two discrete zones, the compression zone and tension zone, respectively. This makes the definition of the effective depth and the internal lever arm in circular sections during calculations relatively ambiguous, unlike rectangular sections where the longitudinal reinforcement is distinctly located at the top and bottom of the cross-section. Additionally, since the shear reinforcement is circular, the shear stresses are considered to act in the circumferential direction. Therefore, only a component of the shear stress is considered effective in resisting the applied transverse shearing activity, thereby reducing the efficiency of steel hoops or spirals compared to regular stirrups in rectangular sections.

4.3.1. Determination of the Neutral Axis and Effective Depth

The neutral axis divides the section into an upper compression region and bottom tension region, respectively. In circular sections, these two regions constitute circular segments with geometrical influence on the determination of the neutral axis and effective depth, respectively. Early works by Clarke et al. [55] computed the effective depth of circular sections by assuming the position of the neutral axis to be coincident with the section's centroidal axis. This approach, despite being convenient, was later found to be a non-conservative simplification as the true neutral axis position varies with the flexural demand and is not necessarily fixed at mid-depth. The ACI Code-318-05 [53] provides a simplified approach, such that the effective depth is considered to be a factor of 0.8 times the diameter of the circular section (0.8*D*).

A more rigorous approach explored in this work was proposed by Orr et al. [56], which determines the position of the neutral axis following a full strain-compatibility sectional analysis, in which the concrete compression zone is established considering the initial circular geometry of the cross-section, characterized by a segment sector angle ω, as shown in the **Figure 4.2** and **Figure 4.3**, before an equivalent rectangular stress block of arbitrary width (b_w)

is considered, with the area of the compression zone segment and its centroid expressed in closed form as a function of the neutral axis depth.

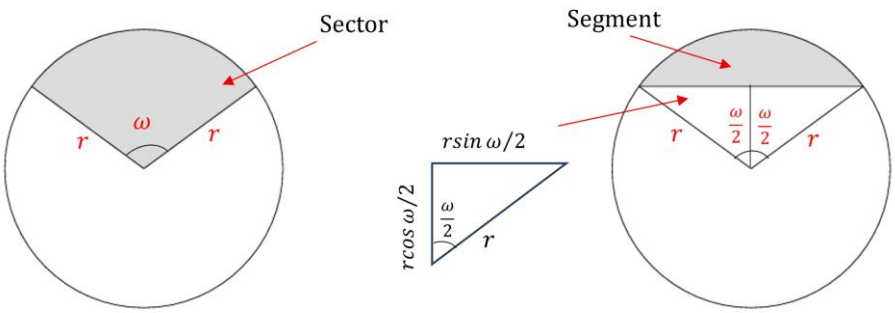


Figure 4.2: Geometrical illustration of the compression zone

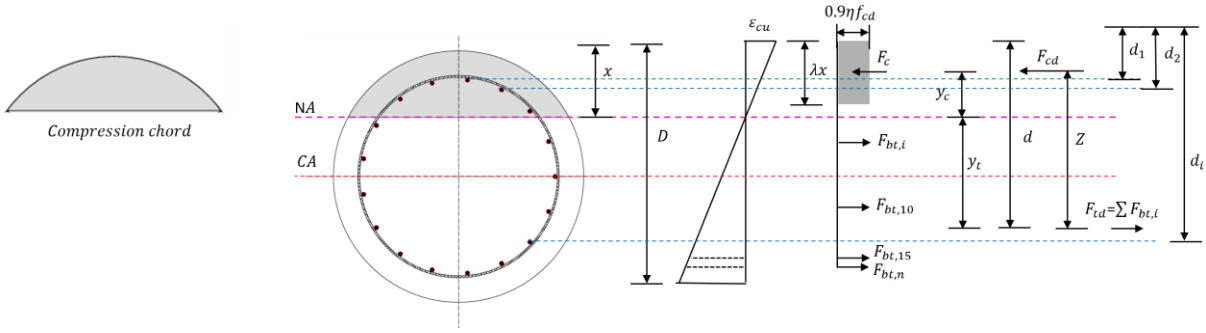


Figure 4.3: Flexural Analysis to determine neutral axis and effective depth [56]

The segment angle ω is determined to satisfy an axial load equilibrium condition, and the resultant concrete compressive force F_{cd} is then determined by applying the design stress block to the compressive area, as shown below.

$$F_{cd} = 0.9.\eta.f_{cd}.A_c \tag{4.13}$$

where f_{cd} is the design value of concrete compressive strength, and A_c is the area of the compression zone, calculated using Eq. (4.14), with a detailed derivation in Annex I.1.

$$A_c = 0.5r^2(\omega - sin\omega) \tag{4.14}$$

The relationship between the neutral axis depth x and the segment angle ω is derived from the stress block theory, where the depth factor $\lambda = 0.8$ is considered. The neutral axis depth is determined from the geometrical relationship below:

$$\cos\left(\frac{\omega}{2}\right) = \frac{(r - \lambda x)}{r} \tag{4.15}$$

such that:

$$x = \frac{r\left(1 - \cos\left(\frac{\omega}{2}\right)\right)}{\lambda} \tag{4.16}$$

where *r* is the radius of the circular cross-section $\left(r = \frac{D}{2}\right)$. The distance of the centroid of the compression segment from the neutral axis depth is obtained using the geometrical relationship shown in Eq. (4.17) below; a detailed derivation is provided in Annex I.2:

$$y_c = \frac{2Dsin^3(\omega/2)}{3(\omega - sin\omega)} - \left(\frac{D}{2} - X\right) \tag{4.17}$$

To determine the effective depth d of the section, the contribution of the longitudinal reinforcement to the internal force equilibrium is evaluated by obtaining the stress-strain behavior of each individual bar in the established tension zone, such that for a given longitudinal bar i, its corresponding depth d_i is measured from the extreme compression fiber at the top to its centroid, as shown in **Figure 4.3**. In this case, the longitudinal bars for which $(d_i > x)$ experience tensile strain, while the bars for which $(d_i < x)$ lie in the compression zone, and are not considered to contribute to the tension resultant. The strain in each corresponding longitudinal bar is obtained using Eq. (4.18):

$$\varepsilon_{s,i} = \varepsilon_{cu}\frac{d_i - x}{x}, \qquad \text{for } d_i > x \tag{4.18}$$

where ε_{cu} is the ultimate crushing strain of the concrete. This expression highlights the relationship between the variation in the neutral axis depth and the tensile strain in the longitudinal steel reinforcement, such that a shallow neutral axis produces larger steel strains and high tensile force contribution to the internal equilibrium. The stress in each bar is then determined as in Eq. (4.19):

$$f_{s,i} = \min\left(E_s\varepsilon_{si}, f_{yd}\right) \tag{4.19}$$

where E_s and f_{yd} is the modulus of elasticity and the design value for the yield stress of the longitudinal steel reinforcement, respectively. The tensile force in each bar is then determined using the following expression:

$$F_{bt,i} = A_{si}.f_{si} \tag{4.20}$$

where A_{si} is the cross-sectional area of bar i. Considering that each bar may experience different tensile strain depending on its geometrical position and distance from the neutral axis, the total tension force is then obtained by summing the contributions of all the bars in tension using Eq. (4.21) as:

$$F_{td} = \sum_{i=1}^{n} F_{bt,i} \tag{4.21}$$

The centroid of the resultant tension force in the equation above is then obtained as in Eq. (4.22):

$$y_t = \frac{\sum_i F_{bt,i}(d_i - x)}{F_{td}} \tag{4.22}$$

The internal lever arm z is calculated as $z = y_c + y_t$, where y_c is the centroid of the concrete compression block determined from Eq. (4.17). The contribution of concrete in tension is neglected. This iterative approach involving the initial determination of the neutral axis depth to establish the compression and tension zones, is suitable for adoption in determining the equivalent effective depth of the strengthened circular pile cross-sections following a similar approach that considers the discrete contribution of the bars in the circular section, as discussed in the next sections.

4.3.2. Equivalent Rectangular Cross-section and Transverse Reinforcement Efficiency

The transformation of circular cross-sections into equivalent rectangular sections is an idealized geometrical simplification accounting for the complex distribution of the stress profile in circular cross-sections. Unlike rectangular sections, where the compression zone width remains constant, the width of a circular compression segment varies non-linearly with the depth of the neutral axis. Consequently, executing fundamental equilibrium equations requires tedious non-linear integration to determine shifting sectional areas and their respective centroids during flexural or shear design. According to the ACI CODE-318-05 framework [53], this simplification is such that the circular geometry of diameter (D) is mapped onto an equivalent rectangle with an effective depth of (0.8D) and a width calibrated to preserve total area, while shear provisions simplify the boundary by setting the effective web width (b_w) equal to the diameter of the circle. Eurocode 2 (BS EN 1992-1-1:2023) [42],

on the other hand, embeds an idealized rectangular truss within the circular boundary, defining the compression chord as a distinct circular segment of depth (X_{sb}) and the tension chord via a selected design width ($b_w \leq D_h$) as shown in **Figure 4.4**.

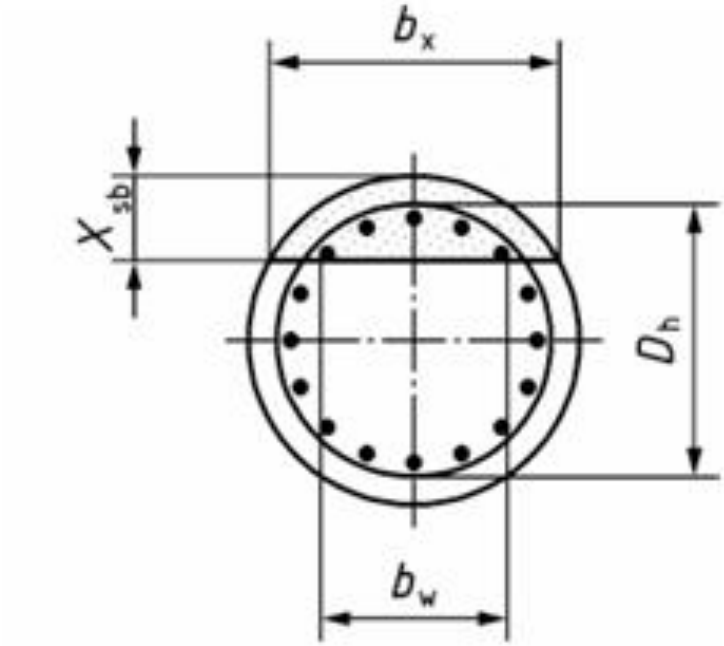


Figure 4.4: Definition of web width b_w

Considering that circular hoops or spirals do not resist the applied shear force with the same efficiency as vertical stirrups, as only a fraction of their cross-sectional area aligns with the shear force in the local tangential direction to contribute to shear resistance, Eurocode 2 uniquely introduces an efficiency reduction factor (b_w / D_h) to scale the effective shear reinforcement area (A_{sw}) to account for the reduced vertical contribution of the hoop segments compared to traditional rectangular stirrups.

4.4. Proposed Analytical Model for Determining Shear in strengthened circular cross-sections

4.4.1. Geometry of Strengthened Circular Cross-section

The geometry of the strengthened circular pile cross-section comprises an existing concrete core consisting of the original as-built concrete, longitudinal and spiral reinforcement; and the strengthening cover, comprising the newly applied concrete or cementitious repair material

together with the added longitudinal and transverse reinforcement made up of steel or GFRP, as shown in **Figure 4.5 a)**. As shown in **Figure 4.5 b)**, the geometrical transformation of the circular cross-section of the strengthened pile into an equivalent rectangular cross-section is presented following the approach discussed in Section 4.3. However, in this case, the geometry of the equivalent rectangular block is modified such that it considers the shear contribution of both the existing reinforcement in the concrete core and the strengthening reinforcement embedded in the concrete core.

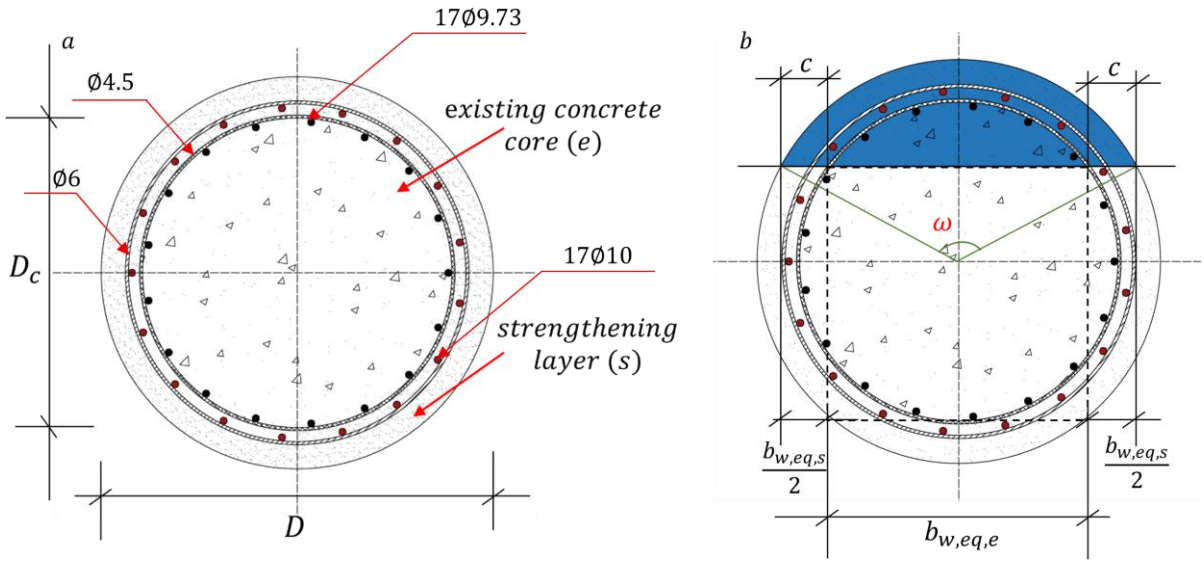


Figure 4.5: a) Geometry of the strengthened cross-section b) Definition of the equivalent rectangular section

For the existing concrete zone, denoted with a subscript e, the equivalent width and depth of the equivalent rectangular cross-section are represented by $(b_{w,eq,e})$, which is calculated to preserve the total area of the existing concrete core using Eq. (4.23):

$$b_{w,eq,e} = \sqrt{\frac{\pi D_c^2}{4}} \tag{4.23}$$

where D_c is the diameter of the existing concrete core, obtained using Eq. (4.24):

$$D_c = D - 2c \tag{4.24}$$

where D is the diameter of the whole circular pile cross-section, and c is the thickness of the concrete cover. For the strengthened concrete zone, denoted with a subscript s, the equivalent width $(b_{w,eq,s})$ is approximated to be double the thickness of the concrete cover (c) on both sides of the circular cross-section, expressed as:

$$b_{w,eq,s} = 2c \tag{4.25}$$

4.4.2. Equations for Predicting the Shear Capacity of the Strengthened Circular Cross-sections

The analytical formulations for the shear design of strengthened circular cross-sections proposed in this chapter are developed on the basis of the truss model introduced in Section 4.2.1 and in **Figure 4.6**. The total shear resistance of the strengthened composite section is taken as the sum of the shear resistance contribution of the existing concrete core ($V_{Rd,e}$) and the strengthening layer in the concrete cover ($V_{Rd,s}$), respectively, as given by Eq. (4.26):

$$V_{Rd} = V_{Rd,e} + V_{Rd,s} \tag{4.26}$$

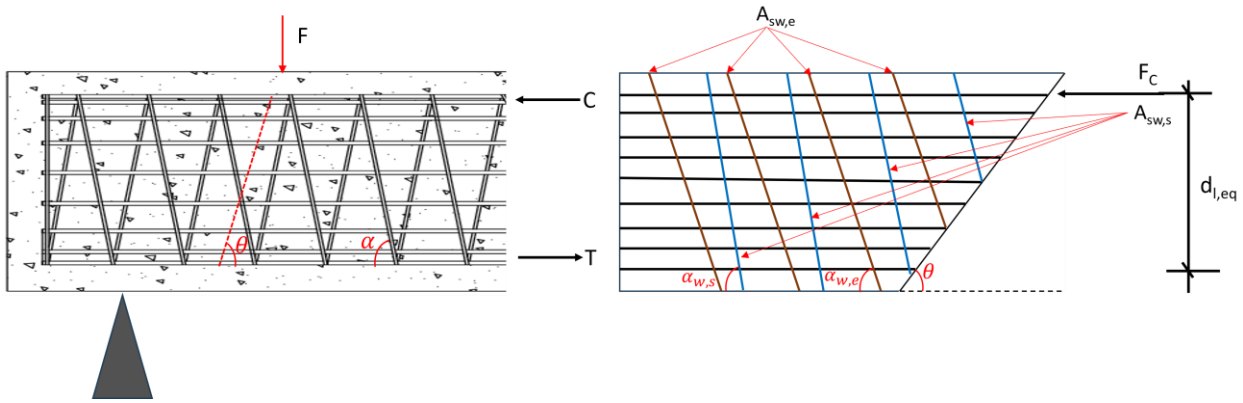


Figure 4.6: Truss model representation of a strengthened pile

$V_{Rd,e}$ and $V_{Rd,s}$ consider the combined shear contribution of both the concrete and shear reinforcement in the corresponding zones of the existing reinforced concrete and the strengthened reinforced concrete cover, respectively, and are calculated based on Eq. (4.26), as shown in Eq. (4.28) and Eq. (4.28), respectively.

$$V_{Rd,e} = V_{Rdc,e} + V_{Rdw,e} \tag{4.27}$$

$$V_{Rd,s} = V_{Rdc,s} + V_{Rdw,s} \tag{4.28}$$

$$V_{Rdf,s} = V_{Rdc,s} + V_{Rdfw,s} \tag{4.29}$$

where FRP strengthening solutions, particularly GFRP longitudinal and transverse reinforcement were used in place of steel, Eq. (4.29) is adopted. $V_{Rdc,e}$ and $V_{Rdc,s}$ are the shear contribution of the existing concrete core and the strengthening concrete at the cover zone, respectively; $V_{Rdw,e}$ and $V_{Rdw,s}$ is the shear contribution of the existing and strengthening transverse reinforcement; and $V_{Rdfw,s}$ is the shear contribution of the FRP strengthening.

4.4.2.1. Transverse Reinforcement Shear Contribution

The shear contribution of the transverse reinforcement term follows directly from the truss equilibrium of Eq. (4.2), applied independently to the existing and strengthening zones as shown in Eq. (4.30), Eq. (4.31) and Eq. (4.32), respectively:

$$V_{Rdw,e} = \frac{A_{sw,e}.f_{sydw,e}}{s_{w,e}}.Z_e.\left(cot\theta + cot\alpha_{w,e}\right).sin\alpha_{w,e} \tag{4.30}$$

$$V_{Rdw,s} = \frac{A_{sw,s}.f_{sydw,s}}{s_{w,s}}.Z_s.\left(cot\theta + cot\alpha_{w,s}\right).sin\alpha_{w,s} \tag{4.31}$$

$$V_{Rdfw,s} = \frac{A_{sf,s}.f_{fydw,s}}{s_{wf,s}}.Z_{f,s}.\left(cot\theta + cot\alpha_{w,s}\right).sin\alpha_{wf,s} \tag{4.32}$$

where $f_{sydw,e}$, $f_{sydw,s}$, and $f_{fydw,s} = E_f.\varepsilon_{fe}$ are the design values of yield stress of the existing steel spiral, strengthening steel spiral and FRP strengthening spiral, respectively; $s_{w,e}$, $s_{w,s}$ and $s_{wf,s}$ is the pitch spacing between the spirals or hoops in the existing and strengthening domains respectively; and Z_e, Z_s and $Z_{f,s}$ correspond to the internal lever arm of each domain related to the equivalent effective depth $(d_{l,eq})$ adopted from the truss model as below:

$$Z_e = 0.9d_{l,eq,e} \tag{4.33}$$

$$Z_s = 0.9d_{l,eq,s} \tag{4.34}$$

$$Z_{f,s} = 0.9d_{l,eq,s} \tag{4.35}$$

where $d_{l,eq,e}$ and $d_{l,eq,s}$ are the equivalent effective depths of existing RC and the strengthening RC, determined after establishing the neutral axis depth as a boundary between the compression zone and the tension zone, following the approach introduced in Section 4.3. The schematic illustration of the flexural analysis to determine the neutral axis depth of the strengthened circular cross-section is shown in **Figure 4.7**.

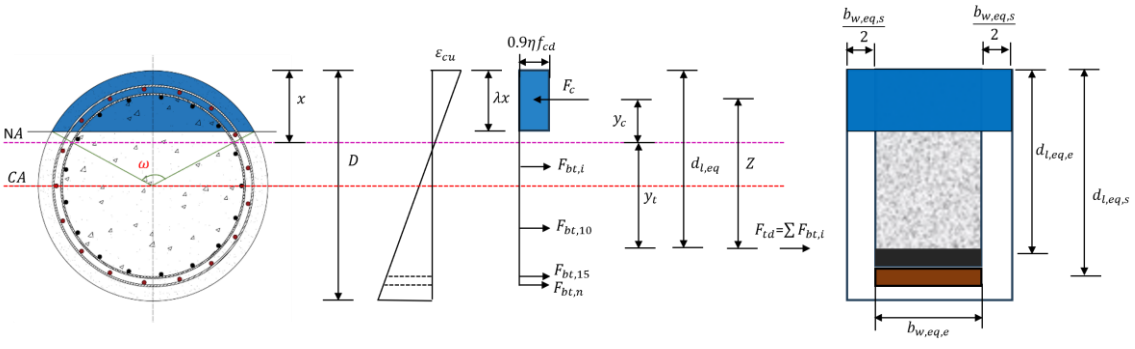


Figure 4.7: Flexural analysis to determine the neutral axis depth of circular strengthened sections

Given that only longitudinal bars in the established tension zone ($d_i > x$) are considered to contribute to the resultant tensile force, $d_{l,eq,e}$ and $d_{l,eq,s}$ were calculated using Eq. (4.36) and Eq. (4.37), measured from the top extreme compression fibre of the circular section.

$$d_{l,eq,e} = \frac{\sum_{i=1}^{nl,e}\left(d_{l,e}^2 A_{l,e}\right)_i}{\sum_{i=1}^{nl,e}\left(d_{l,e} A_{l,e}\right)_i} \tag{4.36}$$

$$d_{l,eq,s} = \frac{\sum_{j=1}^{nl,s}\left(d_{l,s}^2 A_{l,s}\right)_j}{\sum_{j=1}^{nl,s}\left(d_{l,s} A_{l,s}\right)_j} \tag{4.37}$$

where i and j are sequential indices running from 1 to nl,e in the existing domain, and 1 to nl,s in the strengthening domain, respectively; nl,e and nl,s denotes the total number of longitudinal bars situated within the tension zone in the existing and strengthening domains, respectively; nl,s applies to both steel and FRP longitudinal bars depending on the strengthening configuration.

4.4.2.2. Concrete Shear Contribution

The shear contribution of the existing and the strengthening concrete is adopted from Eq. (4.3), which combines the concrete and reinforcement terms, applied to the homogenized equivalent rectangle established in Section 4.3.2, as shown below:

$$V_{Rdc,e} = \tau_{Rdc,e}.b_{w,eq,e}.d_{l,eq,e} \tag{4.38}$$

$$V_{Rdc,s} = \tau_{Rdc,s}.b_{w,eq,s}.d_{l,eq,s} \tag{4.39}$$

where $\tau_{Rdc,e}$ and $\tau_{Rdc,s}$ are the shear resistance of the uncracked concrete without shear reinforcement in the existing concrete and strengthening concrete cover, calculated using Eq. (4.40) and Eq. (4.41), respectively.

$$\tau_{Rdc,e} = \frac{0.66}{\gamma_v}.\left(100.\rho_{l,eq,e}.f_{ck,e}.\frac{d_{dg,e}}{d_{l,eq,e}}\right)^{1/3} \tag{4.40}$$

$$\tau_{Rdc,s} = \frac{0.66}{\gamma_v}.\left(100.\rho_{l,eq,s}.f_{ck,s}.\frac{d_{dg,s}}{d_{l,eq,s}}\right)^{1/3} \tag{4.41}$$

where $\rho_{l,eq,e}$ and $\rho_{l,eq,s}$ are the equivalent reinforcement ratios of the longitudinal bars in the tension zone, calculated as:

$$\rho_{l,eq,e} = \frac{\sum_{i=1}^{nl,e}\left(d_{l,e}A_{l,e}\right)_i}{b_{w,eq,e}d_{l,eq,e}^2} \tag{4.42}$$

$$\rho_{l,eq,s} = \frac{\sum_{j=1}^{nl,s}\left(d_{l,s}A_{l,s}\right)_j}{b_{w,eq,s}d_{l,eq,s}^2} \tag{4.43}$$

The parameters for the roughness size of the of the aggregates $d_{dg,e}$ and $d_{dg,s}$ for the existing concrete are calculated using the following equations:

$$d_{dg,e} = 16 + D_{lower,e} \leq 40\text{mm}, \qquad f_{ck} \leq 60\text{MPa} \tag{4.44}$$

$$d_{dg,e} = 16 + D_{lower,e}\left(\frac{60}{f_{ck,e}}\right)^2 \leq 40\text{mm}, \qquad f_{ck} > 60\text{MPa} \tag{4.45}$$

$$d_{dg,s} = 16 + D_{lower,s} \leq 40\text{mm}, \qquad f_{ck} \leq 60\text{MPa} \tag{4.46}$$

$$d_{dg,s} = 16 + D_{lower,s}\left(\frac{60}{f_{ck,s}}\right)^2 \leq 40\text{mm}, \qquad f_{ck} > 60\text{MPa} \tag{4.47}$$

4.5. Axial load influence on shear resistance terms

As discussed in Section 4.2.2, the influence of the axial compressive load is on the fundamental equation for determining the design value of shear resistance contribution of RC (τ_{Rdc}) is considered in this model, with modifications on Eq. (4.40) and Eq. (4.41), respectively, with special considerations for the material types with plain concrete or SFRC used as the core or cover regions, respectively. For the existing concrete core region with plain concrete, Eq. (4.48) is modified to its axial-load-dependent form as:

$$\tau_{Rdc,e} = \tau_{Rdc,0,e} - k_{1,e}.\sigma_{cp,e} \tag{4.48}$$

where $\tau_{Rdc,0,e}$ is the design value for the shear resistance of the existing concrete core obtained from equation (4.40), $\sigma_{cp,e} = \frac{N_{Sd,e}}{A_{c,e}}$ is the axial stress of the existing concrete core, calculated based on Eq. (4.6), where $N_{Sd,e}$ is taken as a negative value for axial compression. The factor $k_{1,e}$ for the existing core region is determined as:

$$k_{1,e} = \frac{0.5}{\alpha_{cs,0,e}}\left(e_p + \frac{d_{l,eq,e}}{3}\right).\frac{A_{c,e}}{b_{w,eq,e}.z_e} \leq 0.18.\frac{A_{c,e}}{b_{w,eq,e}.z_e} \tag{4.49}$$

where $e_p = 0$, $A_{c,e}$ is the area of the existing concrete core, $\alpha_{cs,0,e}$ based on Eq. (4.8) is taken as $\alpha_{cs,0,e} = d_{l,eq,e}$. For the strengthened cover region with plain concrete, Eq. (4.41) is modified to its axial-load-dependent form as:

$$\tau_{Rdc,s} = \tau_{Rdc,0,s} - k_{1,s}.\sigma_{cp,s} \tag{4.50}$$

where $\tau_{Rdc,0,s}$ is the design value for the shear resistance of the strengthened concrete cover obtained from Eq. (4.41), $\sigma_{cp,s} = \frac{N_{Sd,s}}{A_{c,s}}$ is axial stress of the strengthened cover, calculated based on Eq. (4.6), where $N_{Sd,s}$ is taken as a negative value for axial compression. The factor $k_{1,s}$ for the strengthened region is determined as:

$$k_{1,s} = \frac{0.5}{\alpha_{cs,0,s}}\left(e_p + \frac{d_{l,eq,s}}{3}\right).\frac{A_{c,s}}{b_{w,eq,s}.z_s} \leq 0.18.\frac{A_{c,s}}{b_{w,eq,s}.z_s} \tag{4.51}$$

where $A_{c,s}$ is the area of the strengthened concrete cover, $\alpha_{cs,0,s}$ based on Eq. (4.8) is taken as $\alpha_{cs,0,s} = d_{l,eq,s}$. Notably, the applied axial force N_{Sd} is distributed between the existing core and the strengthening cover in direct proportion to the axial rigidity of each domain, expressed as a product of the domain's concrete modulus of elasticity and concrete cross-sectional area ($E_c A_c$). The derivation of this distribution, from equilibrium and strain-compatibility first principles, is presented in full in Annex II.

In the case where the section is strengthened with SFRC but without transverse reinforcement, the following equation is adopted for the design shear resistance:

$$\tau_{Rd,cF,s} = \eta_{cF}.\tau_{Rdc,s} + \eta_F.f_{Ftud} \tag{4.52}$$

where $\tau_{Rdc,s}$ is the design value for the shear resistance of the strengthened cover obtained according to Eq. (4.50), $\eta_F = 1$, η_{cF} is determined according to Eq. (4.11), and f_{Ftud} is established according to the formulations in Annex L, Section L.5.5.1 of the Eurocode (EN 1992-1-1:2023). Where the cover region is strengthened using SFRC with transverse reinforcement, the following equation is adopted for the design shear resistance:

$$\tau_{Rd,sF,s} = \left(\eta_{sw}.\rho_{w,s}.f_{ywd} + \eta_F.f_{Ftud}\right).cot\theta \geq \rho_{w,s}.f_{ywd}.cot\theta \tag{4.53}$$

where $\eta_{sw} = 0.75$, $\eta_F = 1$, $\rho_{w,s}$ is the reinforcement ratio of the transverse reinforcement in the strengthened region determined using Eq. (4.54) and Eq. (4.55), for steel or GFRP hoops respectively; $A_{sw,s}$ and $A_{swf,s}$ is the cross-sectional area of the steel and GFRP hoops.

$$\rho_{w,s} = \frac{A_{sw,s}}{s_{w,s}.\, b_{w,eq,s}} \tag{4.54}$$

$$\rho_{w,fs} = \frac{A_{sw,fs}}{s_{wf,s}.\, b_{w,eq,s}} \tag{4.55}$$

4.6. Design Application of the Model

The procedure described in Section 4.4 is applied to a representative circular pile section shown in **Figure 4.8**. The existing concrete core comprises plain concrete ($f_{ck,e} = 35$ MPa), the cover region is assessed with different configurations: primarily a plain concrete matrix ($f_{ck,s} = 60$ MPa) and SFRC with a performance class 3c, reinforced with either steel or GFRP longitudinal bars and hoops. Two levels of corrosion damage applied to the cross-sectional area of existing longitudinal and transverse spiral reinforcement are considered at 25% and 50% respectively, which are applied interchangeably to either the existing longitudinal steel (L), the spirals (T), or both cases in a combined configuration (LT).

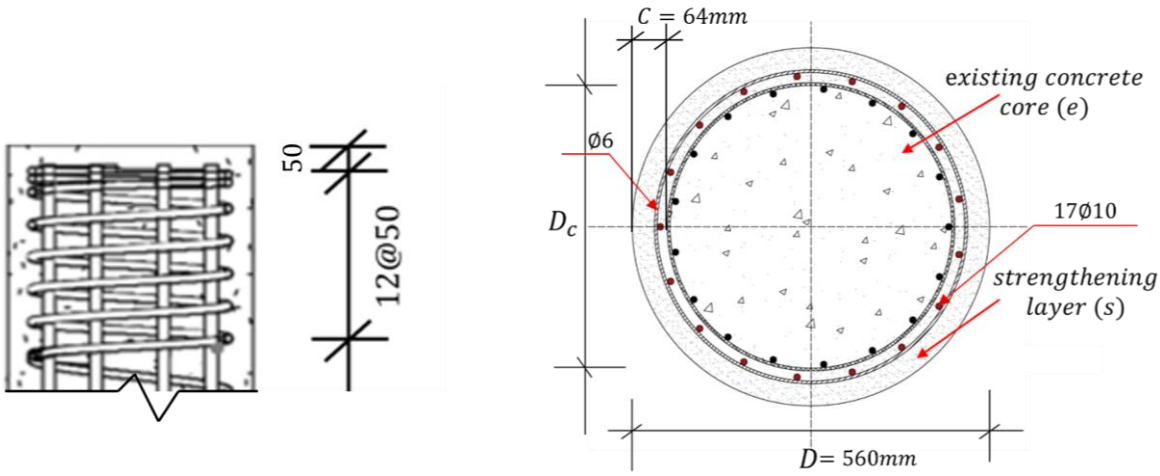


Figure 4.8: Geometry of the circular strengthened pile section

The relevant material and geometric properties are summarized in **Table 4.1** to **Table 4.3**.

Table 4.1: Properties for the plain concrete and SFRC strengthening

Specimen	$f_{ck,e}$ (MPa)	$f_{ck,s}$ (MPa)	$D_{lower,e}$ (mm)	$D_{lower,s}$ (mm)
PC60	35	60	10	16
SFRC (3c/60)	35	60	10	16

Table 4.2: Properties of the steel reinforcement

Reinforcement Type	φ_e(mm)	φ_s(mm)	$f_{sykw,e}$ (MPa)	$f_{sykw,s}$ (MPa)
Longitudinal	9.73	10	1581	1581
Transverse	4.5	6	485	485

Table 4.3: Properties of the GFRP reinforcement

Reinforcement Type	φ_s(mm)	E_f (GPa)	f_{fuk}(MPa)	ε_{fe}
Longitudinal	10	50	1000	0.004
Transverse	6	50	1000	0.004
Strut angle: $\theta = 45°$	Reinforcement angle: $\alpha_{w,e} = 90° - \arctan\left(\frac{S_{w,e}}{\pi D_c}\right), \alpha_{w,s} = \alpha_{wf,s} = 90°$			

4.7. Results for the Shear Strengthening Prediction

The results from the analysis are summarized in **Table 4.4**. The results from the analysis are summarized in the table below. For each of the four cover-reinforcement configurations examined, the table reports the existing-core term $V_{Rd,e}$, the strengthening-domain term $V_{Rd,s}$, and the total shear resistance V_{Rd}, across the corrosion cases and axial load levels considered, allowing the effect of corrosion severity and location, axial compression, and strengthening material to each be isolated by reading the table along the corresponding row, column, or configuration block. The PC60 configuration with steel bars and hoops, at its least severe corrosion case, serves as a reference point: being closest to a conventional stirrup-reinforced section, its predicted resistance can be independently cross-checked against the established EC2 truss model and CSCT concrete term underlying the proposed two-domain formulation, before the novel GFRP, SFRC, and superposition elements are introduced. The physical interpretation of the resulting trends, and their relative magnitude, is discussed in detail in Chapter 5, Section 5.3.

Table 4.4: Summary of the predicted shear strengthening results

Cover Material	Configuration	N_{Sd} (N)	$V_{Rd,e}$ (kN)	$V_{Rd,s}$ (kN)	V_{Rd} (kN)
PC60 (Plain concrete + Steel bars and hoops)	25LS	0	157	202	360
		$0.6N_{Ed}$	523	497	1020
	50LS	0	148	202	351
		$0.6N_{Ed}$	515	497	1012
	25TS	0	142	202	345
		$0.6N_{Ed}$	504	497	1001
	50TS	0	120	202	323
		$0.6N_{Ed}$	479	497	976
	25LTS	0	135	202	338
		$0.6N_{Ed}$	498	497	995
	50LTS	0	105	202	307
		$0.6N_{Ed}$	465	497	962
	25LGFRP	0	156	121	277

Cover Material	Configuration	N_{Sd} (N)	$V_{Rd,e}$ (kN)	$V_{Rd,s}$ (kN)	V_{Rd} (kN)
PC60 (Plain concrete + GFRP bars and hoops)		$0.6N_{Ed}$	523	405	928
	50LGFRP	0	146	121	267
		$0.6N_{Ed}$	515	405	920
	25TGFRP	0	142	121	263
		$0.6N_{Ed}$	504	405	909
	50TGFRP	0	120	121	242
		$0.6N_{Ed}$	479	405	884
	25LTGFRP	0	135	121	255
		$0.6N_{Ed}$	498	405	903
	50LTGFRP	0	104	121	225
		$0.6N_{Ed}$	465	405	870
SFRC (3c/60) + (GFRP bars, without transverse reinforcement)	25LNFRC	0	155	141	296
		$0.6N_{Ed}$	523	363	886
	50LNFRC	0	146	141	287
		$0.6N_{Ed}$	515	363	878
	25TNFRC	0	142	141	282
		$0.6N_{Ed}$	504	363	867
	50TNFRC	0	120	141	261
		$0.6N_{Ed}$	479	363	842
	25LTNFRC	0	134	141	275
		$0.6N_{Ed}$	498	363	861
	50LTNFRC	0	104	141	245
		$0.6N_{Ed}$	465	363	828
SFRC (3c/60) + (GFRP bars, with transverse reinforcement)	25LSFRC	0	155	163	319
		$0.6N_{Ed}$	523	190	713
	50LSFRC	0	146	163	310
		$0.6N_{Ed}$	515	190	705
	25TSFRC	0	142	163	305
		$0.6N_{Ed}$	504	190	694
	50TSFRC	0	120	163	284
		$0.6N_{Ed}$	479	190	669
	25LTSFRC	0	134	163	298
		$0.6N_{Ed}$	498	190	688
	50LTSFRC	0	104	163	268
		$0.6N_{Ed}$	465	190	655

Notes to Table:

PC – Plain Concrete

25 – 25% Corrosion

50 – 50% Corrosion

$$\text{Corrosion specification} \begin{cases} \text{L} - \text{Longitudinal reinforcement} \\ \text{T} - \text{Transverse reinforcement} \\ \text{LT} - \text{Longitudinal} + \text{Transverse} \end{cases}$$

SFRC – Steel Fiber Reinforced Concrete

GFRP – Glass Fiber Reinforced Polymer Bars

4.8. Summary

This chapter has developed an analytical model for the shear capacity assessment of strengthened circular RC sections that combine an existing, potentially corrosion-deteriorated core with a newly applied strengthening cover. Starting from the governing shear equations of the truss model and the critical shear crack theory, and from the modification of these equations to account for axial load interaction, the chapter addressed the specific geometric complications of circular and octagonal sections, namely the determination of the neutral axis and effective depth, and the equivalent-rectangle idealization used to establish the transverse reinforcement efficiency of a circular or spiral reinforcement layout. The proposed model superposes the shear resistance of the existing core domain and the strengthening cover domain, $V_{Rd} = V_{Rdc} + V_{Rds}$, with each domain contributing a concrete term evaluated through the critical shear crack theory and a transverse reinforcement term evaluated through the variable-angle truss model for steel or FRP hoops, or through the EN 1992-1-1:2023 Annex L formulation for SFRC with or without discrete hoops, as applicable to each strengthening configuration.

The influence of axial load was accounted for through both an implicit channel, via the deepening of the neutral axis with increase in axial compressive stress; and an explicit channel, via the axial compressive stress term in the concrete shear resistance equation. The model was then applied to the representative circular strengthened pile sections, considering four cover-reinforcement configurations, plain concrete with steel bars and hoops, plain concrete with GFRP bars and hoops, SFRC without discrete hoops, and SFRC with discrete GFRP hoops, each evaluated at 25% and 50% corrosion levels applied individually to the longitudinal reinforcement (L), the transverse reinforcement (T), or both in combination (LT), and at two axial load levels representative of the unloaded and service-loaded pile condition (N_{Sd}=0.6N_{Ed}), which was specifically selected considering the maximum axial compressive moment common at $0.6\mathrm{N}_{\mathrm{Ed}}$ from the N-M flexural analysis presented in Chapter 3. The results of shear capacity predictions, summarized in **Table 4.4**, are discussed in Chapter 5.

5. Results and Discussion of the predicted Flexural, Axial and Shear Capacity of the Deteriorated and Strengthened Piles

5.1. Introduction

This chapter applies the analytical framework presented in Chapters 3 and 4 to the specific problem of structural capacity assessment for the deteriorated concrete piles extracted during the demolition of the Earl C. Davis Memorial Bridge. As introduced in Chapter 1, the bridge was demolished after a service life of approximately 50 years, and a total of 9 octagonal RC pile samples were extracted for research purposes, providing a unique case-study for assessing the flexural and shear capacity of piles subjected to prolonged marine conditions and their capacity recovery achievable through different repair and strengthening strategies.

5.2. Flexural and Axial Capacity Assessment

This section presents the results obtained from the layered sectional analyses conducted in DOCROS based on the analytical framework, constitutive models and formulations introduced in Chapter 3, where the cross-section was evaluated under combined axial and flexural loading. As shown in **Figure 5.1**., the RC pile sections are isolated from the critical tidal zone of the deteriorated pile, and assessed across three core structural states as follows: (i) as-built undamaged state, (ii) deteriorated state with concrete cover loss and reduced cross-sectional area of the reinforcement due to corrosion, and (iii) strengthening and repair configurations ranging from the use of plain concrete of different compressive strengths, SHCC and SFRC for cover replacement, to GFRP bars and external CFRP confinement jacket were adopted.

5.2.1. Geometry of the Pile Assessment Configurations

The geometrical details of the assessed pile configurations were established based on the original drawings, where the as-built pile section retains its true octagonal geometry, with a diameter of 560 mm and a concrete cover thickness of 64 mm (see **Figure 5.1**). The deteriorated pile section geometry was modelled to account for the lost concrete cover, with

a diameter Dc = 432 mm. The strengthened section, however, is deliberately reconstructed as circular, using the same nominal diameter of D = 560 mm and a concrete cover of c = 64 mm, instead of the original octagonal shape. The circular shape for strengthening configurations is selected because the process of casting a new concrete cover, or applying an FRP jacket, particularly in an underwater repair environment, would be more convenient in a circular pile configuration than in an octagonal geometry. Adopting a circular strengthened geometry, at the same characteristic diameter as the original octagonal section, therefore reflects a realistic and structurally favourable site repair detail, and is consistent with the equivalent-circular idealization already adopted for the shear model in Chapter 4.

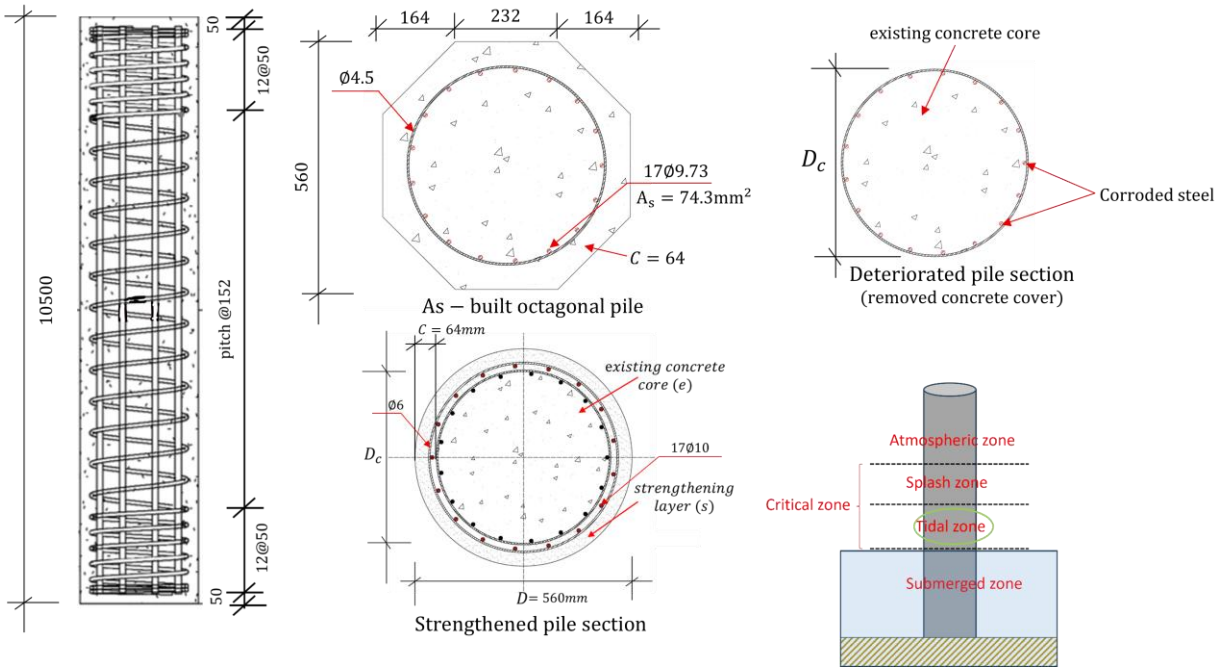


Figure 5.1: Geometrical details of the assessment configurations

The summary of the different pile section configurations assessed for flexural and axial capacity are presented in **Table 5.1**.

Table 5.1: Summary of the predicted shear strengthening results

Assessed Configuration	State	Cover material	Additional reinforcement	Corrosion level (%)
ABOP	As-built	Plain concrete	-	0
DTP25/DTP50	Deteriorated	-	-	25/50

Assessed Configuration	State	Cover material	Additional reinforcement	Corrosion level (%)
STPC35 (UPC35)	Strengthened	Plain concrete (35MPa)	-	25/50
STPC60 (UPC60)	Strengthened	Plain concrete (60MPa)	-	25/50
FRC 3a/3c/3e/6a/8a/8e	Strengthened	SFRC (3a, 3c, 3e, 6a, 8a, 8e)	-	25/50
SHCC35	Strengthened	SHCC (35MPa)	-	25/50
GFRP60	Strengthened	Plain concrete (60MPa)	GFRP longitudinal reinforcement	25/50
CPC35	Strengthened	Plain concrete (35MPa)	Externally bonded CFRP confinement	25/50
CPC60	Strengthened	Plain concrete (60MPa)	Externally bonded CFRP confinement	25/50

The flexural and axial compressive capacity of each configuration and state was characterized by N-M interaction diagrams, for the values corresponding to the ultimate moments of the applied axial loads in the range ($N_{Sd} = 0N_{Rd}, 0.1N_{Rd}, 0.2N_{Rd}, 0.3N_{Rd}, 0.4N_{Rd}, 0.5N_{Rd}, \dots, N_{Rd}$). The results from the N-M interaction diagrams are shown and discussed below.

5.2.2. As-Built vs. Deteriorated Pile Capacity Assessment

The comparison between the original octagonal as-built pile section and the deteriorated section was modelled in this study to represent the most likely severe damage exhibited by the extracted pile specimens after a 50-year service life. The as-built octagonal pile was modelled in its original undamaged state, while the deteriorated section was modelled to account for uniform corrosion induced damage on the existing cross-sectional area of the longitudinal prestressing steel cables at 25% and 50% damage levels respectively, accompanied by concrete cover spalling and loss caused by expansive rust products.

As shown in **Figure 5.2**, the N-M envelope shows a uniform decrease in the moment capacity of the pile sections with increasing levels of corrosion. The case with 50% corrosion (DTP50) shows a markedly more severe reduction in moment capacity than the 25% case (DTP25). This is consistent with the progressive nature of deterioration of RC marine structures due to corrosion during their service life: as corrosion progresses, the prestressing steel loses cross-sectional area, the concrete cover spalls further, and the confinement provided by the octagonal geometry diminishes.

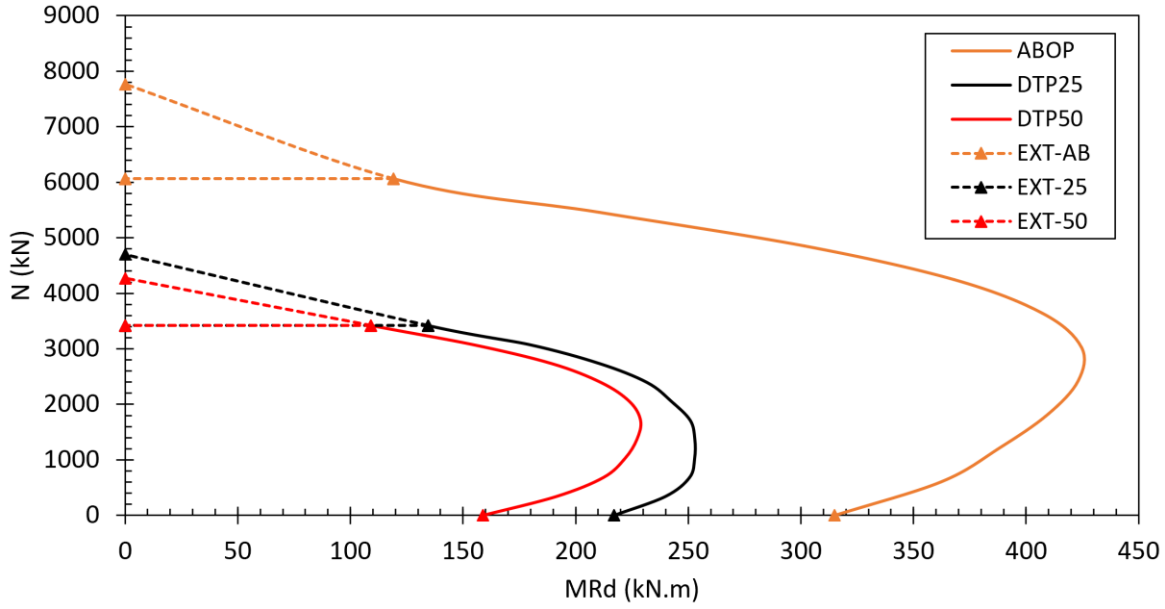


Figure 5.2: N-M interaction comparison of the as-built pile (ABOP) with the deteriorated unstrengthened sections at 25% (DTP25) and 50% (DTP50) corrosion level. EXT are extrapolations to pure axial compression, calculated in each case as $N_{Rd} = A_c f_c + A_s f_s$ (actual theoretical value) and $N_{Rd} = A_c f_c$ (safety cap), respectively.

The reference axial capacity in pure compression $(\mathrm{N_{Rd}})$ of the as-built octagonal pile case (ABOP) dropped by approximately 40% and 80% at 25% and 50% corrosion levels respectively, due to the loss of the concrete cover layer in the deteriorated cases, DTP25 and DTP50, respectively. This loss of the concrete cover contributed to the reduction in the compression block of the cross-sections, thereby reducing the capacity of the deteriorated pile sections to sustain high axial loads. The moment capacity in pure bending, on the other hand, was particularly sensitive to corrosion damage: it dropped by about 31% at 25% corrosion and 49% at 50% corrosion level respectively, with reference to ABOP. The overall reduction in the cross-sectional area of the prestressing steel and the pile-section led to the reduction lever arm of the cross-section, thereby decreasing the flexural resistance capacity of the pile section. The

deterioration also affects the neutral axis position, causing earlier crushing in the compression zone and earlier yielding in the tension zone, with increase in corrosion.

5.2.3. Strengthening with Plain-Concrete (PC35 and PC60) for cover repair

In this section, the effect of the cover repair with plain concrete grades of increasing compressive strengths, C35 and C60, respectively, without additional reinforcement, is explored independently for the repair configurations STPC35 and STPC60 at 25% and 50% corrosion level, respectively. Strengthening the deteriorated piles with plain concrete covers of 35 MPa and 60 MPa produces a clear restoration of structural capacity as shown in **Figure 5.3** and **Figure 5.4**, respectively.

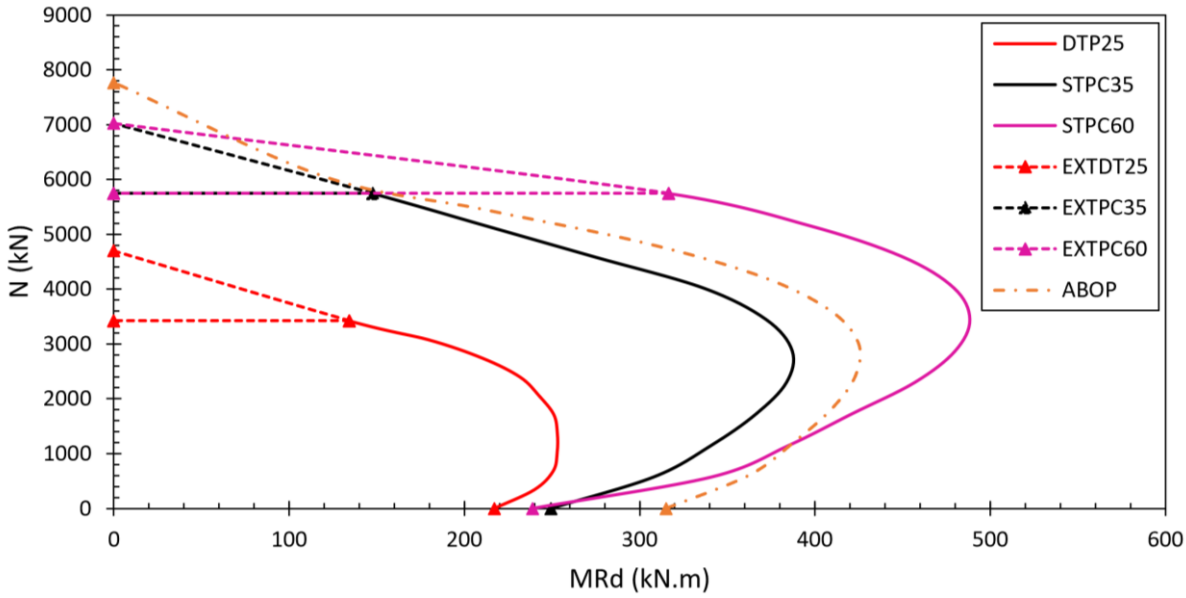


Figure 5.3: N-M interaction diagram for repair configurations STPC35 and STPC60, with plain concrete cover repair at 25% corrosion level. DTP25 is the deteriorated pile at 25% corrosion level. EXT are extrapolations to pure axial compression, calculated in each case as $N_{Rd} = A_c f_c + A_s f_s$ (actual theoretical value) and $N_{Rd} = A_c f_c$ (safety cap), respectively.

The cross-section strengthened with higher-strength concrete (STPC60) provided a more pronounced improvement than the cross-section with lower strength concrete (STPC35), particularly in upper compression zone of the interaction diagram, where compressive stresses dominate. The maximum moment capacity at the balance point increased by 35-48% at 25% corrosion, and by 38-52% at 50% corrosion damage; a significant increase in the axial compressive capacity of the strengthened pile sections compared to the deteriorated cases, DTP25 and DTP50, respectively. Notably, STPC60 restored the axial compressive capacity

beyond that of the as-built case (ABOP), while STPC35 still underperformed compared to ABOP, which can be attributed to the minor contribution of the existing steel in compression in the ABOP, unlike STPC35 with reduced cross-sectional area of the longitudinal steel due to corrosion damage. Overall, the restored concrete cover improved the overall stiffness of the compression zone, thereby increasing the capacity of the section to sustain higher axial loads before crushing.

In pure bending, the moment capacity of the cross-sections was increased by 9-12% at 25% corrosion; and 15-20% at 50% corrosion, respectively, slightly compensating for the lost flexural capacity in the deteriorated cases DTP25 and DTP50. This increase in bending resistance is attributed to the increased effective depth and internal lever arm of the strengthened cross-sections, compared to the deteriorated cross-sections, leading to improved flexural resistance. However, the restored capacity of STPC35 and STPC60 in pure bending still remained lower than ABOP, as restoring the cover with plain concrete does not fully compensate for the tensile strength lost in the corroded longitudinal reinforcement.

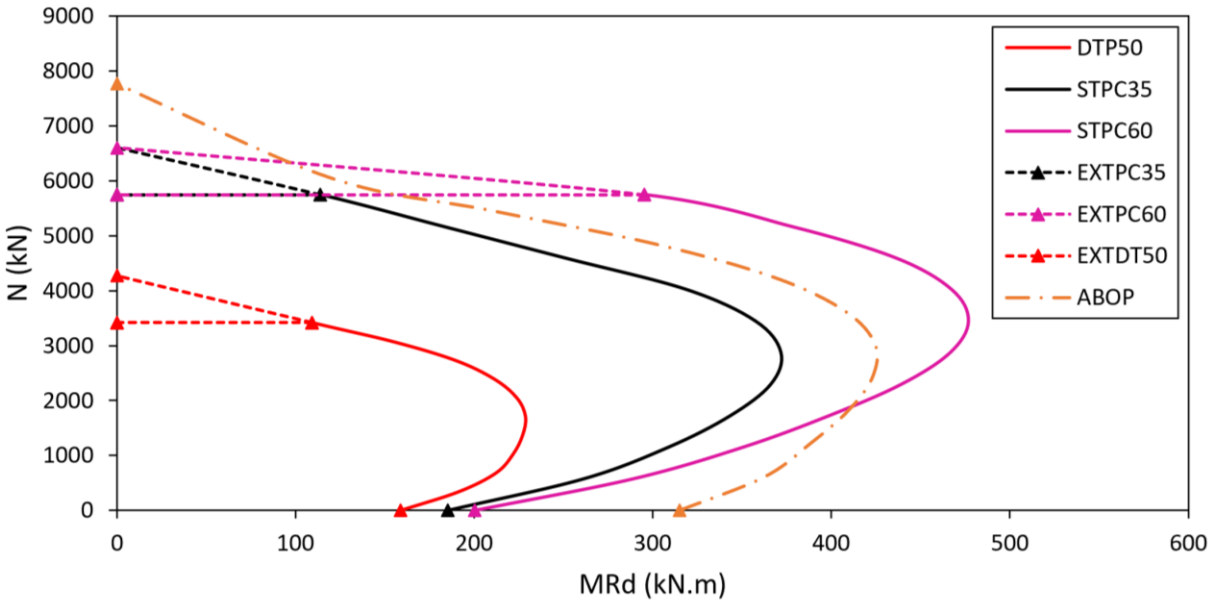


Figure 5.4: N-M interaction diagram for repair configurations STPC35 and STPC60, with plain concrete cover repair at 50% corrosion level. DTP50 is the deteriorated pile at 50% corrosion level.

Overall, the benefits of using higher grade concrete for cover repair are clearly visible, especially in compression, with the 60 MPa cover consistently outperforming the 35 MPa cover, as higher-strength concrete provides greater compressive resistance and stiffness;

allowing the section to sustain higher axial compressive stresses before reaching its ultimate strain.

5.2.4. Strengthening with SFRC for cover repair

In this section, the effects of introducing steel fibres into a selected C60 concrete cover matrix are presented, for 6 Performance Classes (3a, 3c, 3e, 6a, 8a and 8e), established according to the EN 1992-1-1:2023 Annex L. As discussed in Chapter 3, SFRC strengthening produces capacity improvements due to the contribution of the steel fibres, that provide post-crack residual strength through a crack bridging mechanism, which improves both the tensile and compressive ductility of the strengthened sections.

As shown in **Figure 5.5** and **Figure 5.6**, the residual tensile stresses provided by SFRC allow the strengthened section to sustain higher bending moments compared to the reference pile section strengthened with plain concrete (PC60), particularly in ductility classes with higher post-crack tensile behaviour.

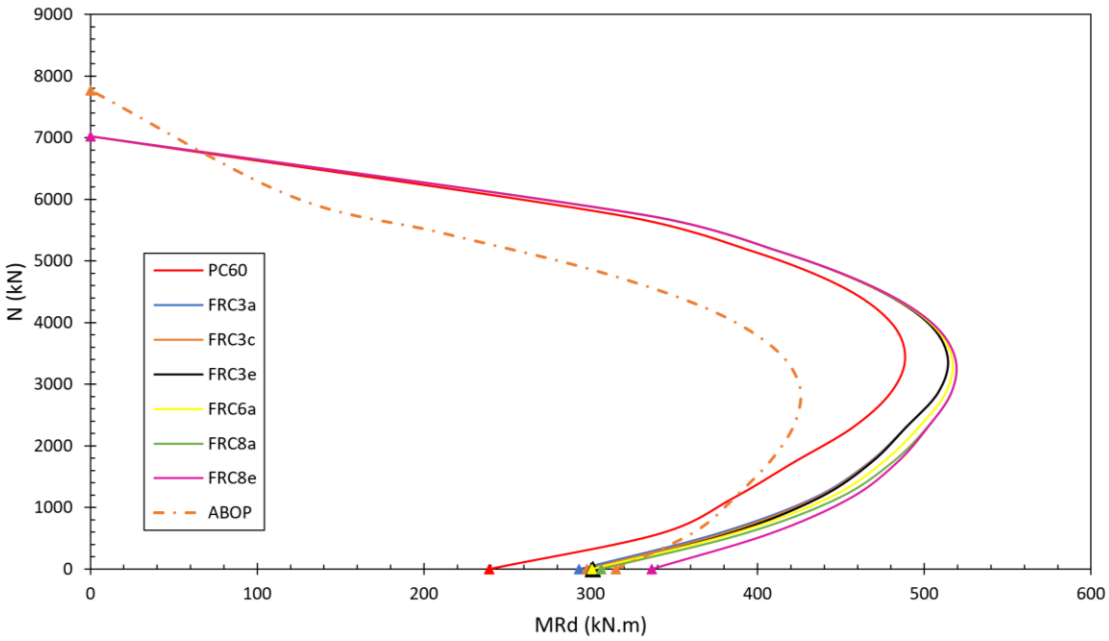


Figure 5.5: N-M interaction diagram for SFRC cover repair with performance classes (3a-8e), compared against the plain C60 cover (PC60), at 25% corrosion level.

Notably, the strengthening case with ductility class 8e produced the largest enhancement in moment capacity of the strengthened pile sections in pure-bending, compared to the other ductility classes (3a, 3c, 3e, 6a and 8a), the reference cases PC60 and ABOP, at both corrosion

levels of 25% and 50% respectively. However, the increase in the bending moment capacity among the strengthening configurations with lower ductility classes (3a, 3c, 3e, 6a and 8a) remained marginally low, as the difference in the residual tensile strengths while moving from 3a to 8a was more less insignificant. This shows that a ductility class with high residual tensile strength produces a large post-cracking tensile contribution in the tension zone, thereby enhancing its moment capacity in pure bending. Additionally, the improved compressive ductility also allows the section to maintain compressive resistance over larger curvature demands. As shown in Figure 5.5 and Figure 5.6, the moment capacity at the balanced point increased modestly among the prescribed performance classes (3a, 3c, 3e, 6a and 8a) at both corrosion levels, but was significantly higher than that of the reference pile sections, PC60 and ABOP respectively.

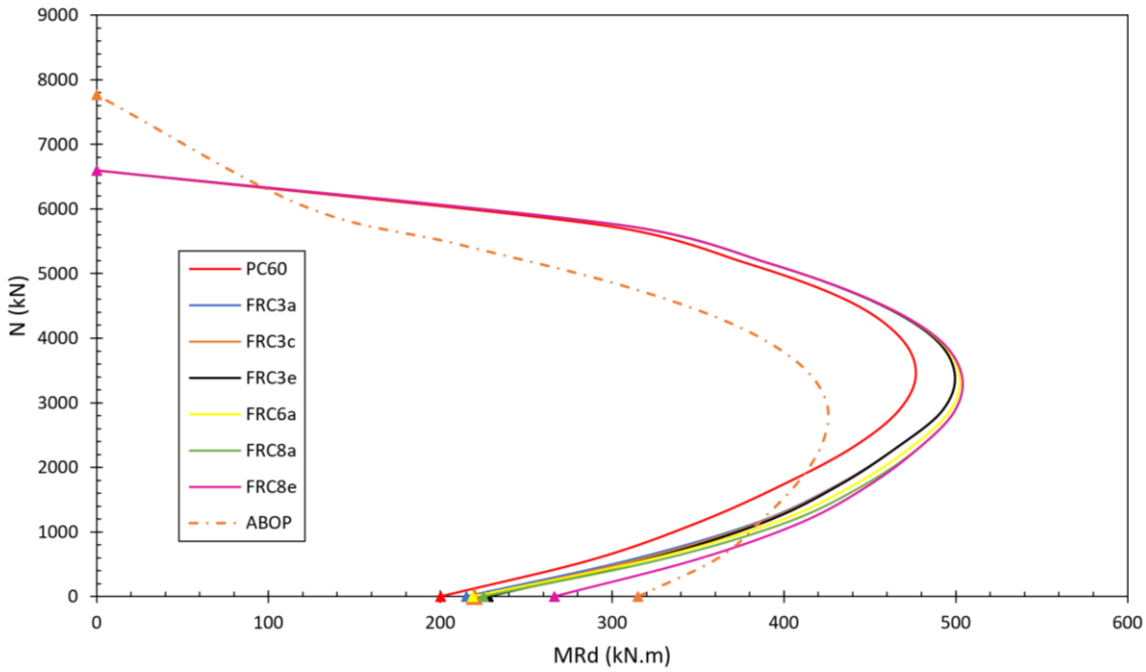


Figure 5.6: N-M interaction diagram for SFRC cover repair with performance classes (3a-8e), compared against the plain C60 cover (PC60), at 50% corrosion level.

The effect of corrosion damage was significant in the evaluation of the effectiveness of the SFRC strengthening. Given that the cross-sectional area and tensile resistance of the existing longitudinal steel reduced with increased levels of corrosion, the fibre contribution to the tensile capacity of the strengthened sections increased proportionately. Notably, the lower ductility classes (3a, 3c, 3e, 6a and 8a) restored the bending moment capacity of the strengthened pile sections beyond the reference case strengthened with plain concrete PC60, but still remained well below the as-built case at 25% corrosion level (see **Figure 5.5**), while at

50% corrosion level, all the strengthening configurations from 3a to 8e did not exceed the pure bending moment capacity of the as-built pile section (see **Figure 5.6**).

At 25% corrosion, the prestressing steel retains most of its cross-section, so the fibres act as a supplementary mechanism rather than a primary tensile component. At 50% corrosion, however, the steel area is significantly reduced, and the tension zone becomes more reliant on the fibre crack bridging mechanism. Consequently, the benefit of SFRC is typically larger at 50% corrosion than at 25% corrosion. Even so, the absolute moment capacity at 50% corrosion remains lower than in the 25% corrosion case, because the geometric lever arm and steel contribution cannot be fully restored by fibres alone.

Overall, SFRC strengthening provided a balanced improvement in both bending and axial compressive capacity, with the magnitude of improvement depending strongly on the fibre performance class. Its benefits are more attributed to ductility, crack control, and resilience rather than increased flexural capacity, which is a significant consideration in the strengthening of marine structures vulnerable to corrosion damage.

5.2.5. Effect of GFRP Longitudinal Bar Reinforcement in the C60 Concrete Cover

The incorporation of GFRP bars within the 60 MPa concrete cover strengthening produces a distinct enhancement in structural performance, particularly in the flexural-dominated regions of the interaction diagram. GFRP bars provide additional tensile reinforcement that remains elastic up to failure, allowing the section to sustain higher tensile strains without yielding. This behaviour complements the existing deteriorated steel and significantly improves the section's ability to resist bending by compensating for the tensile resistance lost due to corrosion damage.

As shown in **Figure 5.7**, the incorporation of GFRP bars produces a substantial contribution to the moment capacity at pure bending, with 25GFRP60 increasing by 32% at 25% corrosion and 50GFRP60 increasing by 34% at 50% corrosion respectively, relative to the reference cases strengthened with unreinforced plain concrete cover of 60MPa (25STPC60 and 50STPC60).

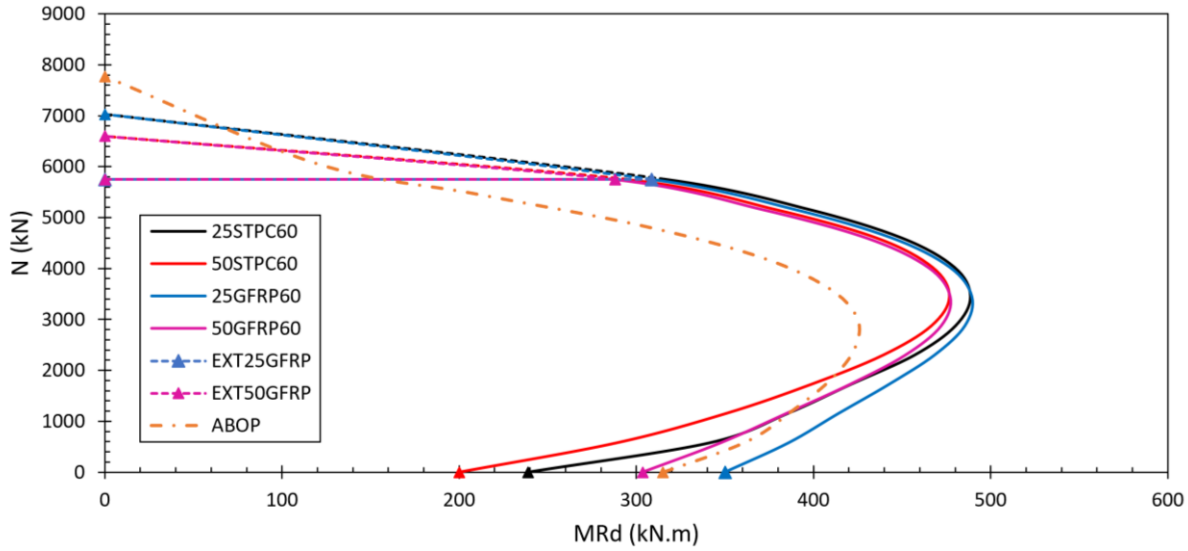


Figure 5.7: N-M interaction comparison of the plain C60 cover repair with and without longitudinal GFRP bar reinforcement, at 25% and 50% corrosion level.

The improvement is more pronounced at lower axial loads, where tensile reinforcement plays a dominant role. The 50GFRP60 case, despite having a lower bending moment capacity than the as-built case (ABOP), its percentage increase in bending moment capacity relative to the unreinforced plain concrete configuration at 50% corrosion level is much higher than the case at 25% corrosion level (25GFRP60). This is because the GFRP bars are able to compensate more for the lost cross-sectional area of the longitudinal reinforcement and weakened tension zone at higher levels of corrosion while only supplementing the steel contribution at lower corrosion damage. At intermediate axial loads, the combination of high-strength concrete and the elastic tensile reinforcement, produces a more resilient section capable of sustaining higher moments before reaching the balanced condition. The balanced region therefore shifts outward, indicating that the section can mobilize higher tensile and compressive forces simultaneously, leading to a slight improvement in the moment capacity in the balanced zone compared to the cases where only plain concrete cover strengthening was used at different corrosion levels. Although GFRP does not contribute directly to axial compression, the restored cover area increases axial resistance, and the axial capacity improvements are similar to those observed for plain concrete strengthening with small contribution to the compression dominated regime. Overall, GFRP strengthening offers a superior enhancement of flexural performance compared to plain concrete and SFRC strengthening, making it particularly effective for restoring bending capacity in deteriorated piles.

5.2.6. Effect of FRP Confinement on the Strengthened Deteriorated Pile

The primary benefit of CFRP confinement is in its ability to restore and significantly enhance the compressive behaviour of the concrete. Unlike strengthening methods which had moderate to high contributions in the tension zone, confinement improves significantly the stiffness, strength, and ductility of the compression zone, allowing the section to sustain higher compressive stresses before reaching its ultimate strain. The confined sections (CPC35 and CPC60), with the same cross-sectional geometry as the unconfined repaired sections (UPC35 and UPC60) examined earlier in this chapter, were analysed based on the Design Oriented FRP-confined reinforced concrete model introduced in Section 3.4 of Chapter 3, where 2 layers of FRP wrapping were selected on the basis that best satisfied a strengthening-ratio criterion consistent with rule of thumb specifying 40-50% threshold increase in structural capacity relative to the existing capacity, thereby avoiding both under and over-strengthening. As shown in **Figure 5.8** and **Figure 5.9**, the strengthening configurations incorporating CFRP confinement exhibit the most pronounced improvement in overall sectional performance among all repair strategies considered. The corresponding interaction diagrams for the confined specimens (UPC35 vs. CPC35 and UPC60 vs. CPC60 at both 25% and 50% corrosion levels) show a clear outward expansion of the N-M envelopes, reflecting the improved compressive behaviour of the confined concrete.

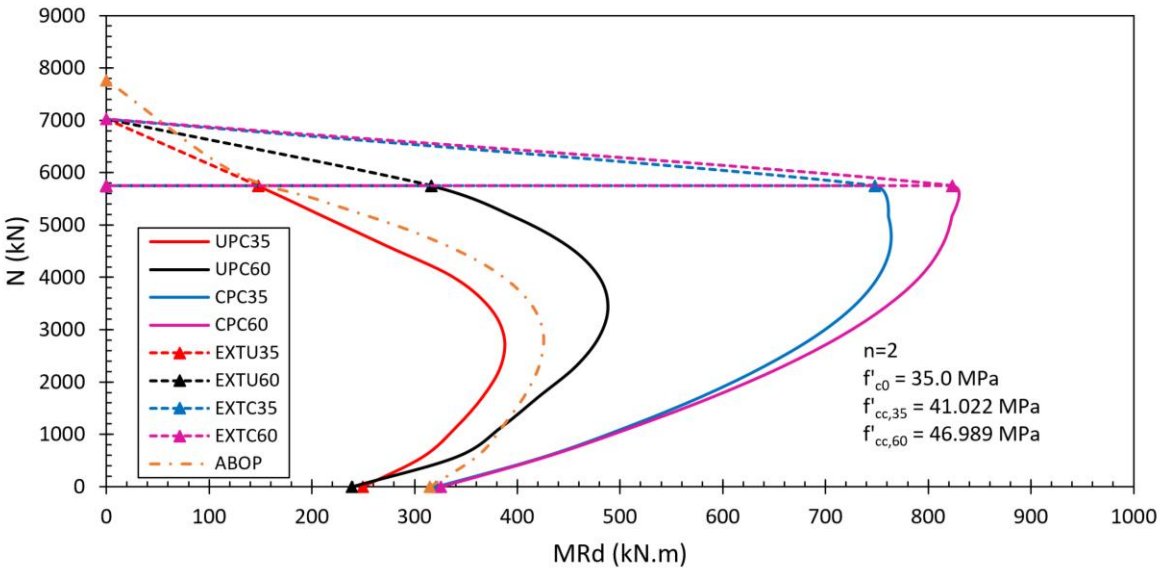


Figure 5.8: N-M interaction diagram of unconfined (UPC35, UPC60) and FRP-confined (CPC35, CPC60) repaired sections at 25% corrosion level.

A direct comparison between the unconfined pile sections (UPC35 and UPC60) and the confined pile sections (CPC35 and CPC60) at 25% corrosion illustrates the magnitude of this improvement. The confined sections exhibit an increase in combined axial-moment capacity by 49% and 41%, respectively, particularly pronounced in the compression-controlled region, where confinement directly strengthens the compression zone, and in the balanced region, where the section benefits from both improved compressive strength and increased ultimate strain. The tension-controlled region also shows improvement, though to a lesser extent, because confinement indirectly enhances bending capacity by stabilizing the compression zone rather than contributing directly to tensile resistance. Despite the confined strengthened section CPC60 producing the highest increase in moment capacity, its percentage increase in moment capacity relative to the unconfined sections UPC60 is slightly lower than CPC35 with 35MPa strength; because the unconfined concrete of 60 MPa already possesses a higher baseline strength, therefore significant contributions are made to the lower concrete grade of 35MPa.

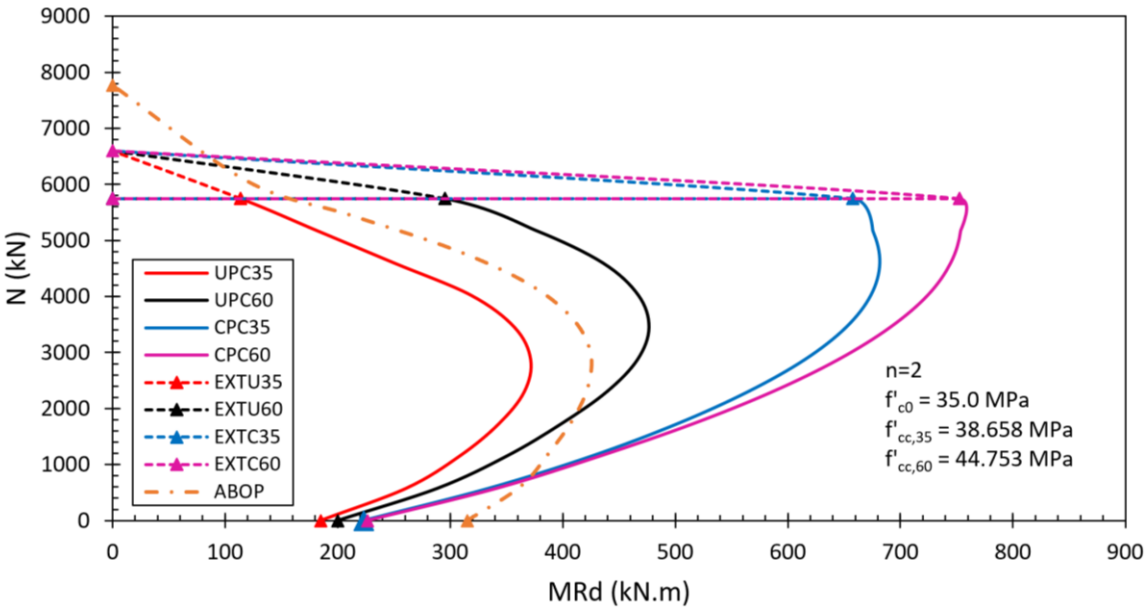


Figure 5.9: N-M interaction comparison of unconfined (UPC35, UPC60) and FRP-confined (CPC35, CPC60) repaired sections at 50% corrosion level.

At 50% corrosion, where deterioration is more severe, confinement becomes even more critical. The CFRP jacket stabilizes the weakened cover, enhances the residual core strength, and mitigates the brittleness associated with chronic steel corrosion. Notably, the confined sections (CPC35 and CPC60) exhibited an increase in combined axial-moment capacity by 45%

and 37%, respectively, relative to the reference unconfined sections (UPC35 and UPC60). The increase in moment capacity of the confined sections at pure bending is only significant relative to the unconfined strengthened cases (UPC35 and UPC60), but remained much lower than the as-built case (ABOP), as most of the existing longitudinal steel was severely degraded at 50% corrosion (see **Figure 5.9**). Although the absolute capacity at 50% corrosion remains lower than at 25%, the overall proportional benefit of confinement remains significant, demonstrating that CFRP strengthening is still effective in heavily deteriorated sections where compressive degradation is pronounced.

5.2.7. Strengthening with SHCC

As presented in Chapter 3 (Section 3.3.3), SHCC strengthening produces substantial improvements in flexural capacity due to its sustained post-crack tensile hardening behaviour. Rather than localizing into a single crack after first cracking, SHCC develops multiple parallel micro-cracks and maintains rising tensile stresses over large strain ranges. This behaviour allows the section to sustain significantly higher bending moments. This pseudo-strain-hardening response allows the tension zone to remain effective over large curvature demands, producing substantial gains in bending resistance. **Figure 5.10** and **Figure 5.11** compare the SHCC-strengthened section (SHCC35) with the plain-concrete repairs STPC35 and STPC60 at 25% and 50% corrosion, respectively.

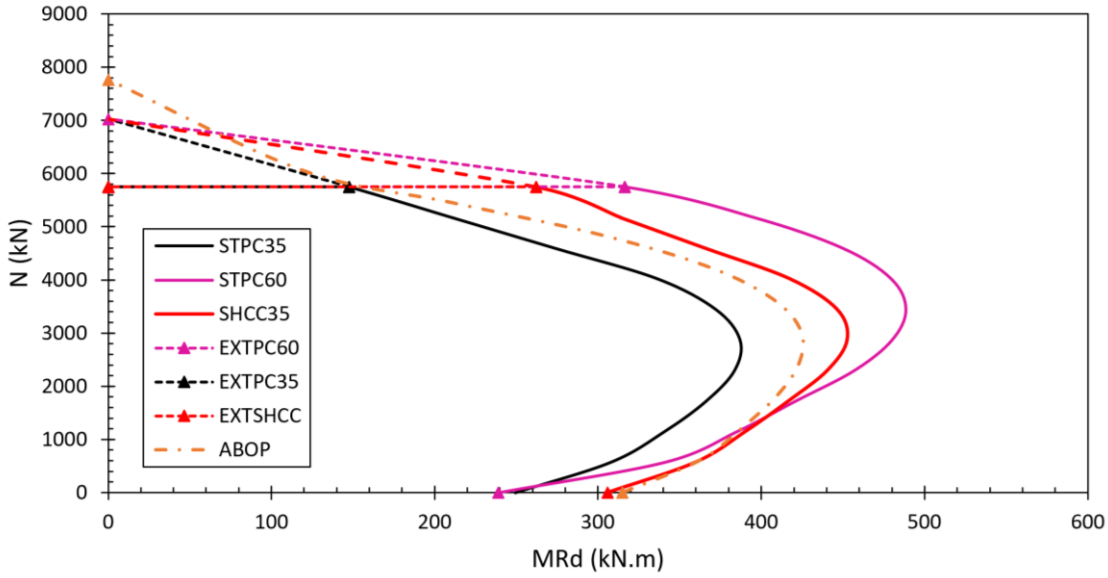


Figure 5.10: N-M interaction comparison of the SHCC-strengthened section (SHCC35) with the plain-concrete repairs STPC35 and STPC60, at 25% corrosion level.

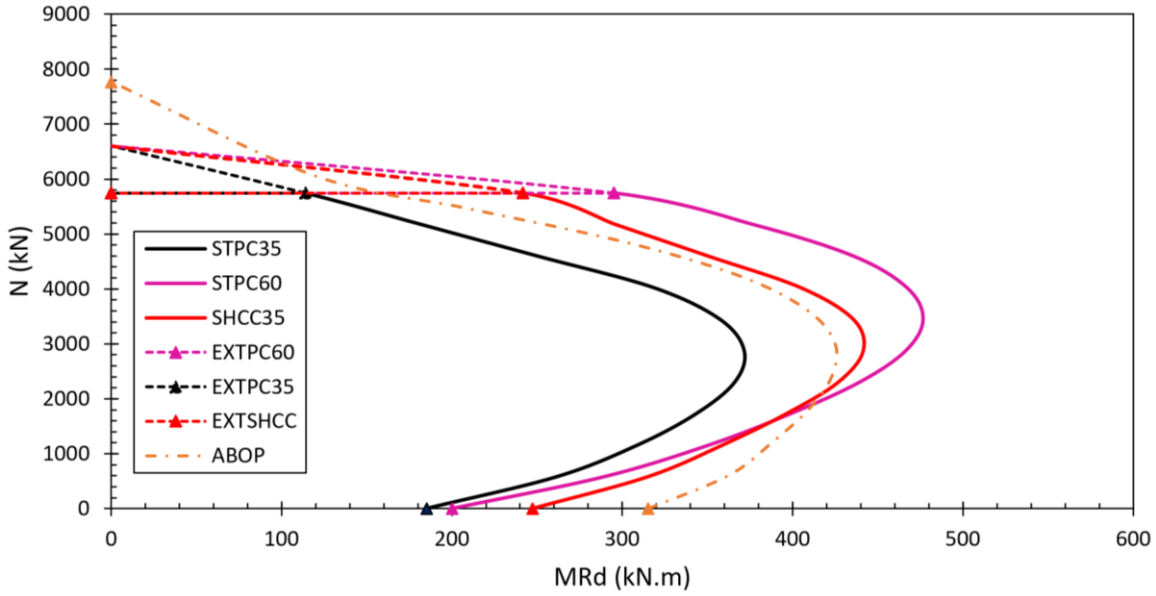


Figure 5.11: N-M interaction comparison of the SHCC-strengthened section (SHCC35) with the plain-concrete repairs STPC35 and STPC60, at 50% corrosion level.

In pure bending, SHCC outperforms both plain-concrete configurations (PC35 and PC60) at both corrosion levels, despite using the lower-grade 35 MPa matrix. At 25% corrosion its moment capacity of 305 kN·m exceeds STPC35 with 249 kN.m and STPC60 with 238 kN.m. At 50%, SHCC reaches 247 kN·m, against 185 kN·m for STPC35 and 200 kN·m for STPC60, a significant increase in moment capacity by about 35% and 25%, respectively. The much larger relative advantage over STPC35 at the higher corrosion level follows the same mechanism already noted for SFRC in Section 5.2.3, where the prestressing steel's own contribution to the tension zone decreases with increasing corrosion, the multiple-cracking tensile contribution of the SHCC matrix makes up a progressively larger share of the total tensile resistance, so the strengthened section becomes comparatively less dependent on the condition of the original reinforcement. The moment capacity of the SHCC strengthened section in pure bending, however, remained well below that of the as-built case (ABOP) at both levels of corrosion, attributed to the lost tensile capacity due to reduction in the cross-sectional area of the existing longitudinal steel relative to the as-built case (see **Figure 5.10** and **Figure 5.11**).

The benefits of SHCC are concentrated in the tension-controlled region of the interaction diagram, however, and do not extend to the balanced and compression-controlled regions of the N-M interaction diagrams. As shown in **Figure 5.10** and **Figure 5.11**, the axial capacity improvements are moderate compared to STPC60. At the balanced point, SHCC35 reaches a peak moment of 452 kN·m at 25% corrosion and 441 kN·m at 50% corrosion. This exceeds

STPC35 but falls short of STPC60 by roughly 7-8% at both corrosion levels. This reflects the modest increase in compressive strength provided by SHCC.

Compared with the GFRP-reinforced cover discussed in Section 5.2.4, SHCC strengthening is the more superior only to the unreinforced strengthening configurations. It's pure-bending capacity of 305 kN.m at 25% corrosion and 247 kN.m at 50% corrosion remains below that of the GFRP-reinforced PC60 cover with 350 kN·m and 303 kN·m, respectively, a shortfall of roughly 14% at 25% corrosion and 23% at 50% corrosion. The distinction lies in the reinforcing mechanism, where GFRP bars add a discrete, high-strength tensile force at a fixed location within the cover, whereas SHCC's benefit comes from keeping a distributed, cracked tension zone stiff and effective over a large strain range. The latter is a more modest contribution to the flexural capacity but a substantially more valuable contribution to ductility, crack width control, and post-cracking durability, none of which is captured directly by the N-M envelope.

Overall, SHCC strengthening offers a genuine and consistent improvement in pure-bending capacity over plain-concrete cover repair at both corrosion levels, with the improvement becoming proportionally larger as corrosion severity increases. It does not match the peak axial compressive moment capacity of a higher-grade plain-concrete cover at the balanced point, nor the pure-bending capacity achieved with GFRP bar reinforcement, but its combination of a moderate strength gain with substantially enhanced tensile ductility makes it a valuable strengthening option where crack control and post-cracking resilience in regions where curvature demands are high.

5.3. Shear Capacity Assessment

Assessment of shear resistance for marine piles is critical for significant lateral demands that may arise from seismic action, wave action, and geotechnical hazards. This section discusses the shear capacity predictions obtained from the analytical model developed in Chapter 4, applied to the representative strengthened pile sections and summarized in the results in **Table 4.4**. The discussion presents the results from the analysis considering: the influence of corrosion level and reinforcement location (longitudinal, transverse, or combined), the influence of axial load, the influence of the cover material and transverse reinforcement type, and the resulting implications for the selection of a shear strengthening strategy.

5.3.1. Influence of Corrosion damage

As shown in **Table 4.4** of Chapter, the effect of corrosion on the existing longitudinal steel had the least impact on total predicted shear capacity of the strengthened sections, compared to other configurations where the effect of corrosion was applied to only the existing transverse reinforcement or both longitudinal and transverse reinforcement at the same time. At zero axial load, the reference configuration (plain C60 cover with new steel bars and hoops) predicts $V_{Rd} = 360$ kN for 25% longitudinal corrosion (25LS) and 351 kN for 50% longitudinal corrosion (50LS), a reduction of only 2.4% for a doubling corrosion level applied to the existing longitudinal steel. Corrosion of the existing transverse spiral reinforcement, on the other hand, has a substantially larger effect such that: 25% and 50% transverse corrosion (25TS, 50TS) reduce V_{Rd} to 345 kN and 323 kN, respectively, a 4.1% reduction at 25% corrosion and 10.2% reduction at 50% corrosion relative to the longitudinally corroded case (25LS and 50LS), respectively. The combined longitudinal-and-transverse corrosion cases (25LTS, 50LTS) produce the largest reductions, at 338 kN and 307 kN respectively, with a 14.6% reduction in shear capacity at 50% combined corrosion relative to 25% corrosion on only the longitudinal bars (25LS), which indicates that the effect of the two corrosion degradation mechanisms on the shear capacity of the cross-sections is more severe in a combined damage configuration than independently damaged configurations. Longitudinal steel loss only affects the concrete term $V_{Rd,e}$, through the reinforcement ratio while transverse steel loss affects both $V_{Rd,e}$, through the effective width, and the stirrup term $V_{Rd,s}$ directly. It is further observed that this corrosion sensitivity applies only to $V_{Rd,e}$, as the strengthening-domain term $V_{Rd,s}$ remained unchanged across every corrosion level and reinforcement combination for a given cover configuration and axial load level. This is because the strengthening domain is entirely new, with undamaged reinforcement in the repaired cover. This is consistent with the logic of the proposed analytical model, where deterioration of the old core does not affect the shear resistance of the new strengthening layer. This observed corrosion sensitivity was consistent in all four configurations examined. Comparing the most favourable (25% longitudinal only) and least favourable (50% combined longitudinal-and-transverse) corrosion cases at $N_{Sd} = 0$, total resistance falls by 14.6% for steel bars/hoops, 18.8% for GFRP bars/hoops, 17.3% for SFRC without discrete hoops, and 16.1% for SFRC with discrete hoops. At $N_{Sd} = 0.6N_{Rd}$, the same comparison in the predicted shear capacity showed a consistent pattern with reductions

of 5.7%, 6.2%, 6.5% and 8.1% in all the four strengthening configurations; PC60 + steel bars/hoops, PC60 + GFRP bars/hoops, SFRC (3c/60) + GFRP without hoops and SFRC (3c/60) + GFRP with hoops, respectively.

5.3.2. Influence of Axial load on the predicted shear capacity

The influence of axial load on shear capacity is very substantial, and considerably larger in absolute and relative terms than the influence of corrosion. For the reference steel-hoop configuration, increasing the axial load from N_{Sd} = 0 to N_{Sd} = 0.6N_{Rd} increases the existing-core term $V_{Rd,e}$ from approximately 157 kN to 523 kN at 25% longitudinal corrosion, and increases the strengthening-domain term $V_{Rd,s}$ from 202 kN to 497 kN over the same range. The corresponding total shear resistance increases from 360 kN to 1,020 kN, an increase of 184%. This magnitude of enhancement reflects the combined implicit and explicit axial load channels established in Chapter 4: the implicit channel, through which increasing compressive axial load deepens the neutral axis and increases the effective shear depth $d_{l,eq}$ used in both the concrete and transverse reinforcement terms, and the explicit channel, through the direct axial compressive stress term entering the critical-shear-crack-theory concrete resistance equation. Fundamentally, as the section is axially compressed, the diagonal shear cracks tighten and close, thereby increasing the shear friction and the overall contribution of the aggregate interlock. The deepening of the neutral axis also increases the effective lever arm, resulting into a more favourable strut inclination accounted for through the transverse reinforcement term. The combination of these effects produces a substantial increase in the total shear resistance at N_{Sd} = 0.6N_{Rd}.

It was also observed that the influence of corrosion damage on the shear capacity of the pile section diminished with an increasing axial load in that: at N_{Sd} = 0, the combined longitudinal-and-transverse configuration with 50% damage (50LTS) reduces V_{Rd} by 14.6% relative to the 25% longitudinal-only case (25LS); while at N_{Sd} = 0.6N_{Rd}, the equivalent comparison (50LTS against 25LS) shows a reduction of only 5.7%. This behaviour follows directly from the growing dominance of the axial-load-driven component of both $V_{Rd,e}$ and $V_{Rd,s}$ as N_{Sd} increases: once the compressive stress field and the associated neutral-axis increased, the resistance contributed by this mechanism compensated for the comparatively modest reduction associated with reinforcement section loss. The practical implication is that piles carrying a

substantial permanent axial compressive loads remain less sensitive to reinforcement corrosion, retaining a proportional amount of their shear capacity as corrosion progresses than would be inferred from an assessment conducted at zero or low axial load; conversely, the zero axial load condition, is still more critical one for shear design especially where lateral loads are considered, and should be treated as the more corrosion-sensitive and hence potentially governing shear design case.

The magnitude of the axial-load benefit varied noticeably for the different configurations, in the existing and strengthening domains, respectively. With reference to the case study of the pile sections at 25% corrosion on the existing longitudinal steel, the shear resistance of the existing domain ($V_{Rd,e}$) grows by almost exactly the same proportion in every configuration between N_{Sd} = 0 and N_{Sd} = 0.6N_{Rd}, from about +233% to +237%, as this term and its axial-load dependence are shared by all four configurations and are not affected by the cover material. The strengthening-domain ($V_{Rd,s}$), on the other hand, grows very differently depending on the reinforcement mechanism as: 146% for steel hoops in PC, 236% for GFRP hoops in PC, 158% for SFRC without discrete hoops, and by only 16% for SFRC with discrete hoops. As a result, total capacity increases by 184% for steel hoops in PC, 235% for GFRP hoops in PC, 199% for SFRC without hoops, and only 124% for SFRC with hoops, over the same axial load range.

5.3.3. Influence of Cover Material and Transverse Reinforcement Type

Comparing the four cover-reinforcement configurations at N = 0 and 25% longitudinal corrosion, the total predicted shear resistance ranks as follows: plain concrete with steel hoops (360 kN) > SFRC with discrete GFRP (319 kN) > SFRC without discrete GFRP hoops (296 kN) > plain concrete with GFRP hoops and bars (277 kN). At N = 0.6N_{Ed}, the same four configurations rank as: steel hoops and bars in PC (1,020 kN) > GFRP bars and hoops in PC (928 kN) > SFRC without discrete hoops (886 kN) > SFRC with discrete hoops (713 kN).

Two key observations were made; first, the GFRP reinforced SFRC strengthening configurations predicted a lower shear resistance at 0.6N_{Ed}, relative to the PC strengthening configurations the GFRP reinforced PC configurations, which is not the case at zero axial load condition (N = 0). This is because at zero axial load, the SFRC cover provides a distinct advantage, in that the steel fibres actively bridge opening cracks, supplementing aggregate

interlock through a dedicated post-cracking shear-transfer mechanism by the fibres in the concrete matrix, explicitly incorporated in the model through the residual tensile strengths of SFRC. Since the shear crack widths are larger at zero axial load, the fibre bridging mechanism is fully mobilized, and the SFRC strengthening contributes significantly to the concrete shear resistance, consequently outperforming plain-concrete, in all the configurations where both materials are reinforced with GFRP. However, at $0.6N_{Ed}$, axial compression reduces crack widths, tightening the critical shear crack, which greatly increases aggregate interlock and activates the confinement provided by the transverse reinforcement. Under these conditions, the model amplifies the concrete contribution through the axial-stress term, which becomes dominant. Because this axial-stress-driven enhancement is more pronounced in plain concrete than the fibre-driven mechanism in SFRC, which is particularly effective during crack opening, the relative advantage of SFRC diminishes as the fibres are no longer fully mobilized. This explains why, at $0.6N_{Ed}$, plain-concrete strengthened sections with GFRP reinforcement surpass the SFRC strengthened cases, contrary to the trend observed at zero axial load.

Second, the strengthening configuration comprising SFRC with transverse GFRP reinforcement outperformed the case without GFRP transverse reinforcement, particularly at zero axial lad. This demonstrates that the presence of transverse reinforcement increases the shear resistance of the reinforced concrete element. However, moving from N = 0 to $N = 0.6N_{Ed}$, a comparatively minor, axial-load sensitivity in the predicted shear resistance of its strengthening-domain term ($V_{Rd,s}$). $V_{Rd,s}$ increases from only 164 kN at N = 0 to 190 kN at $N = 0.6N_{Ed}$, an increase of just 16%, far smaller than the 146-236% increases observed for other configurations. Because this configuration combines the fibre matrix contribution and the discrete GFRP hoop contribution within a single Annex L Equation L.21 formulation rather than through direct superposition of the two mechanisms evaluated separately, its total resistance at N = 0 is overtaken by the GFRP-in-PC and SFRC-without-transverse-reinforcement configurations at high axial load, leaving it the lowest-performing configuration at $N = 0.6N_{Ed}$ despite combining two nominally beneficial mechanisms.

In general, the predicted shear resistance of the sections strengthened with steel hoops and bars was much higher than the sections strengthened with GFRP. This is because the flexural and shear stiffness of steel is much higher than that of GFRP, hence, the dowel action of the steel reinforcement is more effective than that of the GFRP reinforcement, resulting into a

high shear resistance than in GFRP strengthening configurations. Additionally, GFRP does not yield like steel, and bending of the GFRP hoops reduces their effective strength, thereby affecting the overall shear resistance of the GFRP strengthened sections relative to steel strengthened configurations.

5.3.4. Implications for shear strengthening strategy

The results discussed above lead to the following practical conclusions, relevant to the selection of a shear repair or strengthening strategy for a deteriorated marine prestressed pile of this type. First, restoring or providing new discrete transverse reinforcement (steel or GFRP hoops) in the strengthening cover is an effective and predictable strategy because the resulting strengthening-domain resistance is, by the two-domain model's own internal logic, immune to the corrosion state of the pre-existing core, so the designer can rely on the full undamaged capacity of the new hoop reinforcement regardless of the assessed corrosion level of the original pile. Second, where the governing shear demand occurs at low axial load, for example in lateral-dominated loading with limited concurrent axial compression, SFRC cover without discrete hoops is a competitive and comparatively simple strengthening option, as it slightly outperforms a sparse GFRP hoop layout in this regime. Third, where the governing shear demand occurs under substantial concurrent axial compression, which is the typical condition for an in-service foundation pile, discrete hoop reinforcement, in steel or GFRP, is preferable to a fibre-only SFRC cover, because the truss-type mechanism benefits far more from the axial-load-driven increase in effective shear depth than the fibre-bridging mechanism does. Fourth, the combined SFRC-with-GFRP-hoops configuration should not be assumed to provide the cumulative sum of its constituent benefits; as the model predicts a saturated, low axial-load-sensitivity response for this specific combination that leaves it under-performing simpler single-mechanism alternatives at high axial load, and this prediction should be further verified experimentally.

5.4. Summary

The strengthening strategies evaluated in this study demonstrate distinct and predictable patterns of structural improvement, each governed by the specific mechanical pathway

through which the intervention restores or enhances sectional behaviour. Although their effects differ in magnitude and in the regions of the N-M domain where they are most influential, the results collectively reveal a coherent hierarchy of effectiveness that is consistent across both 25% and 50% corrosion levels.

Plain concrete strengthening provides reliable geometric restoration by rebuilding the lost cover and restoring the compression block. Its effectiveness increases with concrete strength, with 60 MPa covers consistently outperforming 35 MPa covers. At 25% corrosion, plain concrete recovers a meaningful portion of the lost capacity, but at 50% corrosion its influence becomes more limited because it cannot compensate for the reduced steel area or shortened lever arm. Its role is therefore foundational but not transformative.

SFRC strengthening provides balanced improvements in bending resilience and crack control. Its post-crack residual tensile behaviour stabilizes the tension zone and enhances ductility, but the increase in peak bending capacity between lower and higher performance classes (3a to 8a) remains modest because the prestressing steel continues to dominate the tensile resistance. At 50% corrosion, where steel deterioration is more severe, SFRC's proportional benefit increases, making it a valuable strategy for improving bending performance and durability in more degraded sections.

GFRP bar strengthening enhances the tension zone and improves bending performance more effectively than plain concrete alone. The elastic behaviour of GFRP allows the section to sustain higher tensile strains without yielding, producing a more resilient bending response. At 25% corrosion, GFRP acts as supplementary reinforcement; at 50% corrosion, where the steel contribution is significantly diminished, its proportional benefit becomes more pronounced. Even so, its influence remains primarily flexural, with limited impact on axial resistance.

FRP confinement delivers the most comprehensive improvement in overall sectional performance. By enhancing the compressive strength, stiffness, and ultimate strain of both the cover and the core, confinement produces substantial gains in axial capacity and balanced moment capacity. The confined specimens consistently outperform their unconfined counterparts by 30-40% at 25% corrosion and often exceed 40% improvement at 50% corrosion, while remaining within the realistic strengthening bounds corresponding to 40-50% of the existing capacity. Confinement is therefore the most effective strategy for restoring

global capacity, particularly in heavily deteriorated sections where compressive degradation is severe.

SHCC strengthening produces a significant enhancement of pure-bending capacity, exceeding both plain-concrete cover options and SFRC at every corrosion level examined, with the relative benefit growing as corrosion severity increases. Its sustained tensile hardening behaviour keeps the tension zone effective over much larger curvature demands than a plain or steel-fibre-reinforced cover, though its peak flexural capacity at the balanced point remains below that of a higher-grade plain-concrete cover, and its pure-bending capacity remains below that achieved with GFRP bar reinforcement. Its principal value lies less in maximizing peak capacity than in the ductility, distributed cracking, and post-cracking resilience it provides, which are particularly relevant to the long-term durability of flexural-critical regions of deteriorated piles.

Overall, the results show that each strengthening strategy performs well in addressing specific capacity demands of the deteriorated pile sections. FRP confinement is the most effective for restoring axial and combined axial-moment capacity; GFRP bars provide the largest gain in pure-bending capacity; SHCC provides a substantial pure-bending improvement together with superior tensile ductility and crack control; SFRC offers balanced improvements in ductility and bending resilience; and plain concrete provides essential geometric restoration and remains the most effective route to compression-zone capacity short of confinement. The optimal strengthening solution therefore depends on the structural demands of the pile and the severity of deterioration, with the results of this study offering a clear and technically grounded basis for selecting the most appropriate intervention.

With respect to shear, the analytical model developed in Chapter 4 shows that the existing-core shear resistance deteriorates systematically with the influence of corrosion damage, degrading moderately in the configurations where corrosion affected only the existing longitudinal reinforcement, and more substantially when the damage affected both the transverse and longitudinal reinforcement in a combined configuration. The predicted shear resistance of the strengthening-domain remains essentially unaffected by the corrosion state of the pre-existing core, since it is generated governed entirely by the new, undamaged repair reinforcement. Across all strengthening configurations, the axial load exerted a far larger influence on shear capacity than corrosion, increasing the total resistance greatly between

the unloaded and service-loaded condition, and this axial-load sensitivity differs materially between various reinforcement types and shear transfer mechanisms. Under high axial compression, the dominant mechanisms are crack-closure, aggregate interlock, and confinement, which favour discrete transverse reinforcement, particularly steel hoops and, to a lesser extent, GFRP hoops. Steel's higher flexural and shear stiffness, superior dowel action, and ability to yield allow it to mobilize substantially greater shear resistance than GFRP, whose lower shear stiffness and bending-induced strength reduction limit its effectiveness. At low axial load, however, the cracks open and aggregate interlock reduced, distributed fibre bridging in SFRC becomes the primary shear-transfer mechanism in SFRC strengthened sections, outperforming the plain-concrete GFRP strengthened configurations, as the fibres actively bridge cracks and compensate for the lower dowel action of GFRP bars and hoops.

THIS PAGE WAS INTENTIONALLY LEFT BLANK

6. CONCLUSIONS AND FURTHER DEVELOPMENTS

This dissertation has developed and applied an integrated analytical framework for the flexural and shear capacity assessment of deteriorated and FRP/steel-repaired octagonal steel-prestressed concrete marine piles, using nine pile specimens extracted from the Earl C. Davis Memorial Bridge at Harkers Island, North Carolina, as the reference case study. This closing chapter draws together the main conclusions arising from the analytical developments of Chapters 3 and 4 and the case-study results and discussion of Chapter 5, and proposes further developments, in particular the experimental and finite element validation, considered necessary to confirm and extend the findings of this work.

6.1. Main Conclusions

6.1.1. Analytical Framework Developed

- A layered sectional analysis framework, implemented within the DOCROS software, was successfully applied to predict the axial load-moment (N-M) interaction response of the pile sections across its as-built, corrosion-deteriorated, and strengthened states, incorporating constitutive models for plain concrete, steel-fibre-reinforced concrete across six performance classes (3a, 3c, 3e, 6a, 8a, 8e), strain-hardening cementitious composites, reinforcing steel, GFRP bars, and FRP-confined reinforced concrete, the latter through the design-oriented dual-confinement model of Shayanfar et al. [36].
- An analytical shear model was formulated for circular strengthened RC sections, superposing the shear resistance of the existing deteriorated core and the new strengthening cover, each combining a critical-shear-crack-theory concrete term and a transverse-reinforcement term appropriate to the material present (steel or FRP hoops, or SFRC with or without discrete hoops), with the influence of axial load incorporated through both the implicit neutral-axis-depth channel and the explicit axial-stress channel. No equally general, physically consistent closed-form model of this kind was identified in the literature for the combined case of a circular,

deteriorated, and FRP/steel-strengthened section, providing a feasible research gap explored in this work.

Both frameworks were successfully applied to the full matrix of configurations relevant to the Harkers Island case study: two corrosion levels (25% and 50% cross-sectional loss), applied individually or in combination to the longitudinal and transverse reinforcement; and multiple cover and strengthening options (plain concrete at two grades, six SFRC performance classes, GFRP bar reinforcement, and FRP/steel confinement), demonstrating that the proposed methodology is sufficiently general and computationally tractable for systematic, multi-variable structural assessment of this class of marine pile.

6.1.2. Flexural and Axial Capacity Predictions

- Marine deterioration reduces the flexural and axial capacity of the as-built pile substantially and non-uniformly: the reference axial compressive capacity fell by approximately 40-80% and the pure-bending moment capacity fell by approximately 31% at 25% corrosion and 49% at 50% corrosion, confirming that loss of the concrete cover and the cross-sectional area of the longitudinal reinforcement contribute to the loss in axial compressive capacity and flexural capacity of the pile section. Additionally, at service limit state conditions, the loss of prestressing force in the corroded steel strands directly leads to premature and uncontrolled concrete cracking, excessive deflections, and reduced structural stiffness
- Cover reconstruction with plain concrete recovers a meaningful share of the lost axial compressive capacity, with the balanced moment capacity increasing by 35-52% and the pure-bending moment capacity increasing by 9-20% relative to the unrepaired deteriorated section, and with the higher-grade (C60) cover consistently outperforming the lower-grade (C35) cover, particularly in the compression-controlled region of the interaction diagram.
- SFRC cover repair provides a balanced enhancement of bending resilience and ductility rather than a large increase in peak flexural capacity, with the highest-performance class (8e) consistently producing the largest pure-bending enhancement, and with the proportional benefit of fibre reinforcement increasing, rather than decreasing, as

corrosion severity increases, since the fibre crack-bridging mechanism becomes proportionally more important to the tension zone as the prestressing steel area is lost.

- GFRP longitudinal bar reinforcement in the repaired cover produces a substantial, corrosion-level-dependent enhancement of pure-bending capacity, of the order of 32% at 25% corrosion and 34% at 50% corrosion, concentrated in the tension-controlled region of the interaction diagram, with limited direct contribution to axial or balanced-point capacity.
- CFRP confinement of the core and cover provides the most comprehensive capacity restoration of all strategies assessed, increasing combined axial-moment capacity by up to 49% relative to the unconfined repaired section at 25% corrosion and by up to 45% at 50% corrosion, and is the only strategy examined that materially expands the compression-controlled branch of the interaction envelope, making it the preferred strategy wherever the pile is subject to substantial concurrent axial compression.
- SHCC cover repair produces significant gain in pure bending capacity, exceeding both plain-concrete cover and SFRC options at every corrosion level examined. However, it falls short of the higher-grade plain-concrete cover (STPC60) at the balanced point by 7-8%, and remains below the pure-bending capacity achieved with GFRP bar reinforcement, positioning it as a ductility and durability-oriented strengthening options.

6.1.3. Shear Capacity Predictions

- Existing-core shear resistance is more sensitive to corrosion of the transverse (spiral) reinforcement than to corrosion of the longitudinal reinforcement, because transverse steel loss simultaneously reduces the truss-model stirrup term and the effective width of the concrete term, whereas longitudinal steel loss affects only the concrete term through the reinforcement ratio; field condition assessment intended to support shear-critical repair decisions should accordingly prioritize transverse reinforcement condition.

- The shear resistance contributed by the new strengthening in the cover is, by construction and as confirmed numerically across all configurations examined, insensitive to the corrosion state of the pre-existing core, since it derives entirely from undamaged new reinforcement; this cleanly validates the internal consistency of the two-domain superposition philosophy adopted for the proposed model.
- Between 0% to 60% of the applied axial load, the axial load exerts a substantially larger influence on total shear capacity than corrosion does, increasing total shear resistance substantially between $N_{Sd} = 0$ and $N_{Sd} = 0.6N_{Sd}$, and this sensitivity is itself dependent on the transverse reinforcement mechanism, with the presence of discrete steel or GFRP hoops benefiting far more from increasing axial load than in the case for distributed SFRC fibre bridging without transverse reinforcement.
- The behaviour of the different shear-strengthening configurations varies strongly with the axial load. At zero axial load, the SFRC cover benefits from fibre bridging and therefore outperforms plain-concrete GFRP configurations. Adding sparse GFRP hoops provides a modest additional gain in shear resistance but does not alter the fibre-dominated mechanism. Under high axial compression, however, crack-closure and confinement become the governing mechanisms, favouring the resistance of the aggregate interlock over the fibre bridging mechanism, while the discrete transverse reinforcement enhances dowel action of the longitudinal reinforcement. Therefore, GFRP reinforced plain concrete outperforms the SFRC configurations. The hybrid combined SFRC-with-GFRP-hoops system shows an unexpectedly muted axial-load sensitivity in that the fibre-driven mechanisms diminish as cracks tighten, while GFRP hoops offer limited confinement due to their lower shear stiffness and bending-induced strength reduction. This leaves the hybrid system as the lowest-performing configuration at high axial load, a model-based trend requiring experimental verification rather than a definitive design conclusion.

6.1.4. Repair Selection Strategy

Combining the flexural and shear findings above, the results of this dissertation support a load-demand-dependent hierarchy of repair strategy selection for deteriorated marine

prestressed concrete piles of this geometry and construction type. Where the governing demand is predominantly axial with low lateral (flexural and shear) demand, cover reconstruction with plain concrete, at the highest practicable grade, provides adequate and cost-effective capacity restoration. Where meaningful lateral demand is present at low-to-moderate axial load, SFRC or GFRP-reinforced cover options provide a materially larger flexural capacity than plain concrete alone, with the choice between the two guided by non-structural considerations such as constructability and long-term durability. Where the pile must sustain significant axial compression together with lateral demand, whether from wave action, vessel impact, or seismic loading, FRP or steel confinement of the core is indispensable, since it is the only strategy examined that materially expands both the flexural compression-controlled branch and, through discrete hoop reinforcement, the axial-load-dependent shear resistance of the section. In all cases, restoration or provision of new discrete transverse reinforcement in the repaired cover should be regarded as a reliable and corrosion-independent contribution to shear capacity, largely decoupled from the condition of the pre-existing core.

6.2. Further Developments

While the analytical frameworks developed in this dissertation are internally consistent, grounded in established mechanics, and applied systematically to a realistic and practically significant case study, they remain, at this stage, unvalidated against direct physical measurement on the specific pile geometry, material combinations, and damage states considered. The following developments are identified as relevant for future work, broadly grouped into experimental validation, numerical (finite element) validation, and further analytical refinement.

6.2.1. Experimental Validation

The most direct and valuable extension of this work is a program of physical testing on the nine extracted Harkers Island pile specimens, or on companion specimens fabricated to match their geometry and material properties, designed specifically to validate the analytical predictions of Chapters 3, 4 and 5. The following experimental activities are recommended:

- Combined axial-flexural (eccentric compression) testing of representative pile segments in the as-built, artificially or naturally corrosion-deteriorated, and repaired/strengthened conditions, instrumented to capture the full moment-curvature response and the axial load-moment interaction envelope, in order to validate the DOCROS-based flexural predictions of Chapter 3 and the comparative repair-strategy results of Chapter 5 directly against measured capacity, stiffness, and failure mode.
- Shear-critical testing of short pile segments, using a shear span-to-depth ratio in the range identified as critical for this section, for each of the strengthening configurations examined in Chapter 4, at varying axial loads, in order to validate the proposed analytical shear model directly, including the relative contribution of the existing and strengthening domains, and the axial-load sensitivity of each transverse reinforcement mechanism.
- Material characterization testing of the corroded prestressing strands recovered from the most severely deteriorated pile specimens, including residual tensile strength, ductility, and stress-strain response, to verify or refine the assumptions, adopted in this dissertation, that the corroded strand retains an as-built constitutive response at the assessed damage levels, an assumption expected to become progressively less conservative as the corrosion level increases beyond those explicitly modelled here.

6.2.2. Finite Element Validation

Complementary to physical testing, nonlinear finite element modelling, using an appropriate concrete damaged plasticity or smeared-crack constitutive formulation, is recommended as an intermediate validation step, both to cross-check the analytical predictions prior to the availability of experimental data and to extend the parametric coverage of the assessment beyond what is practically achievable through physical testing alone. The following finite element activities are recommended:

- Development and validation of a three-dimensional finite element model of the octagonal and circular pile section, incorporating the discrete longitudinal prestressing strand and spiral reinforcement, the repaired cover and any GFRP or SFRC

reinforcement, and, where applicable, an externally bonded FRP jacket or steel confinement system, in order to verify the flexural (N-M interaction) predictions of Chapter 5 for the repair configurations considered.

- Development of a finite element model specifically configured for shear-critical response, using a shear span critically consistent with the pile sections evaluated in Chapter 4, with displacement-controlled loading and a mesh strategy sufficiently refined to capture diagonal shear cracking, in order to verify the analytical shear model proposed in Chapter 4, and in particular to resolve, ahead of or in parallel with physical testing, the physical mechanism underlying the anomalous axial-load sensitivity predicted for the combined SFRC-with-discrete-hoops configuration identified in Chapter 5.
- Use of the validated finite element model to extend the parametric assessment beyond the specific corrosion levels, axial load levels, and reinforcement configurations examined analytically in this dissertation, including intermediate corrosion levels, non-uniform (localized) corrosion patterns more representative of real tidal-zone pitting, and combined flexure-shear-axial load paths representative of lateral wave or vessel impact loading, which could not be addressed within the scope of the present sectional and truss-model-based analytical framework.

6.2.3. Further Analytical Refinement

Beyond experimental and numerical validation, several specific refinements to the analytical framework itself are identified as valuable extensions of this work:

- Incorporation of an explicit corrosion-dependent constitutive model for the prestressing steel at extensive damage levels, capturing the reduction in uniform elongation and ductility associated with uniform or pitting corrosion, to extend the validity of the flexural and shear predictions beyond the moderate damage levels (up to 50% cross-sectional loss) explicitly assessed in this dissertation.
- Explicit modelling of bond-slip behaviour at the interfaces between the existing core, the new cover material, and any externally bonded FRP or GFRP reinforcement, relaxing the perfect-bond assumption adopted throughout this work, since imperfect

bond is expected to reduce the effectiveness of the SFRC and GFRP cover-based strengthening strategies more than that of the FRP confinement jacket, as discussed in Chapter 5, and this effect could not be quantified within the present layered sectional and truss-model formulations.

6.2.4. Cost Assessment and Life Cycle Analysis

The use of strengthening solutions adopted during the service life of the deteriorated structures is mainly because they not only increase and restore the structural capacity of the existing structure, but are also less costly and less disruptive compared to total replacement. This has been discussed briefly in this work without substantial quantification. Therefore, future extensions of this work should explore a combined cost and life-cycle assessment (LCA) to compare the cost of materials, labour, logistics and other miscellaneous factors considered in the installation of the different strengthening techniques explored in this work, particularly in underwater conditions, and the environmental costs relating to carbon and resource consumption in repair considerations against full pile replacement. This can be normalized with respect to the restored structural capacity and the extended service life of the structure.

In summary, this dissertation has demonstrated that a physically based, layered sectional and shear analytical framework can provide a consistent, comparative, and practically actionable basis for the structural assessment and repair strategy selection of deteriorated marine prestressed concrete piles, using the Earl C. Davis Memorial Bridge piles at Harkers Island as a representative case study. The experimental and finite element validation program outlined above is identified as the necessary next step to confirm the quantitative predictions of this work and to extend its applicability with confidence to the wider population of ageing marine prestressed concrete piles that share the geometry, construction, and deterioration mechanisms examined in this dissertation.

REFERENCES

[1] C. R. Gagg, “Cement and concrete as an engineering material: An historic appraisal and case study analysis,” *Eng. Fail. Anal.*, vol. 40, pp. 114–140, May 2014, doi: 10.1016/j.engfailanal.2014.02.004.

[2] A. M. Neville, *Properties of concrete*, 5th Edition. Harlow Munich: Pearson, 2011.

[3] G. Jacobson, “NACE International’s IMPACT Breaks New Ground in the Study of Corrosion Management,” *Mater. Perform.*, vol. 55, no. 4, pp. 28–32, Apr. 2016, doi: 10.5006/MP2016_55_4-28.

[4] R. K. Varma, “Numerical models for the simulation of the cyclic behaviour of RC structures incorporating new advanced materials,” Tese de Doutoramento em Engenharia Estrutural, Universidade do Minho, Braga, Portugal, 2012.

[5] T. Carroll, A. Patel, and A. Ighwair, “Harkers Island Bridge Replacement: NCDOT’s First FRP-Reinforced Concrete Bridge,” *ASPIRE*, vol. Fall 2023, pp. 24–29.

[6] D. Ray, “Converging, if not merging,” Coastal Review. Accessed: Sep. 17, 2026. [Online]. Available: https://coastalreview.org/2023/10/converging-if-not-merging/

[7] R. Rodrigues, S. Gaboreau, J. Gance, I. Ignatiadis, and S. Betelu, “Reinforced concrete structures: A review of corrosion mechanisms and advances in electrical methods for corrosion monitoring,” *Constr. Build. Mater.*, vol. 269, p. 121240, Feb. 2021, doi: 10.1016/j.conbuildmat.2020.121240.

[8] L. Bertolini, B. Elsener, P. Pedeferri, E. Redaelli, and R. B. Polder, *Corrosion of Steel in Concrete: Prevention, Diagnosis, Repair*, 1st ed. Wiley, 2013. doi: 10.1002/9783527651696.

[9] F. Qu, W. Li, W. Dong, V. W. Y. Tam, and T. Yu, “Durability deterioration of concrete under marine environment from material to structure: A critical review,” *J. Build. Eng.*, vol. 35, p. 102074, Mar. 2021, doi: 10.1016/j.jobe.2020.102074.

[10] U. Angst, B. Elsener, C. K. Larsen, and Ø. Vennesland, “Critical chloride content in reinforced concrete — A review,” *Cem. Concr. Res.*, vol. 39, no. 12, pp. 1122–1138, Dec. 2009, doi: 10.1016/j.cemconres.2009.08.006.

[11] F. Qu, J. Zhang, G. Liu, and S. Zhao, “Experimental Study on Chloride Ion Diffusion in Concrete Affected by Exposure Conditions,” *Materials*, vol. 15, no. 8, p. 2917, Apr. 2022, doi: 10.3390/ma15082917.

[12] Y. Tian *et al.*, “Corrosion of steel rebar in concrete induced by chloride ions under natural environments,” *Constr. Build. Mater.*, vol. 369, p. 130504, Mar. 2023, doi: 10.1016/j.conbuildmat.2023.130504.

[13] R. K. Tipu, V. R. Panchal, and K. S. Pandya, “Enhancing chloride concentration prediction in marine concrete using conjugate gradient-optimized backpropagation neural network,” *Asian J. Civ. Eng.*, vol. 25, no. 1, pp. 637–656, Jan. 2024, doi: 10.1007/s42107-023-00801-3.

[14] *Report on corrosion of prestressing steels*. Farmington Hills, Mich.: American Concrete Institute, 2014.

[15] N. J. Carino, “Nondestructive Techniques to Investigate Corrosion Status in Concrete Structures,” *J. Perform. Constr. Facil.*, vol. 13, no. 3, pp. 96–106, Aug. 1999, doi: 10.1061/(ASCE)0887-3828(1999)13:3(96).

[16] S. Sharma, M. J. Osmolska, K. Hornbostel, L. Bathen, I. Novakova, and M. Geiker, “Repair Options for Corrosion-damaged Prestressed Concrete Bridges,” *Nord. Concr. Res.*, vol. 70, no. 1, pp. 99–123, Jun. 2024, doi: 10.2478/ncr-2024-0004.

[17] J. Y. Hu, S. S. Zhang, E. Chen, and W. G. Li, “A review on corrosion detection and protection of existing reinforced concrete (RC) structures,” *Constr. Build. Mater.*, vol. 325, p. 126718, Mar. 2022, doi: 10.1016/j.conbuildmat.2022.126718.

[18] P. Pfändler, L. Bircher, and U. Angst, “Inspecting the corrosion state of underground reinforced concrete structures,” *J. Infrastruct. Preserv. Resil.*, vol. 3, no. 1, p. 17, Dec. 2022, doi: 10.1186/s43065-022-00064-3.

[19] C. Andrade and C. Alonso, “Test methods for on-site corrosion rate measurement of steel reinforcement in concrete by means of the polarization resistance method,” *Mater. Struct.*, vol. 37, no. 9, pp. 623–643, Nov. 2004, doi: 10.1007/BF02483292.

[20] A. Zaki, H. Chai, D. Aggelis, and N. Alver, “Non-Destructive Evaluation for Corrosion Monitoring in Concrete: A Review and Capability of Acoustic Emission Technique,” *Sensors*, vol. 15, no. 8, pp. 19069–19101, Aug. 2015, doi: 10.3390/s150819069.

[21] G01 Committee, *Practice for Preparing, Cleaning, and Evaluating Corrosion Test Specimens*. doi: 10.1520/G0001-25.

[22] J. A. González, C. Andrade, C. Alonso, and S. Feliu, “Comparison of rates of general corrosion and maximum pitting penetration on concrete embedded steel reinforcement,” *Cem. Concr. Res.*, vol. 25, no. 2, pp. 257–264, Feb. 1995, doi: 10.1016/0008-8846(95)00006-2.

[23] T. Vidal, A. Castel, and R. François, “Analyzing crack width to predict corrosion in reinforced concrete,” *Cem. Concr. Res.*, vol. 34, no. 1, pp. 165–174, Jan. 2004, doi: 10.1016/S0008-8846(03)00246-1.

[24] N. Zhuang, H. Dong, Y. Zhou, and D. Chen, “Cracking behavior of reinforced concrete piles externally bonded with carbon fiber reinforced polymer in a marine environment,” *Constr. Build. Mater.*, vol. 190, pp. 1154–1162, Nov. 2018, doi: 10.1016/j.conbuildmat.2018.09.185.

[25] K. Andisheh, A. Scott, and A. Palermo, “Seismic Behavior of Corroded RC Bridges: Review and Research Gaps,” *Int. J. Corros.*, vol. 2016, pp. 1–22, 2016, doi: 10.1155/2016/3075184.

[26] X. Lin, P. Wang, S. Wang, and J. Shen, “Study on corrosion monitoring and assessment method of reinforced concrete based on multi-sensor fusion,” *Anti-Corros. Methods Mater.*, vol. 72, no. 2, pp. 279–291, Feb. 2025, doi: 10.1108/ACMM-10-2024-3121.

[27] R. Sen and G. Mullins, “Application of FRP composites for underwater piles repair,” *Compos. Part B Eng.*, vol. 38, no. 5–6, pp. 751–758, Jul. 2007, doi: 10.1016/j.compositesb.2006.07.011.

[28] V. M. Karbhari *et al.*, “Durability Gap Analysis for Fiber-Reinforced Polymer Composites in Civil Infrastructure,” *J. Compos. Constr.*, vol. 7, no. 3, pp. 238–247, Aug. 2003, doi: 10.1061/(ASCE)1090-0268(2003)7:3(238).

[29] G. Mullins, R. Sen, K. Suh, and D. Winters, “Underwater Fiber–Reinforced Polymers Repair of Prestressed Piles in the Allen Creek Bridge,” *J. Compos. Constr.*, vol. 9, no. 2, pp. 136–146, Apr. 2005, doi: 10.1061/(ASCE)1090-0268(2005)9:2(136).

[30] T. Triantafillou *et al.*, *fib Bulletin 14. Externally bonded FRP reinforcement for RC structures*. in fib Bulletins. fib. The International Federation for Structural Concrete, 2001. doi: 10.35789/fib.BULL.0014.

[31] J. B. Mander, M. J. N. Priestley, and R. Park, "Theoretical Stress-Strain Model for Confined Concrete," *J. Struct. Eng.*, vol. 114, no. 8, pp. 1804–1826, Sep. 1988, doi: 10.1061/(ASCE)0733-9445(1988)114:8(1804).

[32] L. Lam and J. G. Teng, "Design-oriented stress–strain model for FRP-confined concrete," *Constr. Build. Mater.*, vol. 17, no. 6–7, pp. 471–489, Sep. 2003, doi: 10.1016/S0950-0618(03)00045-X.

[33] *Guide for the design and construction of externally bonded FRP systems for strengthening concrete structures*. Farmington Hills, Mich.: American Concrete Institute, 2017.

[34] J. G. Teng, T. Jiang, L. Lam, and Y. Z. Luo, "Refinement of a Design-Oriented Stress–Strain Model for FRP-Confined Concrete," *J. Compos. Constr.*, vol. 13, no. 4, pp. 269–278, Aug. 2009, doi: 10.1061/(ASCE)CC.1943-5614.0000012.

[35] G. Lin, T. Yu, and J. G. Teng, "Design-Oriented Stress–Strain Model for Concrete under Combined FRP-Steel Confinement," *J. Compos. Constr.*, vol. 20, no. 4, p. 04015084, Aug. 2016, doi: 10.1061/(ASCE)CC.1943-5614.0000651.

[36] J. Shayanfar, J. A. O. Barros, and M. Rezazadeh, "Design-oriented stress–strain model for RC columns with dual FRP- steel confinement mechanism," *Compos. Struct.*, vol. 330, p. 117821, Feb. 2024, doi: 10.1016/j.compstruct.2023.117821.

[37] "FRP Application in Underwater Repair of Corroded Piles," in *SP-230: 7th International Symposium on Fiber-Reinforced (FRP) Polymer Reinforcement for Concrete Structures*, American Concrete Institute, 2005. doi: 10.14359/14885.

[38] J. Aguilar, D. Winters, R. Sen, G. Mullins, and M. Stokes, "Fiber-Reinforced Polymer Pile Repair Incorporating Cathodic Protection," *Transp. Res. Rec. J. Transp. Res. Board*, vol. 2150, no. 1, pp. 111–118, Jan. 2010, doi: 10.3141/2150-14.

[39] European Committee for Standardization, "Eurocode 2: Design of concrete structures – Part 1-1: General rules and rules for buildings," CEN, Brussels, Standard EN 1992-1-1:2004, 2004.

[40] K. R. Kordina, G. Mancini, K. Schäfer, A. Schieβl, K. Zilch, and fib. The International Federation for Structural Concrete, *fib Bulletin 54. Structural Concrete Textbook on behaviour, design and performance Second edition Volume 4*. in fib Bulletins. fib. The International Federation for Structural Concrete, 2010. doi: 10.35789/fib.BULL.0055.

[41] A. E. Naaman, Ed., *Proceedings of the Second International Workshop High Performance Fiber Reinforced Cement Composites: (HPFRCC2); Ann Arbor, USA, June, 11 - 14, 1995*, 1. ed. in High performance fiber reinforced cement composites, no. 2. London Weinheim: Spon, 1996.

[42] European Committee for Standardization, "Eurocode 2 - Design of concrete structures - Part 1-1: General rules and rules for buildings, bridges and civil engineering structures," no. EN 1992-1-1:2023. European Committee for Standardization (CEN), Brussels, Nov. 2023.

[43] European Committee for Standardization, "Test method for metallic fibre concrete — Measuring the flexural tensile strength (limit of proportionality (LOP), residual)," CEN, Brussels, Standard EN 14651:2005+A1:2007, 2007.

[44] V. C. Li, "On Engineered Cementitious Composites (ECC): A Review of the Material and Its Applications," *J. Adv. Concr. Technol.*, vol. 1, no. 3, pp. 215–230, 2003, doi: 10.3151/jact.1.215.

[45] V. C. Li and C. K. Y. Leung, “Steady-State and Multiple Cracking of Short Random Fiber Composites,” *J. Eng. Mech.*, vol. 118, no. 11, pp. 2246–2264, Nov. 1992, doi: 10.1061/(ASCE)0733-9399(1992)118:11(2246).

[46] Y. Yang, M. D. Lepech, E.-H. Yang, and V. C. Li, “Autogenous healing of engineered cementitious composites under wet–dry cycles,” *Cem. Concr. Res.*, vol. 39, no. 5, pp. 382–390, May 2009, doi: 10.1016/j.cemconres.2009.01.013.

[47] A01 Committee, *Specification for Steel Strand, Uncoated Seven-Wire for Prestressed Concrete*. doi: 10.1520/A0416_A0416M-12A.

[48] American Concrete Institute, *Guide for the design and construction of structural concrete reinforced with fiber-reinforced polymer (FRP) bars*, 1st printing. in ACI report, no. 440.1R–15. Farmington Hills, MI: American Concrete Institute, 2015.

[49] R. Eid, N. Roy, and P. Paultre, “Normal- and High-Strength Concrete Circular Elements Wrapped with FRP Composites,” *J. Compos. Constr.*, vol. 13, no. 2, pp. 113–124, Apr. 2009, doi: 10.1061/(ASCE)1090-0268(2009)13:2(113).

[50] J. B. Mander, M. J. N. Priestley, and R. Park, “Theoretical Stress-Strain Model for Confined Concrete,” *J. Struct. Eng.*, vol. 114, no. 8, pp. 1804–1826, Sep. 1988, doi: 10.1061/(ASCE)0733-9445(1988)114:8(1804).

[51] J. Shayanfar, J. A. O. Barros, and M. Rezazadeh, “Generalized Analysis-oriented model of FRP confined concrete circular columns,” *Compos. Struct.*, vol. 270, p. 114026, Aug. 2021, doi: 10.1016/j.compstruct.2021.114026.

[52] J. Turmo, G. Ramos, and A. C. Aparicio, “Shear truss analogy for concrete members of solid and hollow circular cross section,” *Eng. Struct.*, vol. 31, no. 2, pp. 455–465, Feb. 2009, doi: 10.1016/j.engstruct.2008.09.002.

[53] A. C. I. Committee, “Building code requirements for structural concrete (ACI 318-05) and commentary (ACI 318R-05),” American Concrete Institute, 2005.

[54] European Committee for Standardization, “Eurocode 2: Design of concrete structures - Part 1-1: General rules and rules for buildings,” no. EN 1992-1-1:2004. European Committee for Standardization (CEN), Brussels, Dec. 2004.

[55] J. L. Clarke and F. K. Birjandi, “The behaviour of reinforced concrete circular sections in shear,” *Struct. Eng.*, vol. 71, no. 5, pp. 73–81, Mar. 1993.

[56] J. Orr, A. P. Darby, T. Ibell, Denton, and J. Shave, “Shear design of circular concrete sections using the Eurocode 2 truss model,” Dec. 2010, doi: 10.17863/CAM.17020.

ANNEX I - DERIVATION OF THE COMPRESSION SEGMENT AREA AND CENTROID FOR A CIRCULAR SECTION

I.1 Area of Compression zone segment

The compression zone formed above the neutral axis in a circular cross-section corresponds to a circular segment, bounded by a chord and the arc of the circle. Consider a circular section of radius r, with the neutral axis or linear chord intersecting the section such that the compression zone subtends a central angle ω (in radians), as shown in **Figure I. 1**.

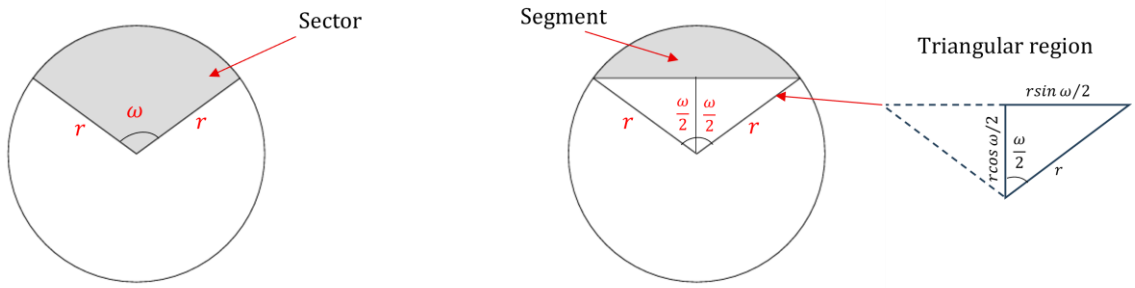


Figure I. 1: Geometrical representation of the compression zone

The area of this segment is obtained by decomposing it into two fundamental geometric components: a sector and an isosceles triangle. The difference between these two areas yields the exact area of the compression segment. Since the sector occupies a fraction of the area of the full circle, its geometrical area is therefore determined as:

$$A_{sector} = \frac{\omega}{2} r^2 \qquad \text{(I. 1)}$$

The second component is the triangle formed by the two radii enclosing the angle ω, and the chord that defines the neutral axis. As shown in **Figure I. 1**, for an isosceles triangle with two sides of length r, and an internal angle ω, its area can be expressed as:

$$A_{triangle} = \frac{1}{2} bh = 2\left(\frac{1}{2} r sin\frac{\omega}{2} . r cos\frac{\omega}{2}\right) \qquad \text{(I. 2)}$$

Substituting the trigonometrical identity for $\frac{sin\omega}{2} = sin\frac{\omega}{2}cos\frac{\omega}{2}$ in Eq. (I. 2) , the final formula for the area of the triangular region is calculated as:

$$A_{triangle} = \frac{1}{2}r^2 sin\omega \quad \text{(I. 3)}$$

Since the compression zone corresponds to the region of the sector excluding the triangle, therefore, the area of the compression zone is obtained by:

$$A_c = A_{sector} - A_{triangle} \quad \text{(I. 4)}$$

$$A_c = \frac{1}{2}r^2(\omega - sin\omega) \quad \text{(I. 5)}$$

I.2 Distance of the Centroid of the Segment from the Neutral Axis

For any given circle, the distance of the centroid of its segment ($\bar{y}$) measured from the centre of the circle is given as:

$$\bar{y} = \frac{4rsin^3\left(\frac{\omega}{2}\right)}{3(\omega - sin\omega)} \quad \text{(I. 6)}$$

where r is the radius of the circle, and ω is the internal angle. Considering the triangular region, the distance of the chord from the centre of the circle is expressed as:

$$y_{chord} = rcos\left(\frac{\omega}{2}\right) \quad \text{(I. 7)}$$

Considering the relationship between $\bar{y}$ and y_{chord}, as shown in **Figure I. 2**, the distance from the centroid of the compression segment to the chord (y_c) can be determined as:

$$y_c = \frac{4rsin^3\left(\frac{\omega}{2}\right)}{3(\omega - sin\omega)} - rcos\left(\frac{\omega}{2}\right) \quad \text{(I. 8)}$$

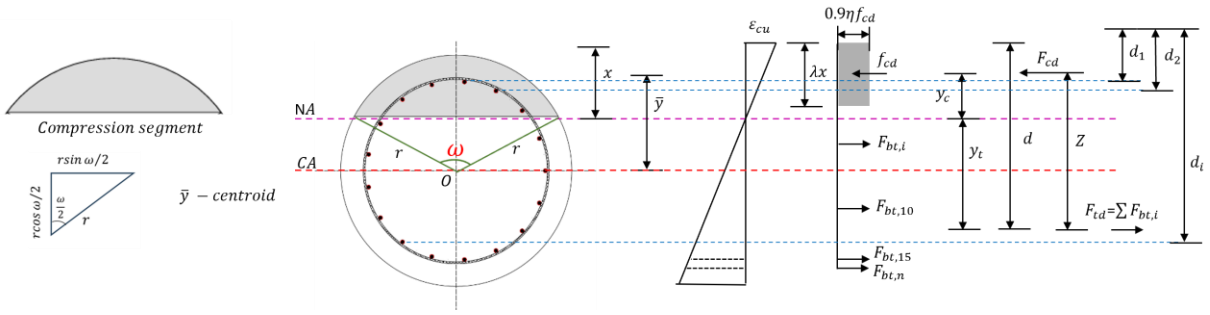


Figure I. 2: Geometrical relationship between the centroid of segment and the neutral axis

The depth of the neutral axis (x), measured from the extreme compression fiber at the top of the circle, is given by the geometric relation:

$$x = r\left(1 - cos\left(\frac{\omega}{2}\right)\right) \tag{I. 9}$$

such that;

$$cos\left(\frac{\omega}{2}\right) = 1 - \frac{x}{r} \tag{I. 10}$$

Substituting Eq. (I. 10) into Eq. (I. 8), with the radius (r) expressed as $r = \frac{D}{2}$, the distance of the centroid measured from the neutral axis can be calculated as:

$$y_c = \frac{2Dsin^3\left(\frac{\omega}{2}\right)}{3(\omega - sin\omega)} - \left(\frac{D}{2} - x\right) \tag{I. 11}$$

ANNEX II - DERIVATION OF THE AXIAL FORCE DISTRIBUTION BETWEEN THE EXISTING AND STRENGTHENING DOMAINS

Consider a composite section in which the applied axial force N_{Sd} is carried jointly by the existing core and the strengthening cover, as shown in **Figure II. 1**.

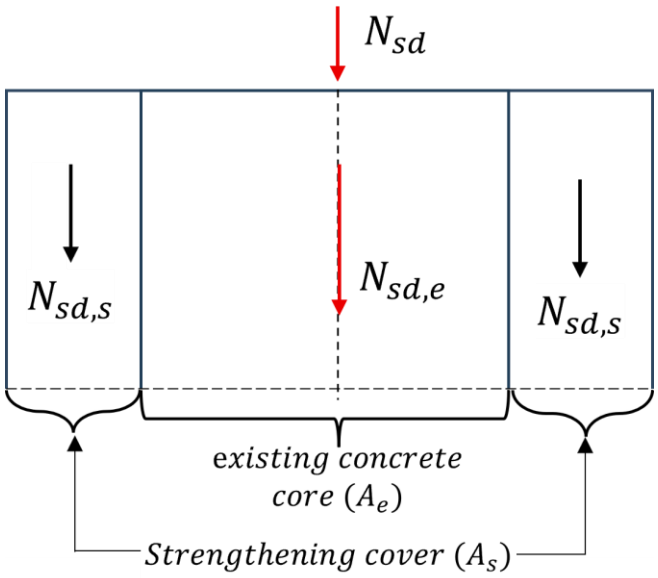


Figure II. 1: Axial load distribution in the strengthened pile section

The force equilibrium across the entire section is such that:

$$N_{Sd} = N_{Sd,e} + N_{Sd,s} \tag{II. 1}$$

where $N_{Sd,e}$ and $N_{Sd,s}$ is the axial load carried by the existing core and strengthening cover, respectively. Within the elastic range, the materials in each domain obey Hooke's law, such that:

$$\sigma = E\varepsilon \tag{II. 2}$$

where E and ε is the modulus of elasticity and strain of the material in each domain, respectively. But strain is itself defined physically as the elongation of a member divided by its original length,

$$\varepsilon = \frac{\mu}{L} \tag{II. 3}$$

where μ denotes the elongation of the domain under consideration, and L its original length.

Given that $\sigma = \frac{N}{A}$, combining the relationship between Eq. (II. 2) and Eq. (II. 3),

$$\frac{N}{A} = E.\frac{\mu}{L} \quad \Rightarrow \quad \mu = \frac{NL}{EA} \tag{II. 4}$$

Applying Eq. (II. 4) separately for each domain:

$$\mu_{c,e} = \frac{N_{Sd,e}L}{E_{c,e}A_{c,e}} \tag{II. 5}$$

$$\mu_{c,s} = \frac{N_{Sd,s}L}{E_{c,s}A_{c,s}} \tag{II. 6}$$

where $\mu_{c,e}$ and $\mu_{c,s}$ is the elongation of the existing and strengthening domain, respectively; $E_{c,e}$ and $E_{c,s}$ is the modulus of elasticity of the existing and strengthening domain, respectively; $A_{c,e}$ and $A_{c,s}$ is the cross-sectional area of the existing and strengthening domain, respectively.

By assuming perfect bond between the materials, the core and the strengthening cover are therefore bonded together and cannot elongate independently, a point at their shared interface must undergo the same physical displacement whether considered part of the core or part of the cover. This condition is expressed as:

$$\mu := \mu_{c,e} = \mu_{c,s} \tag{II. 7}$$

Equating the two expressions of Eq. (II. 5) and Eq. (II. 6) in accordance with Eq. (II. 7),

$$\frac{N_{Sd,e}L}{E_{c,e}A_{c,e}} = \frac{N_{Sd,s}L}{E_{c,s}A_{c,s}} \tag{II. 8}$$

Therefore:

$$N_{Sd,s} = \frac{E_{c,s}A_{c,s}}{E_{c,e}A_{c,e}} N_{Sd,e} \tag{II. 9}$$

Substituting Eq. (II. 9) into the equilibrium condition in Eq. (II. 1),

$$N_{Sd} = N_{Sd,e}\left(1 + \frac{E_{c,s}A_{c,s}}{E_{c,e}A_{c,e}}\right) \quad \text{(II. 10)}$$

Simplifying Eq. (II. 10) by making $N_{Sd,e}$ the subject, and applying an equivalent deduction and substitution for $N_{Sd,s}$ from Eq. (II. 9), we obtain:

$$N_{Sd,e} = \frac{N_{Sd}}{1 + \frac{E_{c,s}A_{c,s}}{E_{c,e}A_{c,e}}} \quad \text{(II. 11)}$$

$$N_{Sd,s} = \frac{N_{Sd}}{1 + \frac{E_{c,e}A_{c,e}}{E_{c,s}A_{c,s}}} \quad \text{(II. 12)}$$

Further simplified as:

$$N_{Sd,e} = \frac{E_{c,e}A_{c,e}}{E_{c,e}A_{c,e} + E_{c,s}A_{c,s}}\ N_{Sd} \quad \text{(II. 13)}$$

$$N_{Sd,s} = \frac{E_{c,s}A_{c,s}}{E_{c,s}A_{c,s} + E_{c,e}A_{c,e}}\ N_{Sd} \quad \text{(II. 14)}$$

Equations (II. 11) - (II. 14) show that each domain's share of the applied axial force is governed by its axial rigidity, E_cA_c, relative to the combined rigidity of the composite section. A domain of higher concrete modulus attracts a proportionally greater share of N_{Sd} independently of its cross-sectional area, which is essentially relevant especially in the strengthening configurations where the strengthening cover and the existing core are cast from concretes of markedly different grade.